Diploma thesis
Florian Wittkötter

Realizing a Resonator Cooling scheme for Ultra-Cold Fermi Gases

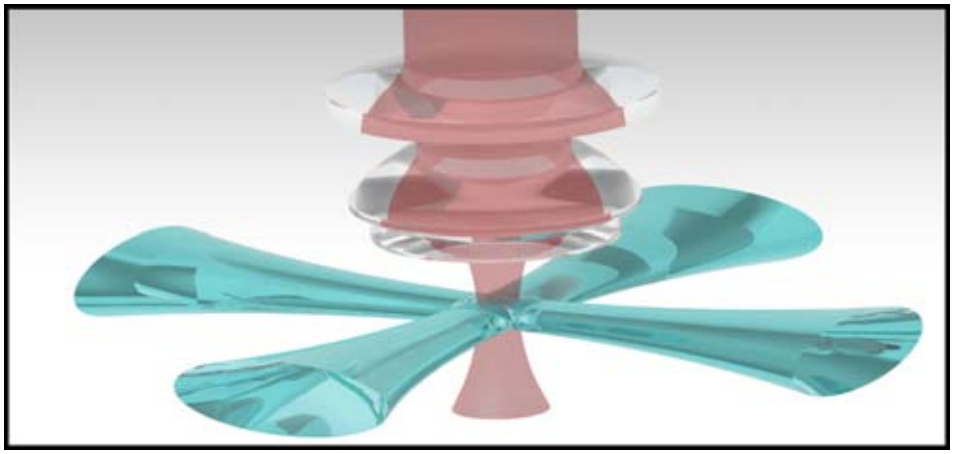

Universität Hamburg
Institut für Laserphysik
Arbeitsgruppe Quantenmaterie

Evaluators:
Prof. Dr. Henning Moritz
Prof. Dr. Klaus Sengstock

Hamburg, 21th April 2011

Universität Hamburg
DER FORSCHUNG | DER LEHRE | DER BILDUNG

ILP
INSTITUT FÜR LASERPHYSIK

Abstract

In the frame of this diploma thesis a vacuum chamber and a resonator for the efficient cooling of atomic gases in a new experiment was designed and tested.

An essential part of the novel cooling scheme utilized is an optical dipole trap. In this dipole trap the atoms will be captured and cooled to the quantum degenerate regime by forced evaporation. A large trap depth is necessary in order to transfer a large number of atoms from the magneto-optical trap which is used for precooling into the dipole trap. A deep dipole trap can be realized with moderate laser power using the power enhancement of a resonator. It is possible to load from a relatively large volume since the transfer is carried out outside of the focus of the resonator mode at a large beam radius. A subsequent transport of the atoms to the focal region increases the density and thereby the efficiency of the evaporation.

The construction of the vacuum chamber and the resonator are strongly connected since the resonator is placed inside the vacuum chamber. The cavity losses are strongly reduced inside the vacuum chamber which enables the large desired enhancement of the laser power. The vacuum chamber and the resonator were designed as 3D-models and manufactured by professional workshops. A laser system for the characterization of the resonator was built and a feedback loop with a bandwidth of approximately 40 kHz was implemented. With this setup the finesse of the resonator was determined to be $F = 4155 \pm 453$ which is equivalent to an enhancement by a factor of 1323 ± 144.

Contents

1 Introduction

Solid state physics is a driving force for technological progress since it trigger the development of new materials with unconventional mechanical, electrical, optical, and thermodynamical properties. Understanding the basic principles underlying the intriguing properties of some materials, however, is very challenging because many of the interesting features arise from complex quantum many-body interactions. Often even the simplest approximative models describing such intriguing phenomena as high temperature superconductivity are not solvable in full detail with todayŠs computational methods [20].
The experimental realization of Bose-Einstein condensation [2] and Fermi degeneracy [7] in dilute gases of neutral atoms, however, led to a novel approach to this research field. The experimental techniques developed to tune the interaction by Feshbach resonances [6] and to realize arbitrary potentials with the dipole force [10] allow for realization and precise control of many parameters of general model Hamiltonians [9]. These quantum simulations may shed new light on long standing questions of many fields of physics such as solid state physics and in turn motivate new experiments.
One of the prominent theories in this frame is the Hubbard model [16] describing electronic properties in solid state systems. It can be simulated very accurately by means of alkali atoms in optical lattices [18]. The current experimental challenges include the observation of the quantum mechanical ground state of the Fermi-Hubbard Hamiltonian. For half filling this ground state is characterized by antiferromagnetic order and requires very low temperatures [5].
In the presence of the pioneering progress in the field of quantum optics during the past years and the arising fundamental questions a new apparatus optimized for the investigation of low dimensional systems is currently being built. The specific aim of the new experiment is to maintain maximal flexibility by means of atomic species employed as well as possible potentials and excellent imaging capabilities. A prerequisite for reaching low temperatures in dilute gases is an efficient evaporation scheme with a fast cycle time and initial large atom numbers. For this reason a new all-optical cooling scheme conceived by T. Esslinger [32] is combined with a powerful microscope setup and a glass cell enabling excellent optical access.
A common solution for trapping potentials for evaporative cooling are magnetic traps since they offer large volumes and large trap depth. For fermions, however, magnetic traps have the drawback that the trapping potential depends on the spin state which leads to a partially polarized gas. For identical fermions the collisions die out at low temperatures leading to a strong suppression of the thermalisation rate and hence of the evaporation efficiency in magnetic traps. Furthermore, spin mixtures in magnetic traps typically experience strong losses.
Optical traps which are based on the dipole force offer a spin independent potential.

Yet a large volume and a high trap depth is necessary in order to guarantee an efficient loading of the evaporation trap from the previous magneto-optical trap. To simultaneous reach a high trapping volume and depth as well as high thermalisation rates with the optical dipole force is a challenging task. A resonator can be used to enhance the available laser power but for fast thermalisation high frequencies and thus tight focusing is necessary which is contrary to a large volume.
In this diploma thesis the design of a ring resonator for a dipole trap enabling both, a high transfer volume and fast thermalisation is presented. The idea of the new evaporation scheme is to load the dipole trap from the MOT outside of the resonator focus in a standing wave configuration which is reached by coupling two counter-propagating beams into the resonator. After the loading process the frequencies of both beams are detuned such that the interference pattern moves and the atoms are transported to the focal region. Once the atoms are in the focus one of the beams is ramped down and evaporation is performed by lowering the power in the remaining beam. To enable high enhancement and thus a deep trap the resonator is placed inside the vacuum. Therefore the design of the main vacuum chamber and the resonator is strongly connected and consequently the design of the main vacuum chamber is also part of this diploma thesis. Finally a setup for the characterization of the resonator was built.
In the first chapter an introduction to general aspects of the manipulation of ultra-cold atoms and an overview of the atom preparation cycle is given. The second and third chapters address the design process of the vacuum chamber and the cooling resonator respectively. A summary of the optical and electronic setup required for operation of the cooling resonator is given in chapter four. Reports on first characterizing measurements are also included in the last chapter.

2 Framework

To observe quantum phenomena in a dilute gas of neutral atoms very low temperatures on the order of 100 nK are necessary. To reach these low temperatures is a very challenging task. In this experiment a new, advanced cooling scheme is set up in order to maintain maximal flexibility concerning the atomic species employed and with the intention to reach larger atom numbers and shorter cycle times than in previous experiments. By using a ring resonator to create a dipole trap for the final evaporative cooling it is possible to enhance the loading efficiency from the magneto-optical trap employed for precooling as well as the evaporation speed with an all-optical and thus species-independent cooling procedure (2.2). To further enhance the evaporation efficiency Feshbach resonances (appendix 7.1) will be employed which enable the control of the interaction strength between neutral atoms by a magnetic field.
Although the focus of this thesis lies at the design and testing of the vacuum chamber and the cooling resonator, a very brief introduction to techniques which generally enable the cooling and trapping of neutral atoms is given (2.1). A detailed discussion of these techniques can be found in [22].

2.1 Cold gases

Nowadays many elements (mostly alkali metals) can routinely be cooled down to a few hundred Microkelvin by laser cooling techniques (2.1.2). However, for the final cooling step all quantum gas experiments rely on evaporative cooling (2.1.3 and 2.1.5). Evaporative cooling is based on the idea to remove the hottest atoms from a conservative trap while the remaining atoms thermalize leading to a lower temperature. The trapping potential determines the initial atom number and temperature as well as the thermalisation rate thus making the choice of a suitable trap crucial. Apart from magnetic traps optical traps became a key technology for the investigation of ultra-cold gases because they allow trapping of all spin states in contrast to magnetic traps. Moreover they make a variety of different potentials from almost homogeneous *bath tubs* to different optical lattices possible.
In this thesis a resonator for a new optical evaporation trap is realized which simultaneously allows for a large and deep loading volume and fast thermalisation. Like all optical traps it is based on the optical dipole force which is the subject of section 2.1.4. First the different behavior of bosons and fermions at low temperatures is discussed (2.1.1).

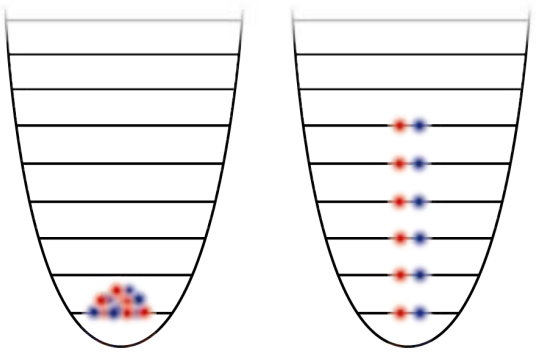

Figure 2.1 – Schematic representation of bosons (left) and fermions (right) at $T = 0\,\mathrm{K}$ in two different spin states (red and blue). While bosons accumulate in the lowest state of a trapping potential fermions stack up to the Fermi energy.

2.1.1 Quantum statistics

The properties of an ideal gas (i.e. without interactions) under ambient pressure and temperature can be derived completely from the Maxwell-Boltzmann distribution and do not depend on the fermionic or bosonic nature of its constituents (classical limit). However, when the phase space density ρ[1] approaches unity the wave functions of individual atoms start overlapping and the gas must be described using quantum mechanics. The occupation probability p of a quantum mechanical state i with energy ε_i is given by the Fermi-Dirac $(+1)$ and Bose-Einstein (-1) statistics respectively:

$$\langle p(\varepsilon_i)\rangle = \frac{1}{e^{\beta(\varepsilon_i-\mu)} \pm 1} \tag{2.1}$$

where μ denotes the chemical potential and $\beta := (k_B T)^{-1}$ with Boltzman's constant $k_B = 1.38 \cdot 10^{-23}\,\mathrm{JK}^{-1}$. In the case of a trapped gas the energies ε_i are determined by the trapping potential.
For both distributions a temperature corresponding to a phase space density of approximately unity can be derived. Systems with a temperature below this crossover temperature are often referred as to be in a quantum degenerate state. To study quantum mechanical effects, such as superfluidity, in dilute vapors of neutral atoms the corresponding crossover temperatures in the Nanokelvin scale have to be reached.
For a bosonic gas in an anisotropic harmonic trap[2] the critical temperature T_c is determined by the trap frequencies ω_j and the number of atoms in the trap N:

$$T_c \propto (\omega_x \omega_y \omega_z N)^{1/3} \tag{2.2}$$

[1] $\rho = n\Lambda^3$ with the number density n and the de Broglie wavelength Λ.
[2] The trapping potential is given by: $U(x,y,z) = \frac{1}{2}m(\omega_x^2 x^2 + \omega_y^2 y^2 + \omega_z^2 z^2)$, where m is the mass of the atom.

For temperatures below T_c the number of accessible exited states becomes less than the total number of atoms in the trap which leads to a macroscopic occupation of the single particle ground state (Bose-Einstein condensation). The investigation of this degenerate system is especially instructive since it makes a quantum mechanical single particle state macroscopically observable.
For fermionic atoms condensation is impossible because of the Pauli principle which states that two identical fermions can not occupy the same quantum mechanical state. This implies that at $T = 0$ all states up to the so called Fermi energy are occupied exactly once and all others are empty. The corresponding Fermi temperature (T_F) is given by:

$$T_F = \frac{E_F}{k_B} \propto (\omega_x \omega_y \omega_z N_i)^{1/3} \tag{2.3}$$

where again a harmonic trap is assumed and N_i denotes the number of atoms in a certain internal state.
The above discussion is only valid in thermal equilibrium and does not account for the effects of interactions at all. Yet interacting gases feature the exciting physics. For example, a gas of weak attractive interacting fermions at very low temperatures become superfluid similar to electrons in bulk materials. The difference between bulk materials and dilute gases is the excellent controllability of the potential[3] and the interaction strength for dilute gases hence making the study of these systems very instructive. A description of interaction phenomena and dynamics is beyond the scope of this thesis but can be found in various text books and reviews such as [27] and [19].

2.1.2 Laser cooling

Two different light forces on atoms have to be distinguished, the conservative dipole force and the scattering force. Here the scattering force is introduced in order to gain first insights into laser cooling. A more detailed discussion can be found in [22].
The scattering force or radiation pressure relies on absorption and spontaneous emission of photons. When a beam of near-resonant light is directed shone at a two-level atom the latter will constantly absorb and reemit photons. Each absorbed photon gives rise to a recoil of momentum $\hbar\mathbf{k}$ in the beam direction. The momentum transfer connected to the spontaneous emission, however, averages to zero over time since it is isotropic. The resulting force is velocity dependent and thus dissipative because of the Doppler shift seen by a moving atom. More precisely, because of the Doppler shift the frequencies of absorbed and emitted photons differ by Δ which denotes the detuning of the laser frequency with respect to the atomic transition frequency. Therefore every absorption-emission cycle gives rise to an energy exchange between the light field and the atom of $\hbar\Delta$. For red detuning ($\Delta < 0$) this exchange means a loss of energy from the system.
Due to the Doppler effect an atom with a velocity component towards a red detuned light beam will more likely absorb photons from this beam than from a beam with the same frequency as the first beam but traveling in the opposite direction. Due to this preferred

[3] Please note that inhomogeneities inevitably introduced by a realistic trapping potential in experiments also provides drawbacks.

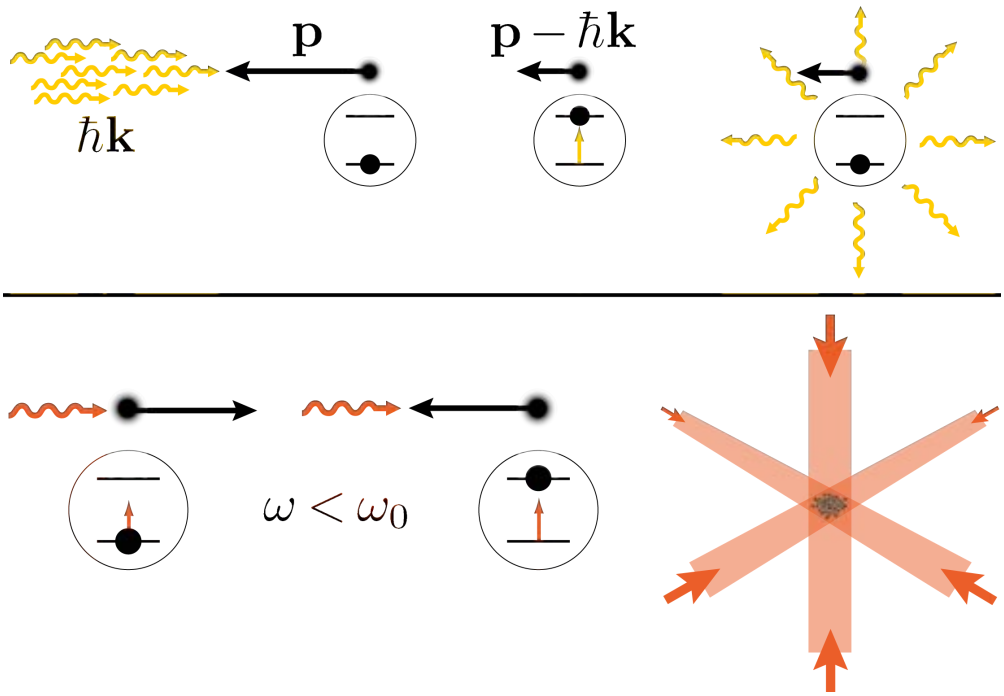

Figure 2.2 – A beam of light imposes a dissipative force on an atom due to the momentum transfer from directed absorption and isotropic spontaneous emission (top). Six orthogonal, red detuned laser beams can be used to cool an atomic sample since atoms most likely absorb photons from a counter-propagating laser due to the Doppler effect (bottom). Please note that atoms are not trapped in an optical molasses

absorbtion of counter-propagating red detuned photons an atomic sample can be cooled in three dimensions by three pairs of counter-propagating laser beams (see figure 2.2). The temperature in such optical molasses is limited due to the *random walk* the atoms perform in momentum space caused by the arbitrary direction of spontaneous emission. The corresponding Doppler temperature can be derived from an equilibrium condition between heating and cooling rate and is given by:

$$T_D = \frac{\hbar\Gamma}{2k_B} \tag{2.4}$$

where Γ is the linewidth of the atomic transition. For typical parameters this temperature is of the order of some hundred Microkelvin and thus far above typical degeneracy temperatures (T_c and T_F respectively) of a few hundred Nanokelvin.

Cooling with the scattering force

The atomic vapor for quantum gas experiments is produced by heating a small piece of

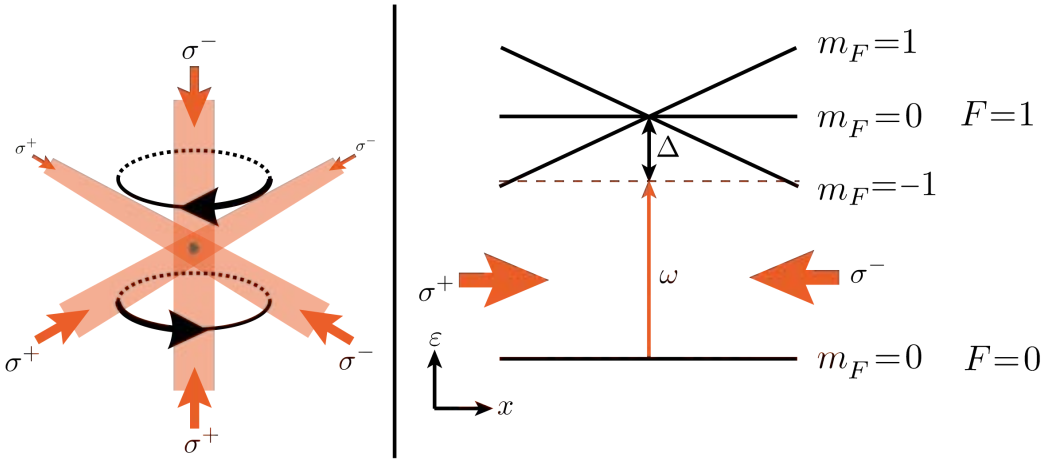

Figure 2.3 – The hyperfine states of an atom with total angular momentum $F = 0$ in the ground state and $F = 1$ in the excited state will split due to the Zeeman Effect as depicted on the right when a magnetic field gradient with $B = 0$ in the center is applied. Appropriate polarized red detuned (by Δ) counter-propagating laser beams (frequency ω) can be used to apply a spatial dependent force since off center atoms will come in resonance with a beam pushing them to the center. An experimental setup to trap and cool atoms due to the scattering force in all three dimensions is schematically shown on the left (the black arrows indicates magnetic coils) .

the desired element which leads to the vapor due to increased vapor pressure. Cooling down this vapor is one of the most challenging tasks when investigating phenomena in the quantum degenerate regime. The cooling strategy strongly depends on the atomic species employed. Two very widespread techniques for the first cooling step are the two-dimensional magneto-optical trap and the Zeeman slower.

A magneto-optical trap (MOT) combines pairs of counter propagating, polarized laser beams with a magnetic field gradient such that the scattering force becomes space dependent. For atoms with an appropriate internal structure this can be used to cool and collect the atomic gas at a specific position (see figure 2.3). Since the cooling in a MOT relies on the scattering force the lowest achievable temperature is given by T_D.

By using the MOT principle for two dimensions in a volume with relatively high pressure, slow atoms from the background gas can be captured and cooled in these dimensions. Along the third dimension a pushing beam can be applied producing a dense beam of relatively slow atoms leaving the 2D-MOT region.

For the Zeeman slower technique the atoms are heated in an oven where a small aperture allows for directional emission. A laser beam counter-propagating to the atomic beam gives rise to the scattering force which slows the atoms. To compensate for the change in the Doppler shift when the atoms slow down it is necessary to tune either the laser wavelength or the atomic transition frequency. A Zeeman slower achieves this compen-

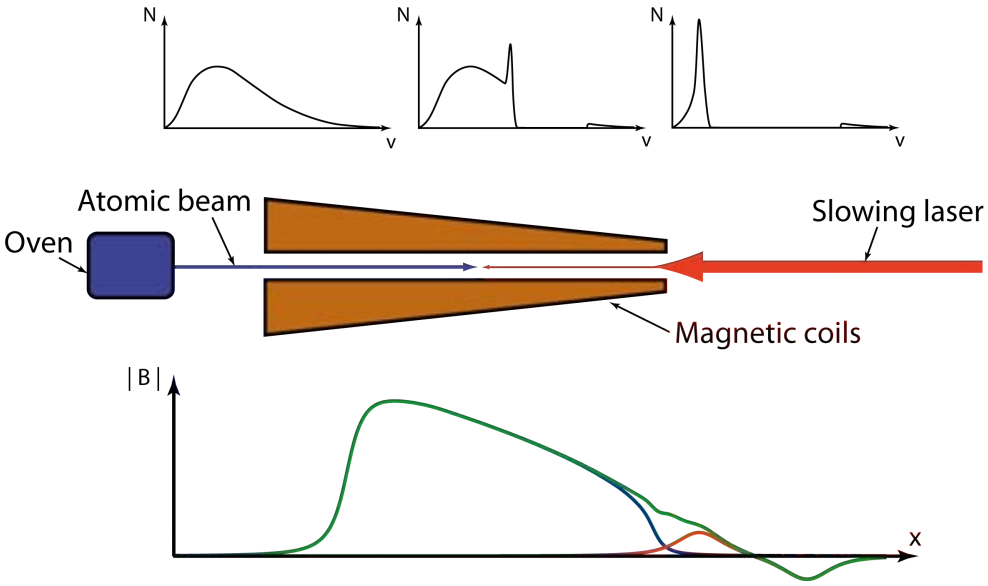

Figure 2.4 – The magnetic field of the Zeeman slower used in this experiment on the axis (bottom) and a schematic representation of the Zeeman slower (middle) as well as of the velocity distribution at different points (top). The MOT field is indicated in red. A smooth gradient of the total field is favorable to minimize unwanted diverging of the atomic beam thus making good matching between MOT and Zeeman slower field necessary (fields calculated by K. Morgener).

sation by a magnetic field gradient and the associated Zeeman effect tuning the atomic transition frequency (see figure 2.4).
Both methods prepare the atoms in a directed beam which may point at a three dimensional MOT. Here the atoms can be recaptured and cooled to the Doppler limit. Although there are some very sophisticated schemes how to reach deeper temperatures with laser cooling it is impossible to achieve phase space densities of order unity. Therefore all quantum gas experiments use evaporative cooling as the final cooling step.

2.1.3 Evaporative cooling

Evaporative cooling relies on the idea of removing the hottest atoms from a thermal ensemble, by lowering the trapping potential for instance, leading to a reduced temperature after thermalisation. The achievable temperature depends critically on the trap employed.
The trap determines the initial atom number and temperature by the trapping volume and depth respectively. A large initial atom number is important since more removed atoms lead to a lower temperature and a large degenerate cloud is desirable. Usually evaporation is performed after precooling in a MOT. Typically a large and deep trapping potential is necessary in order to guarantee an efficient transfer of the atoms from the MOT.

Additionally the trapping potential determines the thermalisation rate, which is crucial for an efficient evaporation since it determines the speed at which atoms can be removed preserving thermal equilibrium. For example high densities[4] and trap frequencies lead to high scattering rates and thereby to a fast thermalisation. High trap frequencies in turn are equivalent to a tight confinement.
The thermalisation is mediated by elastic two body scattering making the corresponding cross section decisive for efficient evaporation. For a radial symmetric scattering potential such as atomic potentials it is convenient to expand the two-body scattering amplitude in terms of spherical harmonics [31]. For high angular momentum the scattering potential is modified by the centrifugal barrier such that for scattering with low energies only the first order term contributes to the scattering amplitude and cross section. This s-wave scattering cross section σ_0 converges to a finite value in the limit of low temperatures ($k \to 0$) given by:

$$\sigma_0 = 4\pi a^2 \tag{2.5}$$

where the scattering length a is defined by this equation. The scattering length can be tuned by a so-called Feshbach resonance modifying the interaction strength and thereby the thermalisation rate (appendix 7.1). To address a Feshbach resonance in an atomic sample a homogeneous, typically rather large, magnetic field must be applied.
In an intuitive picture s-wave scattering can be described as contact interaction. The Pauli exclusion principle, however, states that two identical fermions can not be simultaneous at the same place. Therefore the thermalisation rate is strongly suppressed in a polarized gas of fermionic atoms. To avoid this so-called Pauli blocking it is favorable to trap a gas of fermions in a potential that is independent of the spin state for evaporative cooling.
A common trap for cold atoms is the magnetic trap. It offers a large volume with adequate depth. The force in such a trap arises from the Zeeman effect which shifts the energy of an atomic state according to:

$$\Delta\varepsilon_i = \mu_B g_i m_{F_i} B \tag{2.6}$$

where m_{F_i} is the projection of the total angular momentum F_i on the magnetic field direction, g_i is called the Lande g-factor and μ_B is the Bohr magneton. From this formula it can be seen that only atoms with $m_{F_i} g_i < 0$ can be captured in a local magnetic minimum[5]. It can also be seen that the potentials for different m_F are not the same. For spin mixtures[6] this leads to spatial separation of the different states and such to a partially polarized gas. This causes serious problems for fermionic atoms as discussed above. Additionally magnetic traps are typically not compatible with the use of a Feshbach resonance. An alternative to magnetic traps is the optical trap which rely on the dipole force.

[4] Please note that a high density also lead to increased losses due to three body collisions.
[5] Magnetic maxima are not possible in free space as can be seen from Maxwell's equations.
[6] A gas of atoms in different spin states.

2.1.4 Dipole force

When a light field with a frequency which is detuned with respect to an atomic transition frequency is incident on an atom, it will induce an electrical dipole moment. The dipole moment in turn will interact with the incident light field. This back action is the origin of the optical dipole force. When the detuning is large compared to the splitting of sublevels in the atomic spectrum, the force is independent of the spin state. Additionally the dipole force is conservative, which makes it optimally suited to trap atoms for evaporation.
The induced dipole moment is given by $\mathbf{p}(\mathbf{r},\omega) = \alpha(\omega)\mathbf{E}(\mathbf{r},\omega)$ where the complex polarisability of the atom α depends on the laser frequency ω and $\mathbf{E}(\mathbf{r})$ is the amplitude of the electrical field. The energy associated with this induced dipole in the light field and hence the dipole potential is given by:

$$U_{dip} = -\frac{1}{2}\langle \mathbf{pE}\rangle_t = -\frac{1}{2\epsilon_0 c} Re(\alpha) I(\mathbf{r}) \tag{2.7}$$

where $I(\mathbf{r}) = \frac{1}{2}\epsilon_0 c|\mathbf{E}(\mathbf{r})|^2$ is the intensity of the light field. The brackets $\langle ...\rangle_t$ indicates that the effect of the electrical field oscillations with the laser frequency are averaged over time. The dipole force is given by the negative gradient of the potential: $\mathbf{F}_{dip} = -\nabla U_{dip}$.
Although the laser frequency is detuned with respect to the atomic transition frequency the atom will scatter some photons. The scattering rate Γ_{sc} can be calculated from the absorbed power P_{abs} leading to:

$$\hbar\omega\Gamma_{sc} = P_{abs} = \langle \dot{\mathbf{p}}\mathbf{E}\rangle_t = \frac{\omega}{\epsilon_0 c} Im(\alpha) I(\mathbf{r}) \tag{2.8}$$

This off-resonant photon scattering causes heating and therefore has to be minimized.
An explicit expression for the polarisability can be estimated within a semiclassical approach when the atomic structure is simplified to a two-level system. When the detuning of the laser frequency with respect to the atomic transition frequency is chosen much larger than the spectral linewidth of the atomic transition but much smaller than the transition frequency itself the resulting formulas can be approximated to:

$$U_{dip} \approx \frac{3\pi c^2}{2\omega_0^3}\frac{\Gamma}{\Delta} I(\mathbf{r}) \tag{2.9}$$

$$\frac{\hbar\Gamma_{sc}}{U_{dip}} = \frac{\Gamma}{\Delta} \tag{2.10}$$

where $\Delta = \omega - \omega_0$ is the detuning of the laser frequency ω with respect to the transition frequency ω_0 and Γ the line width of the transition. As can be seen from the first equation the dipole force is repulsive towards high intensities for blue detuning ($\Delta > 0$) where it is attractive for red detuning ($\Delta < 0$). Therefore already a simple focused laser can provide a trapping potential.
For propagation in z direction a laser can be described by a gaussian beam reading:

$$E(r,z,t) = E_0 \frac{w_0}{w(z)} e^{-\frac{r^2}{w(z)^2}} e^{-i\left(kz - arctan\frac{z}{z_R} + \frac{kr^2}{2R(z)}\right)} e^{i\omega t} \tag{2.11}$$

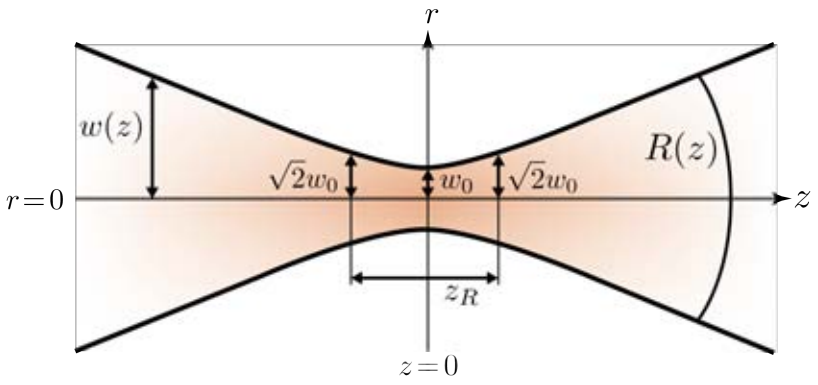

Figure 2.5 – Schematic representation of a focussed Gaussian beam. For a description of the indicated quantities see text.

where $r^2 = x^2 + y^2$. As shown in figure 2.5 the beam radius $w(z)$[7] evolves in z direction according to:

$$w(z) = w_0 \sqrt{1 + \left(\frac{z}{z_R}\right)^2} \tag{2.12}$$

with the beam waist w_0 and the Rayleigh range $z_R = \frac{\pi w_0^2}{\lambda}$ which is a measure for the intensity variation in z direction[8]. $R(z)$ indicates the radius of curvature of the wavefront which has a minimum at $z = z_R$ and diverges for $z \to 0, \pm\infty$:

$$R(z) = z\left(1 + \left(\frac{z_R}{z}\right)^2\right) \tag{2.13}$$

Alternatively to those quantities the gaussian beam can also be described by a single parameter:

$$\frac{1}{q(z)} = \frac{1}{R(z)} - i\frac{\lambda}{\pi\omega(z)^2} \tag{2.14}$$

For the sake of completeness the intensity distribution can be calculated with the aid of the total beam power $P = \int_0^\infty 2\pi I(r,0) r dr = \frac{\pi}{2} w_0^2 I_0$ and is given by:

$$I(r,z) = \frac{2P}{\pi w(z)^2} e^{-2\frac{r^2}{w(z)^2}} \tag{2.15}$$

The focused Gaussian beam with red detuned light is the simplest dipole trap but of course other potentials are possible. For example interfering laser beams can provide optical lattices in all dimensions and even more complicated potentials are possible by combining attractive and repulsive traps.

[7] The value of r where the intensity dropped to $\frac{1}{e^2}$ of it's value for $r = 0$.
[8] $I(0, z_R) = \frac{1}{2} I(0,0)$

For a specific application and atomic species the choice of an appropriate wavelength and laser power is crucial to generate the desired potential. Nowadays many isotopes and even ions of different elements are routinely trapped and manipulated by the dipole force. It should be pointed out again that the dipole force is not dissipative and hence the atoms will oscillate for ever in a dipole trap when no additional cooling mechanism is present.

2.1.5 Evaporation in dipole traps

Dipole traps are conservative and independent of the atomic spin state and thus optimally suited to trap an atomic cloud for evaporative cooling. The evaporation process in dipole traps is initiated by lowering the laser power. For an efficient evaporation fast thermalisation and efficient transfer from the previous cooling stage is essential.
The thermalisation rate and hence the efficiency of evaporative cooling is determined by the density in the trap and the trap frequencies. For a dipole trap formed by a symmetric gaussian beam ($\omega_x = \omega_y =: \omega_r$) the trap frequencies in the radial (ω_r) and longitudinal (ω_z) direction are given by:

$$\omega_r = \sqrt{\frac{4U_0}{mw^2}} \tag{2.16}$$

$$\omega_z = \sqrt{\frac{4U_0}{mz_R^2}} \tag{2.17}$$

respectively. Here m denotes the mass of the atoms and U_0 is the potential depth in the center of the trap which can be calculated with formulas 2.9 and 2.15. To reach high thermalisation rates and hence an efficient evaporation high trap frequencies are crucial. It can be seen from equation 2.17 that a high trap frequency in longitudinal direction is equivalent to thigh focussing of the laser. For an efficient transfer from a MOT, however, a rather large volume is required.
Another drawback for dipole traps concerning evaporative cooling is the high intensity required to trap atoms. For typical parameters already laser powers on the order of some hundred Watts are necessary, even for a rather small overlap between the MOT and dipole trap. Especially for far off-resonante dipole traps high laser powers are necessary. Far detuned dipole traps are favorable in order to reach lower temperatures since photon scattering is reduced.
A resonator can be used to enhance the trap depth for a given laser power. In addition a tight longitudinal confinement is naturally provided by the interference pattern of the standing wave in a two-mirror resonator. Unfortunately it turns out that the thermalisation rate and thereby the cooling efficiency in the resulting two-dimensional systems is suppressed by some mechanism not finally identified[9].
A ring resonator in contrast needs tight focusing in order to provide sufficient longitudinal confinement since the resonating mode (TEM_{00}) can be described by a Gaussian

[9] This phenomenon has not yet been systematically studied but has been observed in experiments in Innsbruck [23] as well as in Zürich [40] (personal discussion with H. Moritz).

beam. This tight focussing, however, leads to a small volume and therefore to a low transfere efficiency.
Simply loading the atoms from the MOT into a traveling wave resonator outside of the focal region is not a good solution either. Because of the conservative nature of the dipole force the atoms will start strong oscillations where heating is the only damping mechanism.

2.2 A new cooling scheme

For the observation of such exiting phenomena as anti-ferromagnetic order extremely low temperatures on the order of $TT_F^{-1} \approx 0.06$ are necessary. To reach these temperatures with a reasonable large atomic sample and different atomic species a novel, all-optical cooling scheme will be implemented. The large vacuum chamber (chapter 3) required to accomodate the involved resonator trap severlely reduce the optical access at the cooling position. Therefore the atoms are loaded into a dipole trap and transported into a glass cell after evaporation.
After a brief summary of the entire atom preparation cycle (2.2.1), the strategy for evaporative cooling will be discussed in detail (2.2.2). The chapter will conclude with a short outline of the experimental goals (2.2.3).

2.2.1 Atom preparation cycle

To achieve ultra low temperatures and high atom numbers a sophisticated cooling scheme is necessary. The first element to be investigated in this experiment is fermionic lithium (^{6}Li) but later an upgrade to other atomic species (Na, K) should be enabled. This demand for a flexible scheme with high efficiency for fermionic atoms makes an all-optical cooling favorable.
Figure 2.6 schematically shows the atom preparation scheme utilized in this experiment. Lithium vapor is created in an oven at approximately 400°C. The atoms are released from this oven as a directed beam pointing at the main vacuum chamber, slowed down by a Zeeman slower and recaptured in a magneto-optical trap. The Zeeman slower is designed so that it may also be used for sodium. Potassium in contrast will be captured from background pressure by a 2D-MOT. However, all atomic species are recaptured in the three dimensional MOT and cooled to the Doppler limit (figure 2.6a).
The final evaporation is performed in a far detuned optical dipole trap. Good performance for all atomic species is reached by the choice of an appropriate wavelength and sufficient laser power. For this purpose a new scheme for a resonator dipole trap is implemented (section 2.2.2). The basic idea of this scheme is to load the atoms from the MOT into a large volume of a dipole trap. Once the atoms are inside the dipole trap they are moved adiabatically to the resonator focus (figure 2.6b). Finally evaporation is performed by lowering the laser power circulating in the resonator (figure 2.6c).
The cooling will be performed in a large vacuum chamber which prevents optimal optical access. Therefore the final experiments are performed in a glass cell (appendix 7.2). The transport of the atoms from the cooling chamber to the glass cell is achieved via a

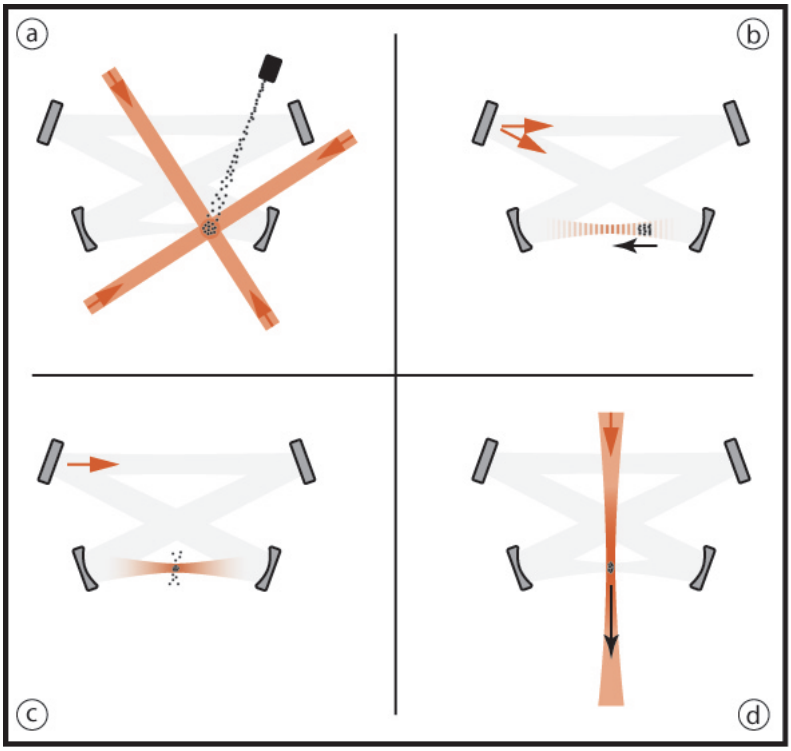

Figure 2.6 – Schematic representation of the atom preparation cycle. The MOT is loaded from an atomic beam (a) and the atomic sample is cooled to $T \approx T_D$. The atoms are then transferred into a far detuned optical dipole trap wich is formed by the interference pattern of two counterpropagating beams in a resonator and transported to the focus (b). In the focus evaporative cooling is performed (c). Finally the atoms are transported into the glass cell by a second dipole trap (d).

dipole trap formed by a single focused laser beam (figure 2.6c). For this transport only a relatively low laser power is required since the atomic gas is already relatively cold. The focusing lens for the transport trap is mounted on an air-bearing translation stage such that the focus can be shifted from the focus of the dipole trap were the final evaporation is performed into the glass cell were the experiments take place.

2.2.2 Evaporation scheme

For an efficient evaporation scheme a large and deep dipole trap is desirable. A resonator can be used to enhance the available laser power. Following the discussion in section 2.1.5 neither a typical standing wave resonator nor a typical ring resonator provides a dipole trap for an efficient evaporation scheme. An idea how to combine a large capture volume with high thermalisation rates and overcome the drawbacks of conventional dipole cooling resonators was conceived by Tilman Esslinger and first described in [32].
The basic idea is as follows: First the atoms are loaded from a MOT into the large

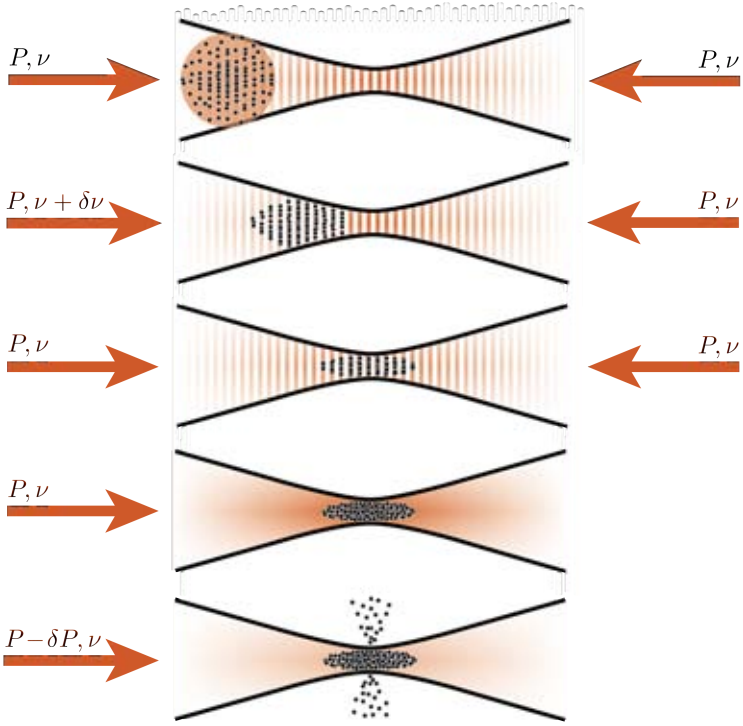

Figure 2.7 – Schematic representation of the single steps performed in the resonator dipole trap. From top to bottom: First the atoms are loaded from the MOT into the interference pattern of two counter propagating beams. By itroducing a frequency difference the atoms are then transported to the focal region where one beam is ramped down. Finally evaporative cooling is performed by lowering the power in the remaining beam.

volume of a standing wave interference pattern. Then this atoms are moved inside the interference pattern into a focus region such that no heating occurs (adiabatical). Finally the trap is changed to a running wave configuration and the evaporation is performed (see figure 2.7).
Exactly this scheme can be realized by coupling two counter-propagating beams into a ring resonator providing a small focus. When the frequencies of both beams are identical, a standing wave pattern will emerge. The spacing of the individual interference maxima is given by half the wavelength of the utilized light. By choosing the loading position outside the resonator focus a rather large overlap between the resonator mode and the MOT can be achieved. After the MOT light and magnetic coils are switched off the frequencies of the two beams are slightly detuned and consequently the interference pattern start to move. The captured atoms can be transported in the moving interference pattern to the focal region. Here the focus itself provides longitudinal confinement and one of the beams can be ramped down. The evaporation can now be performed in this running wave configuration by simply lowering the power in the remaining beam. Since the transport increases the density of the atomic cloud the thermalisation rate will also be enhanced.

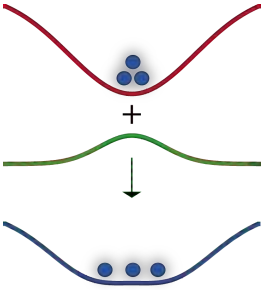

Figure 2.8 – A homogeneous dipole potential for neutral atoms (bottom) can be generated by superimposing a red detuned (top) and a blue detuned (middle) laser beam.

Furthermore since no magnetic fields are required for trapping, the thermalisation rate can be further enhanced by use of a Feshbach resonance. With this resonator evaporation scheme a powerful tool for efficient cooling of fermionic atoms is available.

2.2.3 Experimental goals

The last decade has seen extraordinary progress in the research field of ultra-cold fermionic gases. A systematic review of this development was compiled by M. Inguscio, W. Ketterle and C. Salomon [17]. Recently intriguing systems such as imbalanced spin mixtures, bose-fermi mixtures [11] [26], fermions in optical lattices, double wells with few atoms [1] and far from equilibrium situations in general [28] attract scientific attention. To potentially contribute to all of these topics the new experiment is designed with a flexible but nevertheless very powerful cooling scheme and excellent optical access to the atomic cloud. This optical access is guaranteed since the atoms are moved from the cooling position into a flat glass cell for the experiments.
Imaging of the atoms is accomplished with a high resolution ($\approx 600\,\mathrm{nm}$) microscope above the glass cell. A second, identical microscope placed opposite to the first one allows for manipulations on the same length scale. Around the microscopes Feshbach coils are placed to allow for tuning the interaction strength. Besides the superior optical access enabled by a glass cell compared to a metal cell, a glass cell also allows for fast switching of the magnetic fields since no eddy currents are present.
Dipole traps are used to hold the atoms during the experiments. Here various potentials are possible. To achieve very clean potentials an arrangement of two ring resonators placed around the glass cell will be utilized. These resonators provide very elliptical modes and guarantee perfectly superimposed modes when different beams are coupled into the resonators. For example a red and a blue detuned laser beam coupled in simultaneously make the creation of very homogeneous potentials possible as depicted in figure 2.8. In the vertical direction two blue detuned laser beams under a small angle will be used to create two dimensional systems. Because of the wide spacing between two sheets in this geometry it is possible to only occupy one layer. Of course also systems in lower dimensions are realizable by coupling counter propagating lasers into the resonators.

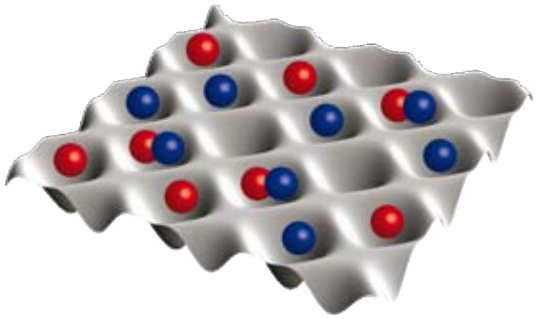

Figure 2.9 – Schematic representation of fermions in two different spin states (blue and red) in an optical lattice. For low energies the properties of the system are determined by the tunneling between adjacent sites (J) and the on site interaction (U). This state is described by the Hubbard model.

This setup enables the investigation of the properties of interacting fermions in two-dimensional optical lattices within the Hubbard model and beyond. The Hubbard model describes interacting particles in the lowest band of a lattice potential. The physical properties of atoms in optical latices within the Hubbard model are determined by the tunneling matrix element between adjacent sites J and the on-site interaction energy U. The Fermi-Hubbard Hamiltonian for spin $\frac{1}{2}$ particles in optical lattices reads:

$$H = U \sum_i \hat{n}_{i,\uparrow} \hat{n}_{i,\downarrow} - J \sum_{\{i,j\},\sigma} \hat{c}^\dagger_{i,\sigma} \hat{c}_{j,\sigma} + \sum_{i,\sigma} \varepsilon_i \hat{n}_{i,\sigma} \tag{2.18}$$

where the first term describes the interaction energy and the second the kinetic energy in the system. The occupation number operator of site i is given by $\hat{n}_{i,\sigma} = \hat{c}^\dagger_{i,\sigma} \hat{c}_{i,\sigma}$ where $\hat{c}^\dagger_{i,\sigma}$ and $\hat{c}_{i,\sigma}$ denote the creation and annihilation operator of a particle with spin σ ($\uparrow$ or $\downarrow$) respectively. The last term takes into account the possible inhomogeneity within the lattice where ε_i denotes the site specific offset.
Possible experiments in this context are to impose local excitations and observe the propagation of the excitations through the lattice or to rapidly change the interaction strength with respect to the tunneling rate (interaction quench) and investigate the thermalisation properties [8]. Obviously the planned setup also offers a wide range of other opportunities.

3 The vacuum system

The lifetime of an ultra-cold atomic gas in a trap is limited by light scattering, three body collisions and scattering with background atoms. While the first two are inevitable assuming a given light field and interaction strength, the latter only depends on the background pressure. Therefore every quantum gas experiment is performed under ultra-high vacuum (UHV) conditions. To achieve pressures as low as 10^{-11} mbar a sophisticated vacuum system is necessary.
In the frame of this diploma thesis the main vacuum chamber for the new experiment, where the cooling cycle takes place, was designed. The main constrains on the chamber geometry are defined by the desired optical access (3.4) and the coils for the high magnetic field which are necessary to address Feshbach resonances (3.5). Many general aspects for reaching the UHV have to be considered when planning a new vacuum system where the most important with respect to this work are introduced in (3.3). However, first an overview of the whole vacuum system (3.1) and the geometric boundary conditions on the main chamber (3.2) are given.

3.1 The apparatus

Figure 3.1 shows a CAD drawing of the entire vacuum system with the arrangement for the magnetic coils. In the following the main parts will be introduced.
The cooling scheme discussed in 2.2.2 provides good performance for different atomic

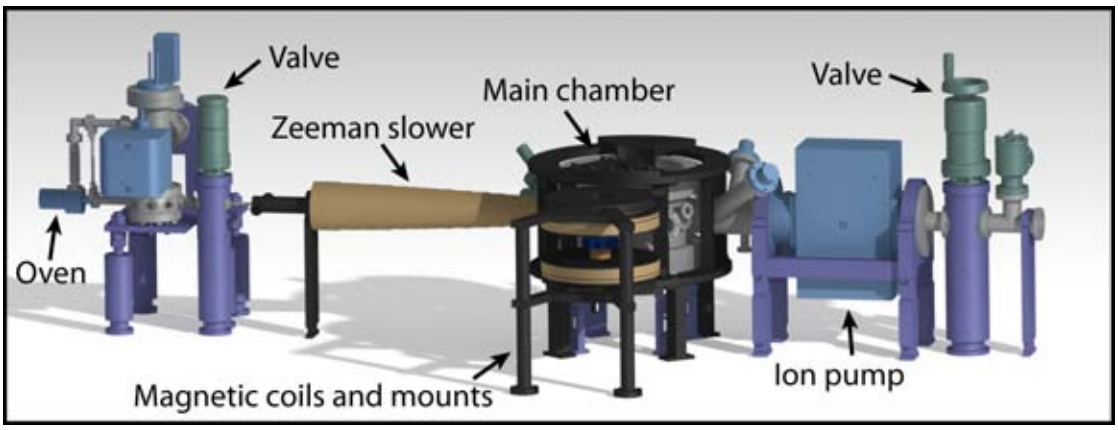

Figure 3.1 – A CAD-drawing of the vacuum system and the magnetic coils. One sees the oven, the Zeeman slower, the main vacuum chamber and the arrangement for the magnetic coils as well as the main vacuum pump.

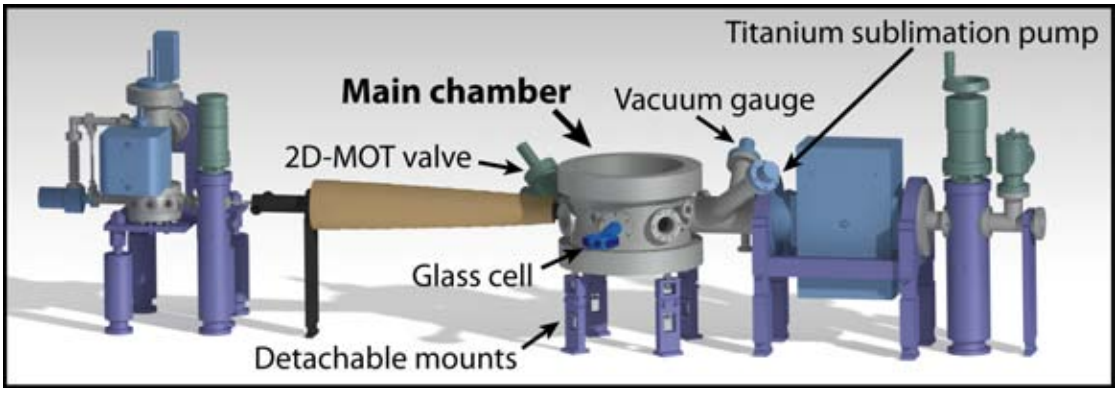

Figure 3.2 – The main chamber within the vacuum system, the design process is discussed in sections 3.4 and 3.5. The mounts which are designed to attach the magnetic coils after the bake-out of the vacuum system is performed are indicated as well as the galss cell, the valve for the upgrade with a 2D-MOT and the vacuum gauge and the titanium sublimation pump for the main chamber.

species, where lithium is the first element which will be investigated but a later upgrade for sodium and potassium is taken into account. The lithium vapor is created in an oven and guided through a Zeeman slower into the main vacuum chamber. In this chamber the further cooling steps are performed. The Zeeman slower length and coil arrangement is optimized for an efficient cooling of both, lithium and sodium as well as for good matching with the MOT field. Therefore the apparatus can be upgraded for sodium by a simple modification of the oven and a more costly adaption of the laser system. Potassium will be produced in an additional 2D-MOT where at the moment only a valve[1] is placed to enable this option.
A magnetic rotary feed-through[2] behind the oven allows for blocking the atomic beam when not needed. Since no mechanical wear will occur the beam can be blocked every experimental cycle. The advantage of this beam shutter is that the window opposite to the oven is not continuously exposed to the lithium which would deposit on it and thus decrease the optical access or even destroy the viewport. Nevertheless it may be necessary to heat the window in order to get rid of the deposited material or even to replace it by a new one. For this purpose a valve[3] is placed behind the large ion pump for the main chamber. A second valve is provided to attach the primary vacuum pumps. Another valve[4] can separate the oven from the remaining vacuum system in order to make easy repair and upgrad possible.
The Zeeman coil is not wrapped directly around the vacuum tube but on a larger tube which provides cooling by an inner water flow. The advantage of this separate mounting is that no heating which would decrease the vacuum through enhanced outgassing or

[1] All metal inline valve from MDC Vacuum.
[2] Vacom: MagiDrive MD16.
[3] VAT Vacuum Valves: All-Metal Gate Valve CF40 Inventory:QM-00019
[4] VAT Vacuum Valves: All-Metal Gate Valve CF16 Inventory:QM-00020.

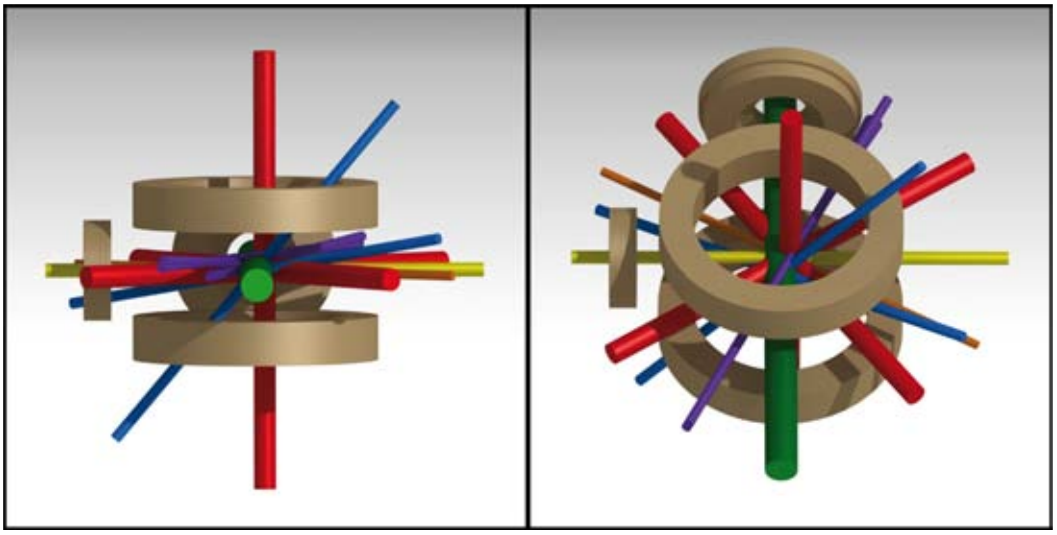

Figure 3.3 – Scaled summery of all parts determining the geometry of the main vacuum chamber. Shown are the magnetic coils and the resonator beams (purple, details in chapter 4) as well as the beams for the MOT (red), the Zeeman slower (yellow), the transport dipole trap (green), the 2D-MOT (orange) and for imaging (blue).

vibrations are imposed on the vacuum system. The magnetic coils for the MOT and the Feshbach field at the main chamber as well as at the glass cell are also mounted without contact to the vacuum system.
A differential pumping tube at the entrance to the Zeeman slower allows for a pressure at the oven several orders of magnitude higher than inside the main chamber (approximately 10^{-9} mbar at the oven and 10^{-11} mbar in the main chamber). The vacuum at the oven is provided by a small ion pump[5] and an additional titanium sublimation pump. A vacuum gauge[6] constantly monitors the pressure at the oven. At the main chamber a larger ion pump and another titanium sublimation pump are employed and again a vacuum gauge is used to monitor the pressure.
Figure 3.2 again shows the entire vacuum system but now the magnetic coils are removed. Here the main vacuum chamber with the glass cell can clearly be seen. Some details on the glass cell can be found in appendix 7.2 whereas the main chamber will be discussed in the following.

3.2 The main vacuum chamber

A goal of this diploma thesis was the design of the main vacuum chamber. The geometry of this chamber is determined by the coils for the magnetic fields for the MOT and for addressing the Feshbach resonances as well as by the required optical access.

[5] A $15\mathrm{ls}^{-1}$ nitrogen ion pump from Gamma Vacuum: 25S-DI-2V-SC-N-N Inventory: QM-00071.
[6] A combined Pirani - Bayard - Alpert sensor from Pfeiffer Vacuum: PBR260, Inventory: QM-00036.

The same coils should be used for the Feshbach and the MOT field[7] but since the two central positions do not coincide additional pushing coils are required for the MOT field. All of these coils are depicted in figure 3.3 together with the beams determining the optical access necessary.
The cooling scheme discussed in section 2.2.2 will be performed in the main vacuum chamber and requires an appropriate optical access. An atomic beam is either created by a Zeeman slower (yellow) for lithium and sodium or a 2D-MOT (orange) for potassium. This atomic beam loads a MOT (red) where the atoms are cooled to the Doppler limit. Subsequently the atoms are transferred into the resonator dipole trap (purple), transported into the focus of the resonator mode and evaporatively cooled by lowering the power circulating in the resonator. After evaporation the atoms must be transported into the glass cell. This is achieved by a second dipole trap (green) where the focus and thereby the atomic vapor can be moved. It is desirable to image (blue) the atomic cloud from different directions in order to gain full information about the three dimensional density distribution.
In addition to these optical accesses ports for some vacuum devices are necessary. In the main vacuum chamber a pressure below 10^{-11} mbar is essential. This pressure is provided by a large ion pump and an additional titanium sublimation pump. The pressure is monitored by a vacuum gauge and an electrical feed-through is required for the frequency stabilization of the cooling resonator.
The mounting of the cooling resonator provides additional restraints on the chamber geometry. The design of both, the resonator and the chamber were performed in parallel but in this thesis for clarity the resonator will be discussed separately in chapter 4 where the vacuum chamber will be treated as a given boundary condition. Before the design process of the vacuum chamber will be addressed in detail in sections 3.4 and 3.5 a short introduction to vacuum techniques is given now.

3.3 Vacuum techniques

When planning a chamber for experiments under UHV conditions many technical details have to be considered. In the following section the most important aspects with respect to this work will be outlined. In particular these are the aspect of vacuum leaks (3.3.1), the problem of outgassing (3.3.3) and appropriate UHV connections (3.3.2). For a more complete and detailed discussion of techniques for the generation of ultra-high vacuum the reader is referred to [25]. This section is concluded by very short introductions of vacuum gauges (3.3.4) and electrical feed-throughs (3.3.5).

3.3.1 Vacuum leaks

It is crucially important that no leaks connect the inner part of a vacuum chamber to the environment. At the required pressures even smallest cracks will rapidly reduce the vacuum quality. Even when there are no real leaks the vacuum can suffer from so called

[7] One only has to change from a Helmholtz to an anti-Helmholtz configuration.

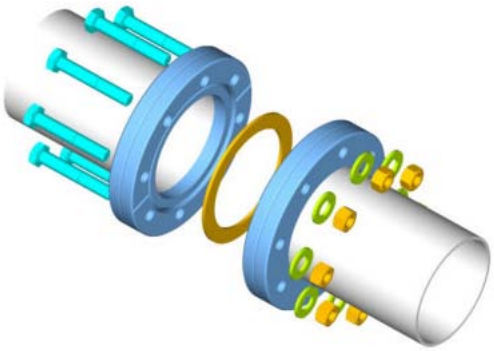

Figure 3.4 – Working principle of CF connections (taken from [30]). The two flanges (dark blue) provide edges which are ditching in the gasket (yellow) of a soft metal (e.g. copper) when the two flanges are tightly screwed together.

virtual leaks.
Virtual leaks are small, nearly closed volumes within the chamber in which air is trapped which is released only over very long timescales so that efficient pumping is not possible. For example badly performed welding may lead to virtual leaks. In order to guarantee welding without virtual leaks it is important to ensure good access to every weld when designing a vacuum chamber. Another possible source of virtual leaks are two surfaces directly contacted to each other. Since they will never be exactly flat these contacts can trap air and should be avoided in the design process. Virtual leaks are especially annoying since they can not be found by leak testing. Leak testing is done by applying helium selectively to the point at the chamber where the leak is suspected while a special sensor connected to the vacuum pumps measures the helium concentration in the gas pumped from the chamber.

3.3.2 UHV flanges

The mounting of pumps, measuring gauges and viewports to a vacuum chamber in the UHV regime is another crucial point. The mounting in the UHV regime is accomplished with so called CF flanges (*con flat*® connections). CF flanges have an edge at both sides and a gasket of some soft metal (e.g. copper) is placed in between the two knife edges. Both parts are tightly screwed together and an all metal seal is realized (see figure 3.4). When assembling CF connections it is important to evenly tighten the screws to guarantee a good seal.
Different gaskets are used for special situations. For example lithium reacts chemically with copper and correspondingly might destroy copper gaskets when the gasket is exposed to too high concentrations of lithium. Nickel gaskets are used at the oven for this reason. Since viewports are quite sensitive to stress it is convenient to use annealed copper gaskets, which are softer but also more expensive, to attach viewports to the vacuum

system. A general drawback of CF-connections is that they are very massive and thus need much space.

3.3.3 Outgassing

Every material shows outgassing, i.e. sublimation and desorption into the vacuum, which leads to a decreasing vacuum quality and therefore has to be minimized. The choice of material is crucial for this aspect. Stainless steel shows low outgassing and a high mechanical stability[8] and is therefore the preferred material for vacuum chambers. The residual outgassing of mainly hydrogen [14] can be further suppressed by heating the chamber when evacuated (bake-out). Most gas from the surface and from inside the material will thereby be lost before the experiments start. Typical bake-outs are performed at a few hundred degrees Celsius for some days to weeks.
The bake-out will be more efficient when the whole chamber is placed inside a vacuum and the temperature is on the order of 900 °C (vacuum annealing). Yet vacuum annealing works only for high-quality stainless steel (e.g. 316 grade) since for low quality stainless steel (e.g. 304 grade) the high temperatures may lead to inter crystalline corrosion. Inter crystalline corrosion causes smallest tears between the crystalline parts of the material (leaks) and therefore decrease the final vacuum.
In any case it is recommended to heat the chamber under atmosphere when assembled. Thereby long organic (grease) molecules are destroyed which may otherwise survive vacuum bake-out and pumping.
Of course also the inner chamber surface is important regarding the vacuum quality. There are some special surface treatments promising an improved vacuum. For example electropolishing reduces the surface roughness and thereby suppresses outgassing. By depositing a non-evaporable getter[9] on the chamber surface the surface even acts as additional sorption pump and once the getter material is saturated, it can be reactivated by heating the chamber [24]. However, since appropriate pressures are typically reached without any special surface treatment the inner surface of the main chamber in this experiment was only mechanically processed.

3.3.4 Vacuum gauge

For observation of pressures down to 10^{-11} mbar the most suitable gauges work with the hot cathode principle. Here electrons from a heated filament ionize the residual gas, the ions are collected and the resulting current can be used to determine the pressure. The outcome of this measuring principle depends on the composition of the residual gas requiring a calibration or at least a corrective factor. Since in this experiment the exact composition of the residual gas is not known an error in the absolute value of the vacuum

[8] In contrast to glass for example which shows extremely low outgassing but is mechanically much more sensitive.
[9] A getter is a material which binds atoms from the residual gas by means of a chemical reaction (chemisorption) [29].

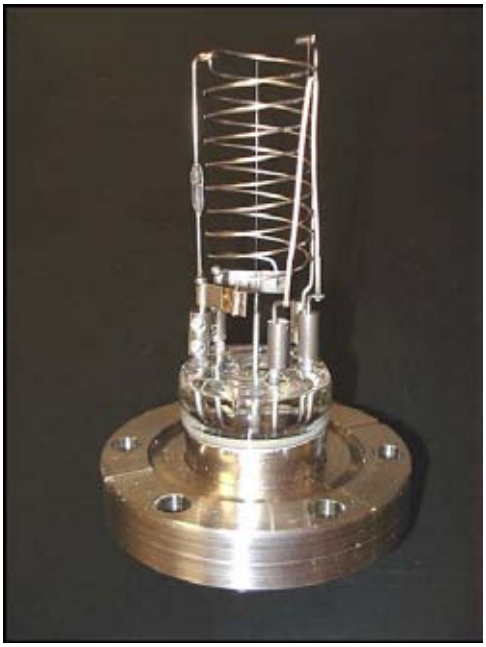

Figure 3.5 – A Bayard-Alpert vacuum measuring gauge mounted on a CF40 vacuum flange (taken from [38]). The filament on the right side (held by the springs) emits electrons when heated. The electrons are accelerated by a electric field generated by the coil and subsequently ionize the residual gas. The ions are collected by the center anode generating a current which is a measure for the pressure.

measurements is inevitable.
The most widespread hot cathode type is the Bayard-Alpert-sensor (figure 3.5). It provides a measuring range from 10^{-2} mbar to 10^{-11} respectively 10^{-2} mbar to 10^{-9} mbar depending on the acceleration grid[10]. Only the extractor-principle can measure even lower pressures (down to 10^{-13} mbar).

3.3.5 Electrical feed-through

The electrical feed-through for the piezoelectric tube voltage in this experiment is a two pin version[11] which allows for high voltages with a compact design. A critical point for such feed-throughs is the isolation since it has to be UHV suitable and therefore must show low outgassing rates. Commonly ceramics are used for this purpose which have the drawback of being sensitive to mechanical stress and therefore easily show leakages when not handled with care.

[10] Here a Varian (Agilent Technologies): UHV-24P Ion Gauge with a XGS-600 Gauge Controller is chosen. Inventory: QM-00061 and QM-00062
[11] Vacom: CF16-HV6-2-CE-SS13.

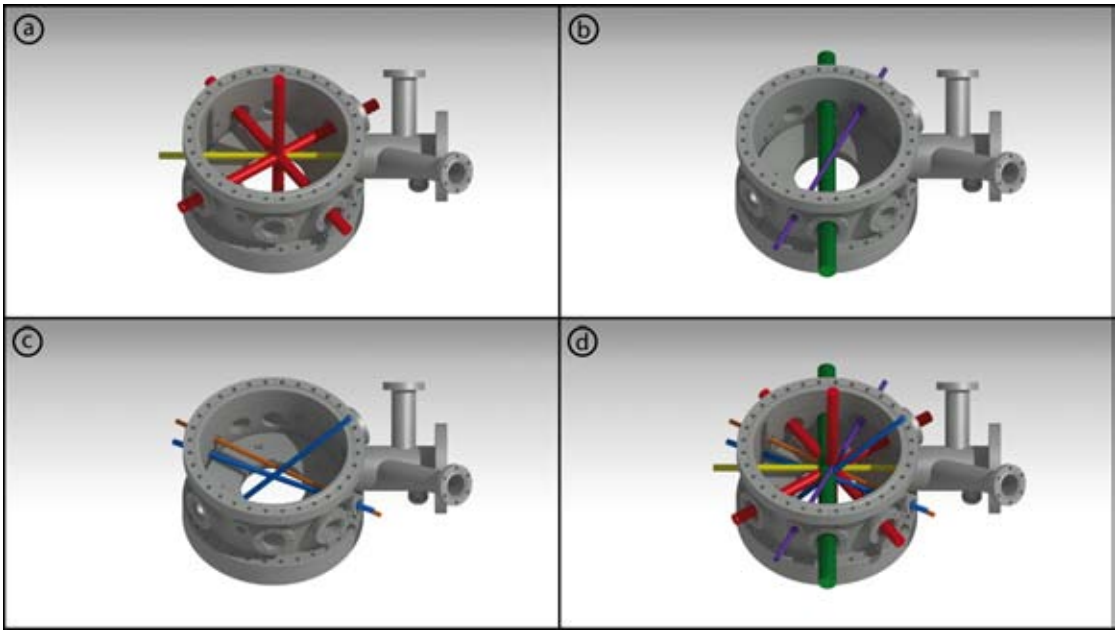

Figure 3.6 – The main vacuum chamber with all the different rays passing through it. The MOT and the Zeeman slower are indicated in a, the resonator rays and transport dipole trap in b and the 2D-MOT and imaging beams in c. All beams are shown in d.

3.4 Optical access

The shape of the main vacuum chamber is mainly determined by the desired optical access. Beside appropriate flanges at the main chamber for every beam (3.4.1) the choice of corresponding viewports is also important. For example, a viewport with a very flat surface is needed for the transport dipole trap whereas for the flanges near the glass cell a low magnetic susceptibility is essentiell (3.4.2).

3.4.1 Beams in the main chamber

For the cooling scheme described in 2.2.1 and 2.2.2 many laser beams are used, requiring an appropriate optical access. An overview of all beams involved and the resulting chamber geometry can be seen in figure 3.6. In the following paragraphs the requirements defining the position of every single beam are summarized. Additional drawings of the resulting chamber are given in figure 3.12.

MOT beams

To realize the MOT three pairs of counter-propagating, orthogonal beams with a diameter of approximately 30 mm are used. Hence six viewports are necessary. One of the MOT axes is fixed by the position of the magnetic coils. Since the MOT is situated off-center with respect to the magnetic coils very large viewports (CF100) at the top and bottom

flange of the chamber are used in order to exploit the available space optimally and allow for imaging in vertical direction. Because the MOT beam diameter was chosen to be approximately 30 mm the viewports for the remaining MOT beams are CF40 viewports.

Zeeman slower and pumping tube

The lithium and potassium atoms are produced in an oven and decelerated by a Zeeman slower. The Zeeman slower has to be directed towards the MOT position. It only needs a relative small tube and corresponding flange (CF25) but some space around the flange should be kept free in order to place the Zeeman coils as close to the chamber as possible. This close mounting will lead to a good matching between the Zeeman field and the MOT field.
The slowing laser will be guided through the ion pump which is located opposite to the Zeeman slower. A special feature of this ion pump is that it provide an optical passage making this placement possible. The tube for the ion pump has to be rather large to enable high pumping rates. An inner diameter of 72 mm was chosen which is slightly larger than the inner chamber height. The pump itself offers a CF100 flange which is why a CF100 is also welded to the chamber tube. In addition the electric feed-through for the piezoelectric actuator, a vacuum gauge and a titanium sublimation pump will be mounted to this tube. The titanium sublimation pump works best when it can coat the whole inner chamber surface, therefore a tilted mounting position is chosen.

Resonator beams

The resonator for the novel cooling scheme is placed inside the vacuum chamber. To enable incoupling and power monitoring additional viewports are used. Their position is determined by the position of the resonator (chapter 4). For the incoupling viewport a CF40 flange was chosen because the large clear aperture enables both, incoupling through one mirror and observation of the spot size, more precisely the beam divergence, through another mirror. For the power monitoring a CF16 flange is sufficient. The CF16 flange as well as the CF40 flange are slightly tilted with respect to the horizontal plane because the corresponding beams will be tilted as well.

Transport dipole trap and glass cell

After evaporation the atoms are loaded into a second dipole trap and transported to the glass cell. For the focused laser providing the dipole trap two viewports must be placed such that the beam intersect the center of the Feshbach coils. For the size of the viewport the divergence of the transport beam and the distance to the final position in the glass cell is crucial. The beam waist of the dipole trap of approximately 20 μm and the distance between glass cell and viewport of approximately 500 mm lead to a beam diameter for which a CF40 flange is sufficient. For the glass cell flange it is important that not too many other chamber parts are located close to it since the optics and magnetic coils around the glass cell will occupy a significant amount of space.

2D-MOT beams

To load, cool and use potassium the option to attach a 2D-MOT is considered. The atomic beam from this 2D-MOT must be directed towards the MOT position. It only needs a very small entrance because it is located close to the chamber and correspondingly the atomic beam will not have diverged much. Therefore a CF16 flange is sufficient for the 2D-MOT as well as for the viewport opposite for an optional slowing beam.
Instead of the 2D-MOT only an all metal inline valve from MDC[12] is installed at present. The valve is very compact compared to other better CF16 valves with larger optical access. Of course it should be kept in mind that much more space will be needed for the 2D-MOT vacuum chamber extension and the associated optics.

Imaging

Finally it is desirable to enable additional horizontal imaging at the position of the resonator focus perpendicular to the resonator beam. This turned out to be impossible within the restriction given by all the flanges discussed above. However, it was possible to place two CF16 ports for imaging close to the optimal direction at a small angle with respect to the horizontal direction.

3.4.2 Viewports for the main chamber

For the optical access appropriate viewports are necessary. For different beams and positions at the main vacuum chamber special properties of the viewports are important requiering different viewports. In this experiment viewports from Larson Electronic Glass are chosen.
The viewport for the transport dipole trap has to have a very good surface quality in order to avoid deformations of the beam during the transport which may lead to additional losses. It is the glass to metal transition rather than the utilized glass itself which limits the surface quality. Usually the glass to metal brazing is performed at high temperatures which lead to stress and in turn decreases the surface flatness. Therefore a special bonding with lead-silver alloy is employed for high quality viewports which can be processed at much lower temperatures. Unfortunately these viewports are much more expensive and are not specified for operations at temperatures higher than 200 °C[13] yet the coating is typically performed at 260 °C. However, for the viewports used in this experiment the coating was performed at 200 ° C wich results in a mechanically less stable coating and may also decrease the transmission coefficient.
Since lithium is an aggressive material the viewport opposite to the Zeeman slower has to withstand the corrosive effect. A sapphire viewport is appropriate and since a coating would be destroyed by the lithium it is not applied to this viewport. The viewports near the glass cell should show no residual magnetization in order to maintain precise control over the magnetic fields for the experiments.
Most viewports are anti-reflection coated to minimize the losses when a laser beam should be used inside the vacuum chamber. Since the possibility for magneto-optical traps and

[12]MDC Vacuum Products: MIV-150-V modified with a CF16 flange at one side.
[13]The melting point of lead-silver alloy is approximately 300 °C.

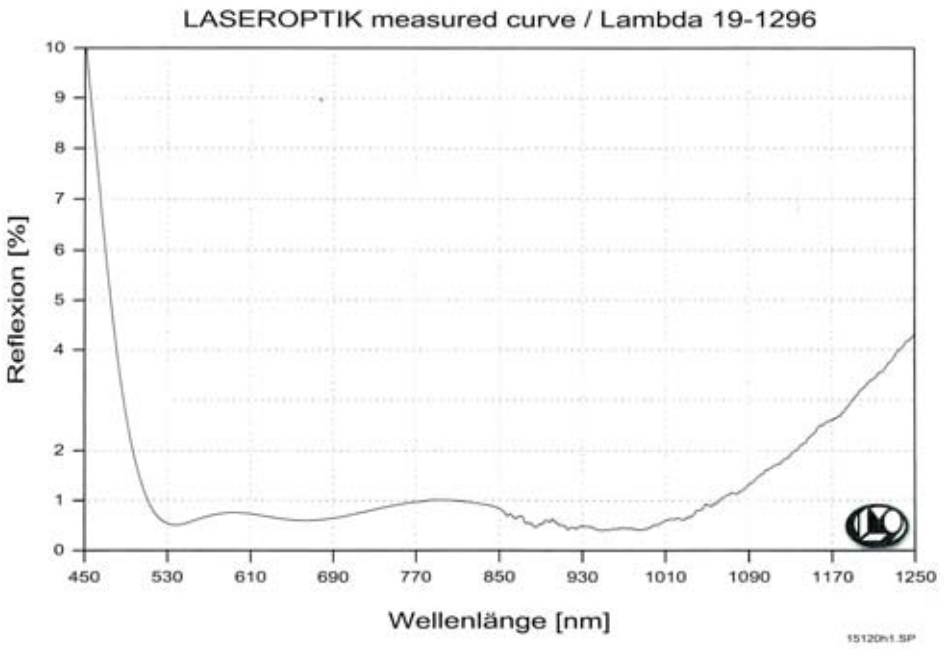

Figure 3.7 – The reflection of the coated viewports for normal incidence as measured by *Laseroptic Garbsen*. As can be seen the losses are below 1 % for the important range between 532nm and 1064 nm.

imaging systems for different elements is considered a broadband anti-reflection coating is employed. The reflection coefficient as measured by the coating company is shown in figure 3.7, the losses are below 1% in the important range from 532 nm to 1064 nm.
The inner side of all CF16 viewports is not coated since the relatively large metal flanges will partially block the coating beam thus making uniform results impossible. For CF16 viewports this so called shadowing effect decreases the usable diameter of coated viewports to approximately 5 mm.

3.5 Mechanical boundary conditions

In addition to the optical access discussed in the previous section also some other outer boundary conditions apply for the design of the vacuum chamber. For example the magnetic coils used to realize the cooling scheme set constraints on the chamber geometry (3.5.1). Moreover, the problem of proper mounting of the vacuum chamber to the optical table and of the cooling resonator to the chamber has to be considered in this context (3.5.2). Finally the choice of material and appropriate vacuum pumps is crucial to reach the UHV (3.5.3).

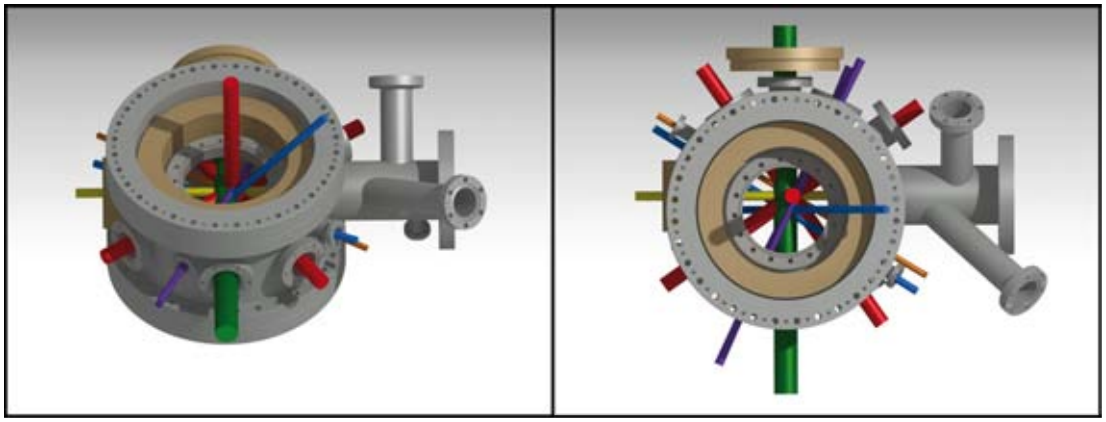

Figure 3.8 – The main chamber with top and bottom flange as well as all beams and magnetic coils necessary for the atom preparation. It can be seen that the Feshbach coils are situated very close to the atoms in order to generate the desired field. The two additional coils are utilized to push the center of the MOT field away from the resonator focus.

3.5.1 Magnetic fields in the main chamber

To trap and cool the atomic vapor both, MOT and Feshbach coils are required. In this experiment both fields will be generated with the same coils in order to realize a simple coil arrangement. Since these coils have to create rather large fields to address the Feshbach resonance they need to be close to the atoms and hence influence the chamber geometry. The specifications of the coils which consequently leads to a specific chamber design are discussed in the following paragraphs. The resulting chamber with the coils surrounding it is depicted in figure 3.8.

Feshbach field

The Feshbach resonance which should be adressed in this experiment requiering the highest magnetic field is the broad lithium resonance at 832 G[14] [3]. Thus the design target was to construct coils which can generate a homogeneous magnetic field of at least 1000 G at the chamber center.
Another demand on the coils is that it should be possible to assemble them after the bake-out of the chamber has been performed since the high temperature could destroy the isolation. The design of the coil mounting which is completely separate from the chamber[15] was not part of this thesis but enough free space had to be guaranteed. The coils are made of hollow copper wire[16] through which water constantly flows allowing for efficient cooling. This wire allow for a maximal current of approximately 10 Amm^{-2} in constant operation. Constraints on the coil geometry are the minimal bending radius of

[14] $1\,\mathrm{G} = 10^{-4}\,\mathrm{T}$
[15] In order to avoid imposing vibrations when they are turned on and off as well as heating which leads to enhanced outgassing.
[16] Delivered by OSWALD Elektromotoren GmbH, where also the winding is done.

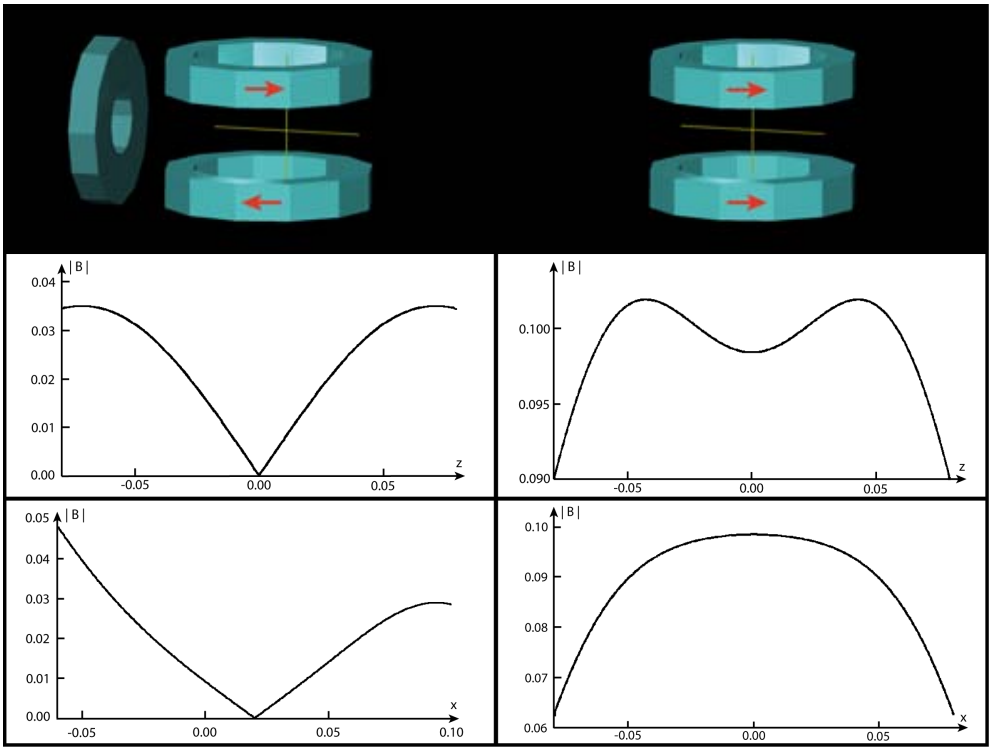

Figure 3.9 – These calculations where performed to ensure that it is feasibe to generate the MOT (left) and Feshbach (right) fields with the same coils. Shown are the coil arrangement (top) and the absolute value of the magnetic fields along the radial (bottom) as well as along the vertical (middle) direction each crossing the corresponding center position (units in Tesla and Meter respectively). The coils have an inner and outer diameter of 162 mm and 224 mm respectively, their spacing is 121 mm and the current was set to 10 Amm^{-1} for the Feshbach field and 5 Amm^{-1} for the MOT field (15 Amm^{-1} for the additional pushing coil).

the wire (30 mm for $4 \times 4\,\mathrm{mm}^2$ wire) and the maximal wire length which is determined by the maximal length for which a constant water flow is possible.
Simulations of the magnetic fields (figure 3.9) showed that it is best to use tubes for the top and bottom flange which allow the coils to be brought closer to the position of the atoms than the overall high of the vacuum chamber.

MOT field

In order to realize a simple coil arrangement the MOT field should be generated with the Feshbach coils used in an anti-Helmholtz configuration. However, the MOT position is displaced with respect to the Feshbach coils hence additional coils are necessary to shift the position of the field zero. Shifting the homogeneous Feshbach field is not possible. A superimposed second homogeneous field will only lead to a higher absolute value of the field and a field with a gradient which can shift the position of the field maximum will

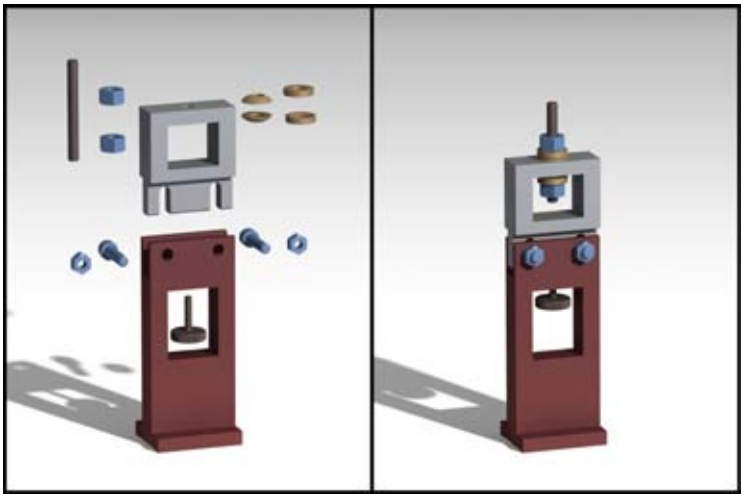

Figure 3.10 – These mountings where developed to ensure a stable chamber mounting and the possibility to assemble the magnetic coils after the bake-out. First the threading stick will be placed in special bores in the bottom of the main chamber. Then the upper part of the mount will be mounted and finally the chamber can be fixed on the optical table with the lower part of the mounts where the upper part is tightly clamped by the two vertical screws.

always impose inhomogeneities.
For a MOT the magnetic field gradient plays the key role and values of $5 - 15\,\mathrm{Gcm}^{-1}$ are reasonable. Again some calculations where done to ensure that enough place is left for appropriate coils. The magnetic field design was not part of this diploma thesis and therefore the calculations depicted in figure 3.9 only state approximate values to ensure the feasibility.

3.5.2 Chamber and resonator mounting

As mentioned above it should be possible to mount the coils after the chamber is baked out which means that the chamber mounts must be detachable. For this purpose the mounts depicted in figure 3.10 were designed. A vertical screw is provided for precise alignment of the chamber. The stability is guaranteed by clamping of the upper part tightly using the two horizontal screws.
To mount the resonator base plate (4.3) four thread bolts are welded to the bottom chamber flange. They are positioned such that they do not block any beams and are not at the position of the mirror holders.

3.5.3 Vacuum pumps and materials

Choosing suitable vacuum pumps is a challenging task but not part of this diploma thesis so the interested reader is referred to [30]. In this experiment the vacuum is established

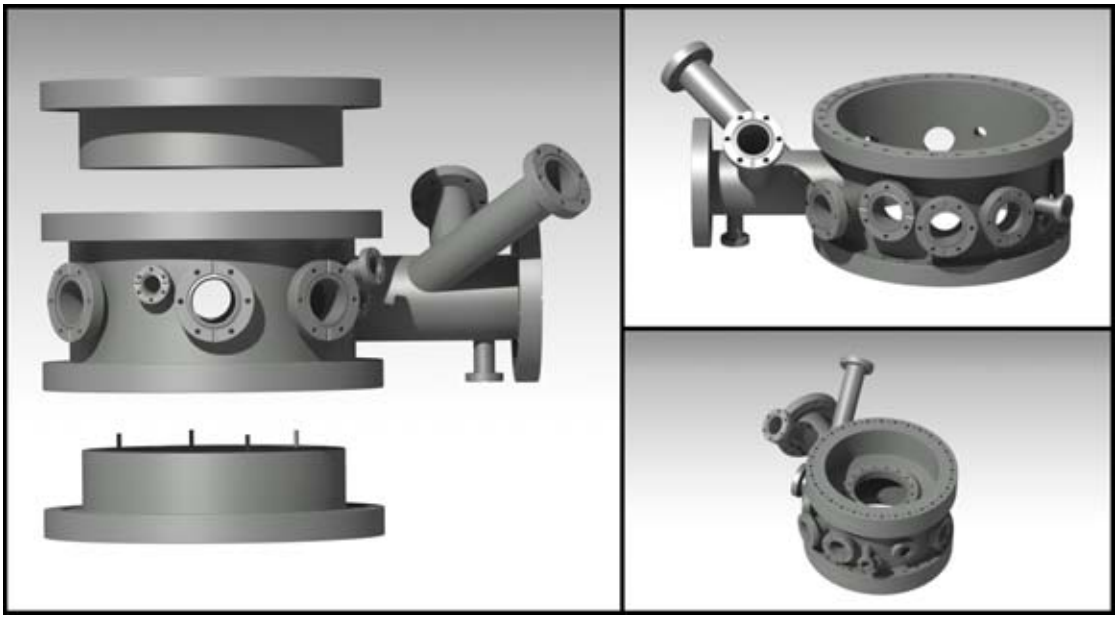

Figure 3.11 – Shown are CAD-drawings of the final vacuum chamber from different perspectives. For orientation: The Zeeman slower will be mounted opposite to the large (pumping) tube and the glass cell in front of the left picture.

in three stages. Initially the chamber is evacuated by a turbo molecular pump where a oil-free version is chosen. The pump maintaining the final vacuum at the main chamber during experiment is an ion pump[17]. An interesting feature of this specific pump is the optical passage provided by two oppositely placed CF100 ports. The ion pump will be activated constantly and should be mounted as close to the chamber as possible preferably with a large tube. In addition a titanium sublimation pump[18] can be activated to deposit titanium on the inner surface of the chamber which then acts as a getter and absorbs residual gases. This sublimation pump works best if it can deposite titanium in the whole chamber but with 950 °C it is quite hot and should therefore not be mounted too close to any temperature sensitive elements.
While the pumps help to get rid of residual gases, it is the choice of materials that determine the composition of the residual gas by outgassing from the material. A further aspect which is important for this experiment is that the chamber material should not have a high magnetic susceptibility since this would lead to perturbations in any applied magnetic field yet for the experiments high precision is necessary. It is also important to consider the processing when choosing a material in order to guarantee the producibility of the chamber. Stainless steel is a common material offering both low magnetic susceptibility and low outgassing rates. From the variety of types differing slightly in special properties such as mechanical strength and chemical stability, the *austenitic* grades 304

[17] A $80\,\mathrm{ls}^{-1}$ nitrogen ion pump from Gamma Vacuum: 100L-DI-6D-SC-N-N Inventory: QM-00070.
[18] Varian (Agilent Technologies): Mini Ti-Ball^{TM} Titanium Sublimation Source, Inventory: QM-00055

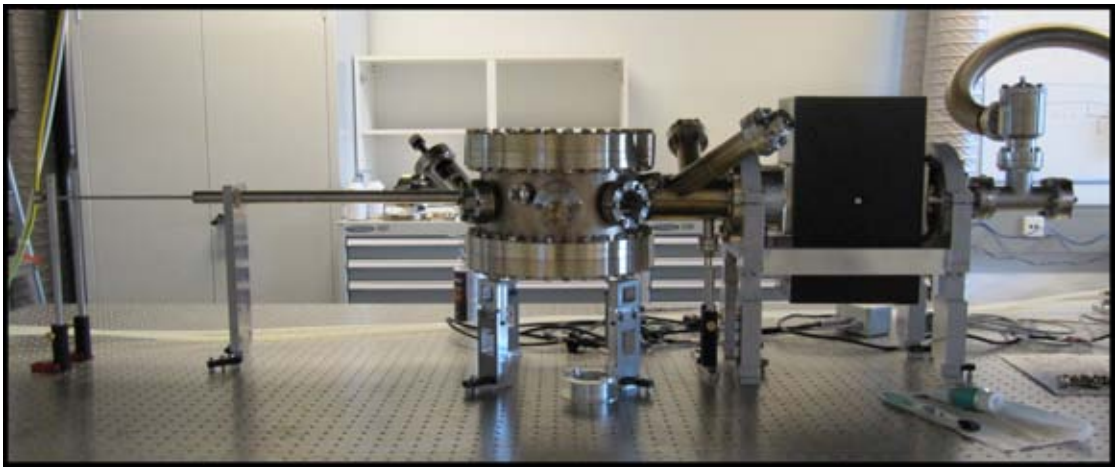

Figure 3.12 – The vacuum system during assembling. The Zeeman slower tube, main chamber and ion pump can clearly be identified.

(V2, European norm: 1.4301) and 316 (V4, European norm: 1.4401 / 1.4436) are very common for vacuum systems where the latter is superior in both demands, low outgassing rates and low magnetic susceptibility. Nevertheless for this vacuum chamber 304 is utilized since the differences seem marginal yet the price is much higher for 316.

4 The cooling resonator

Evaporative cooling is the key technique to achieve temperatures deep in the quantum degenerate regime. It can either be performed in magnetic traps or optical dipole traps both showing specific advantages and drawbacks. In the frame of this experiment fermionic atoms are investigated. Due to the Pauli principle two different spin states have to be captured simultaneously for efficient evaporative cooling of fermionic atoms. For this application a dipole trap is favorable (2.1.5). Very deep traps are necessary for an efficient evaporation scheme. A large trap depth can be reached by enhancing the light field of the dipole trap with a resonator. In this chapter the design of a ring resonator for a novel cooling scheme which will overcome drawbacks of other resonator dipole traps for evaporative cooling is reported.
In the first section (4.1) an overview of the relevant theory is given. The idea of the resonator and the working principle are then summarized in the second section (4.2). Finally this is followed by a detailed description of the design process and the technical parameters (4.3).

4.1 Resonator theory

A resonator or cavity consists of two or more mirrors (reflecting surfaces) arranged such that light can circulate between them. Since resonators play a key role within the new experiment and this diploma thesis a detailed description of the properties of resonators will be given. A more comprehensive discussion can be found in [33] on which this chapter is based.
In section 4.1.1 some general properties of resonators such as the finesse are derived where the plane wave approximation is applied. Subsequently the transverse field amplitude distribution in the resonator is discussed (4.1.2) and the result is used to obtain a condition for a stable resonator geometry within the ray matrix formalism (4.1.3). Since every resonator needs an active feedback to guarantee optimal incoupling efficiency the Pound-Drever-Hall technique for frequency stabilization is introduced in section 4.1.4. As an example the bow-tie resonator depicted schematically in figure 4.1 is utilized throughout this section.

4.1.1 Basic characteristics

An electro-magnetic wave incident on a mirror is split into a reflected and a transmitted part. The amplitudes of the electric field are described by the complex transmission and reflection coefficients t and r. They can be set to be real when the phase shift for transmission in one direction is taken to be $e^{i\frac{\pi}{2}} = i$. For a lossless mirror t and r are

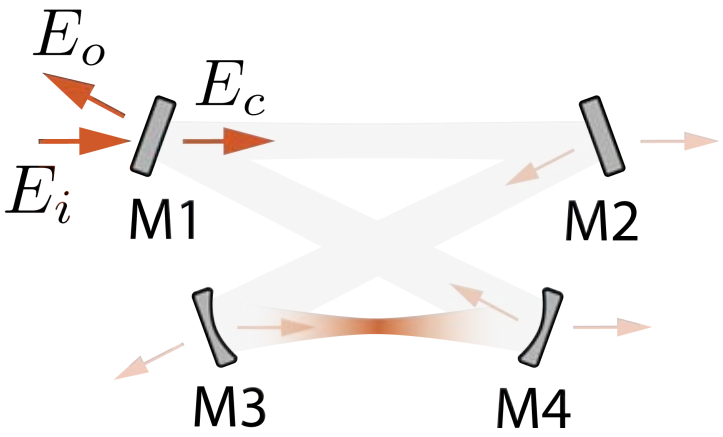

Figure 4.1 – Schematic representation of a simple bow-tie ring resonator. The labeling of the incident field E_i, the outgoing field E_o and the circulating field inside the cavity E_c will be used in the whole thesis. The transmitted fields at the other mirrors are disregarded. The mirrors M_i are characterized by their transmission coefficients t_i and reflection coefficients r_i for the electric fields respectively.

then connected by $r^2 + t^2 = 1$.
The following calculations are based on the scalar field approximation describing the electro-magnetic waves only by the amplitude of the electric field (vector character and the magnetic field are neglected). For a steady state situation the cavity field right behind the incoupling mirror E_c must equal the sum of the transmitted part of the field incident on the mirror E_i plus the field that has already made one roundtrip:

$$E_c = itE_i + gE_c \tag{4.1}$$

with the complex net roundtrip gain g. For the example given in figure 4.1 it reads $g = r_2 r_3 r_4 r_1 (1-\alpha) e^{i\phi}$ where α is a general loss term taking into account the absorption and scattering out of the resonator mode. α can be negative for an active medium placed inside the cavity (i.e. for a laser). For an empty resonator in vacuum with a roundtrip length L the phase ϕ is given by $\phi = \frac{\omega L}{c}$. For a lossless cavity ($\alpha = 0$) the circulating field is then calculated to be[1]:

$$E_c = \frac{it_1}{1 - |g| e^{i\omega \frac{L}{c}}} E_i \tag{4.2}$$

Here one sees the resonance character directly because for $\omega_{res} = 2\pi\nu_{res} = p2\pi\frac{c}{L}$ $(p \epsilon Z)$ a maximum in the circulating field is given which can be much higher than the incident

[1] In general r_i, t_i, α ϕ and g all depend on the frequency of the electromagnetic wave ω. This is neglect to improve readability

field. The same is true for the corresponding beam powers which are proportional to the square of the absolute values of the amplitude. The enhancement which is defined to be the ratio of the incident power to the circulating power on resonance is then:

$$\varepsilon = \left.\frac{P_c}{P_i}\right|_{\omega_{res}} = \frac{t_1^2}{(1-|g|)^2} \tag{4.3}$$

The resonance frequencies are called the axial resonator modes and the spacing between two modes is the free spectral range: $\Delta\omega_f = 2\pi\Delta\nu_f = 2\pi\frac{c}{L}$. The linewidth[2] of the resonance peak $\Delta\omega_l$ can be calculated by comparing the square of the absolute value of equation 4.2 to one half of it's maximal value (e.g. for $\omega = \omega_{res} = 0$) leading to:

$$\begin{aligned}
\frac{1}{2}\left|\frac{it_1E_i}{1-|g|}\right|^2 &= \left|\frac{it_1E_i}{1-|g|\,e^{i\frac{\Delta\omega_l}{2}\frac{L}{c}}}\right|^2 && (4.4)\\
\Rightarrow 2(1-|g|)^2 &= \left|1-|g|e^{i\frac{\Delta\omega_l}{2}\frac{L}{c}}\right|^2 && (4.5)\\
\Rightarrow \Delta\omega_l &= \frac{2c}{L}\arccos\left(1-\frac{(1-|g|)^2}{2|g|}\right) && (4.6)\\
&\approx \frac{2c}{L}\arcsin\left(\frac{1-|g|}{\sqrt{|g|}}\right) && (4.7)\\
&\approx \frac{1-|g|}{\sqrt{|g|}}\frac{2c}{L} && (4.8)\\
& && (4.9)
\end{aligned}$$

For the first approximation it is used that $\cos(x) = \sqrt{1-\sin^2(x)}$ and therefore $\arccos(1-x) = \arcsin(\sqrt{2x-x^2})$. Both approximations are valid for $|g| \approx 1$[3]. From the last equality the finesse is given by:

$$F = \frac{\Delta\omega_f}{\Delta\omega_l} = \frac{\Delta\nu_f}{\Delta\nu_l} \approx \frac{\pi\sqrt{|g|}}{1-|g|} \tag{4.10}$$

Another quantity directly connected to the finesse is the ring-down time. When a resonant beam is coupled into the cavity and is suddenly switched off at $t = 0$ the power inside the resonator will show an exponential decay. This can be derived when starting with the loss of the electric field amplitude for one roundtrip periode T inside the resonator, when no light is incident on the cavity:

$$\begin{aligned}
\frac{\partial E_c}{\partial T} &= -(1-|g|)E_c && (4.11)\\
\Rightarrow \frac{\partial E_c}{\partial t} &= -\frac{c}{L}(1-|g|)E_c && (4.12)\\
\Rightarrow E_c(t) &= E_{c,0}e^{-\frac{c}{L}(1-|g|)t} && (4.13)
\end{aligned}$$

[2]Full width at half maximum.

[3]Often the intensity reflection coefficient $R = |g|^2$ is used.

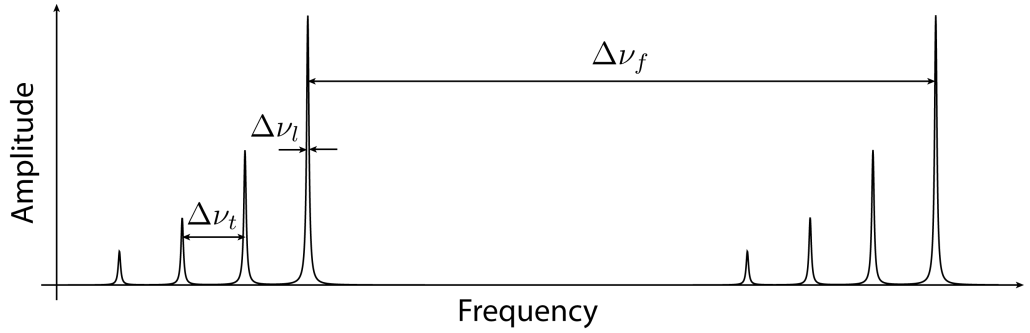

Figure 4.2 – A qualitative cavity resonance spectrum. $\Delta\nu_f$ denotes the free spectral range, $\Delta\nu_l$ the resonance line width and $\Delta\nu_t$ the spacing of adjacent transversal modes.

What can be measured by a photo detector is the power ($\propto |E|^2$) thus giving for the decay constant:

$$\tau = \frac{L}{2c(1-|g|)} \approx \frac{F}{2\pi}\frac{L}{c} \tag{4.14}$$

As a last point in this section the outgoing field E_o is discussed. E_o is a superposition of the directly reflected light at the incoupling mirror with the light that has already made one roundtrip and is transmitted by the incoupling mirror:

$$E_o = r_1 E_i + r_2 r_3 r_4 i t_1 e^{i\phi} E_c = \frac{1}{r_1}\frac{r_1^2 - g}{1-g} E_i \tag{4.15}$$

where for the second step equation 4.2 is used to substitute E_c. This can be interpreted as interference between the light transmitted out of the cavity by the incoupling mirror and the directly reflected light showing a minimum at resonance due to destructive interference. More precisely: on resonance the phase shift for one roundtrip is zero (or a multiple 0f 2π respectively) leading to an effective total phase shift of exactly $180\,^\circ$ due to the double transmission. When the amplitudes of both beams are the same they will interfere to zero (on resonance). Both amplitudes are the same in the case of perfect impedance matching which reads: $r_1 = r_2 r_3 r_4$.
In the impedance matched case for zero losses the enhancement can be approximated by the finesse:

$$\varepsilon = \frac{(1-r_1)^2}{(1-r_1 r_2 r_3 r_4)^2} \approx \frac{F}{\pi} \tag{4.16}$$

4.1.2 Transverse modes

The spatial amplitude variation of the electric field was not explicitly included in the discussion so far. In general an electro-magnetic wave (in the scalar field approximation) can be described by $\mathcal{E}(x,y,z,t) = E'(x,y,z)e^{i\omega t}$ where $E'(x,y,z)$ has to satisfy the scalar wave equation:

$$\nabla^2 E' + k^2 E' = 0 \tag{4.17}$$

with the wave number $k = \frac{\omega}{c} = \frac{2\pi}{\lambda}$. Under the assumption that the amplitude $E'(x, y, z)$ will only vary slowly with respect to the wavelength λ in the direction of propagation (e.g. z) this can be factored to $E'(x, y, z) = E(x, y, z)e^{-ikz}$ (where $\frac{\partial^2}{\partial z^2}E \approx 0$). Inserting the latter into (4.17) gives:

$$\frac{\partial^2}{\partial x^2}E + \frac{\partial^2}{\partial y^2}E - 2ik\frac{\partial}{\partial z}E = 0 \tag{4.18}$$

The boundary conditions for the individual solutions of this equation are determined by the cavity. A stable mode has to show the same radial intensity distribution after one roundtrip where a power drop due to losses and a phase shift is possible which is characterized in analogy to g by γ. This statement for a given z reads:

$$E_{nm}^{j+1} = \gamma_{nm}E_{nm}^{j} \tag{4.19}$$

where the exact form of possible E_{nm} depends on the geometry used and $\gamma_{nm} = |\gamma_{nm}|e^{i(w\frac{L}{c}-\phi_{nm})}$. The indices nm indicate the discreteness of solutions[4]. The phase is expressed by the phase of the central ray $\omega\frac{L}{c}$ and a correction term ϕ_{nm}. On resonance the exponential term becomes unity and the new resonance frequencies are given by:

$$w_{res} = 2\pi\frac{c}{L}(p + \frac{\phi_{nm}}{2\pi})\ (p\epsilon Z) \tag{4.20}$$

The magnitude of the correction ϕ_{nm} is typically much smaller than the free spectral range. A schematic mode spectrum is shown in figure 4.2.
The solutions to equation 4.18 under this boundary conditions are called transverse electronic modes (TEM_{nm}). The lowest order mode (TEM_{00}) shows a Gaussian intensity profile so that the electric field can be expressed by equation 2.11.

4.1.3 Geometric stability

The Gaussian mode discussed in the last subsection is a solution of the scalar wave equation in the paraxial approximation (paraxial Helmholtz equation). The propagation of a Gaussian beam can be described by the well known $ABCD$ matrices from ray optics as long as the elements fulfill the paraxial approximation with respect to the beam radius $w(z)$. The Gaussian mode is fully characterized by a single parameter q which is given by:

$$\frac{1}{q(z)} = \frac{1}{R(z)} - i\frac{\lambda}{\pi\omega(z)^2} \tag{4.21}$$

Therefore the propagation through an arbitrary element can be described by the effect of this element on q leading to:

$$q_o = \frac{Aq_i + B}{Cq_i + D} \tag{4.22}$$

[4]The number of intensity minima in x and y direction is labeled with n,m respectively.

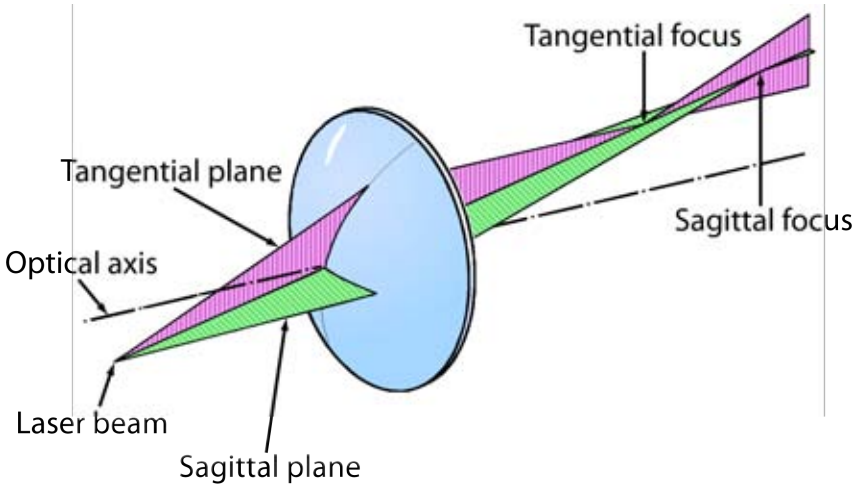

Figure 4.3 – Illustration of astigmatism for non orthogonal incidence on a curved optical device. The foci in the sagittal and tangential plane differ in position and waist (modified taken from [39]).

where q_i is the parameter for the incident beam and q_o is the parameter for the outgoing beam. For the description of the resonator depicted in figure 4.1 only two matrices are required, namely F for free propagation and M for a mirror:

$$F = \begin{pmatrix} 1 & L \\ 0 & 1 \end{pmatrix} \quad ; \quad M = \begin{pmatrix} 1 & 0 \\ -\frac{2}{R_e} & 1 \end{pmatrix} \tag{4.23}$$

Here R_e is the effective radius of the mirror curvature experienced by the beam. As depicted in figure 4.3 the tangential plane is defined by the beam and the optical axis whereas the sagittal plane is said to be the plane perpendicular to the tangential likewise containing the beam. The distinction between the sagittal and tangential plane is the effective radius of curvature experienced by a beam incident under an angle φ on a curved optical device with geometric radius of curvature R (astigmatism). The effective radius of curvature is given by $R_e = R\cos(\varphi)$ in the tangential plane and $R_e = R\cos(\varphi)^{-1}$ in the sagittal plane. $R_e = \infty$ for flat mirrors. Again self consistency requires that the beam has the same transversal intensity distribution after one roundtrip, i.e.:

$$q = \frac{A_T q + B_T}{C_T q + D_T} \tag{4.24}$$

where the matrix for one roundtrip (T) is generated by multiplication of the matrices of the individual elements $T = ...F_1 M_1$. By solving this equation one finds the q parameters describing stable Gaussian beams inside a given resonator. Without proof it should be mentioned that a small focus correspond to a configuration close to instability. An intuitive explanation for this stability regime is given in figure 4.4.

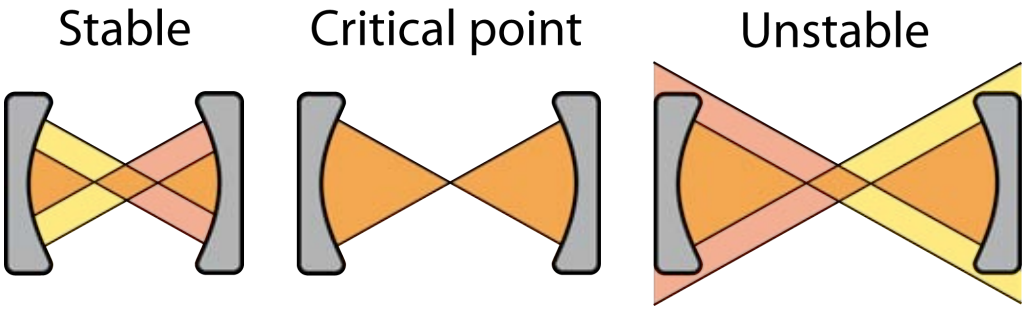

Figure 4.4 – Schematic representation of a symmetric two-mirror resonator which provides a focus. When the distance between both mirrors equals twice the radius of curvature of the two mirrors the two mirror foci coincide and the waist of the resonator mode is minimized. When the mirrors are brought closer together the beam waist becomes larger whereas extending the distance between both mirrors results in an unstable configuration since the resonator mode experiences strong losses. Please note that the stability region may be characterized by a large distance between two curved mirrors for a ring resonator.

4.1.4 Frequency stabilization

Every resonator has well defined resonance frequencies (longitudinal modes) which are enhanced inside the cavity whereas all other frequencies are strongly suppressed. To guarantee an efficient incoupling the laser frequency must coincide with the desired resonator mode. However, small fluctuations in the effective resonator length or laser frequency lead to a difference between the laser wavelength and cavity resonance. For high finesse cavities the difference between the laser frequency and the cavity resonance frequency very easily exceeds the linewidth of the cavity making an effective incoupling without an active feedback loop impossible. Such a feedback loop measures the deviation from perfect resonance and corrects either the resonator length or the laser frequency. The error signal describing these deviations needs to give information about the total amount and the direction of the deviations. For an error signal only describing the strength of the deviation it is not clear wether the laser frequency is above or below the cavity resonance frequency and hence the feedback loop can not correct the deviation. Therefore the error signal needs to be asymmetric around resonance.
A powerful technique available for this task is the Pound-Drever-Hall laser frequency stabilization (PDH locking technique). The theoretical basics of the error signal generation with this scheme will be outlined in the following. More details can be found in [4].
Neglecting the spatial dependence, the electric field right behind the laser source can be described by:

$$E = E_0 e^{i\omega t} \tag{4.25}$$

Modulating the phase of this electrical field sinusoidal with frequency Ω and amplitude β results in:

$$E = E_0 e^{i\omega t + i\beta sin(\Omega t)} \tag{4.26}$$

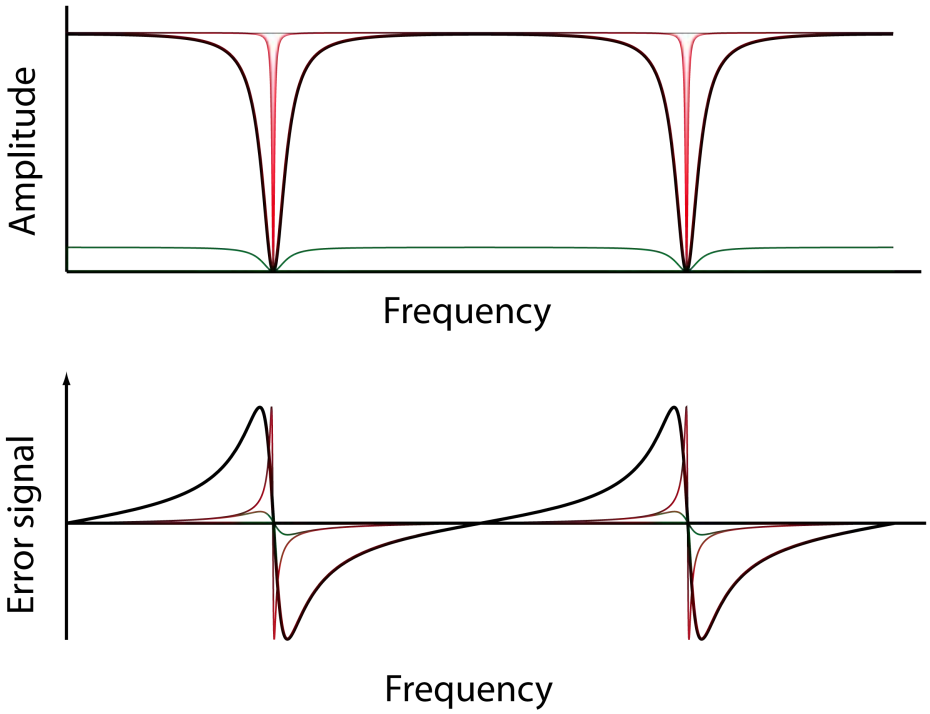

Figure 4.5 – Plot of the real (top) and the imaginary (bottom) part of equation 4.15 in the impedance matched case for different mirror reflectivities and field amplitudes (red: $r = 0.99$, $E_i = 1$ black: $r = 0.9$, $E_i = 1$ green: $r = 0.9$, $E_i = 0.1$). The lock is performed at the zero crossing of the imaginary part. Therefore a high finesse which leads to a short capture range as well as low signal strength wich causes a weak correction signal decrease the locking capability.

Using Eulers formula and the small angle approximation for small β the electrical field can be approximated as:

$$E \approx E_0 e^{i\omega t} + \frac{E_0\beta}{2} e^{i(\omega+\Omega)t} - \frac{E_0\beta}{2} e^{i(\omega-\Omega)t} \tag{4.27}$$

This equation shows that a sinusoidal phase modulation is equivalent to adding sidebands oscillating at frequencies $\omega \pm \Omega$.
Following subsection 4.1.1 the light observed as reflection at the incoupling mirror of a resonator is a coherent superposition of the light directly reflected and the leakage from the light inside the resonator. Comparing the reflected light with a phase reference therefore enables to extract the phase difference between directly reflected light and the light transmitted from inside the cavity. Sidebands can be used as the phase reference when the modulation frequency is large enough that the sidebands are totally reflected whenever the main frequency is near resonant. To extract the phase shift induced on the carrier frequency due to the presence of the resonator, the outgoing light at the cavity is monitored by a photodiode. Demodulating the signal with the frequency used for

sideband generation and filtering it with a low pass yields the error signal.
More precisely, the outgoing light at the incoupling mirror can be written as:

$$E_o = F(\omega)E_i \tag{4.28}$$

where the transfer function $F(\omega)$ is defined by equation 4.15. When plotting this function (figure 4.5) it can be seen that the amplitude of the reflected light ($\propto Re(F)$) is symmetric around the resonance whereas the phase ($\propto Im(F)$) is asymmetric and linear near the resonance, yielding the desired error signal.
The statement that the sidebands are totally reflected is equivalent to $F(\omega \pm \Omega) = -1$. Together with equation 4.28 and the special case of the incident light field in equation 4.27 the outgoing field from the cavity can be written as:

$$E_o = E_0 \left(F(\Omega)e^{i\omega} - \frac{\beta}{2}e^{i(\omega+\Omega)t} + \frac{\beta}{2}e^{i(\omega-\Omega)t} \right) \tag{4.29}$$

A photodetector measures the power which is proportional to the square of the absolute value of the field amplitude $|E_o|^2$. Neglecting terms quadratic in β (appropriate for small β) and using EulerŠs formula again, the power of the outgoing field at the incoupling mirror of the cavity can be expressed as:

$$\begin{aligned} P_o &\propto |E_o|^2 && (4.30)\\ &\approx |E_{i,0}|^2(|F(\omega)|^2 + i\beta[F(\omega) - F(\omega)^*]\sin(\Omega t)) && (4.31)\\ &= |E_{i,0}|^2(|F(\omega)|^2 - 2\beta Im[F(\omega)]\sin(\Omega t)) && (4.32) \end{aligned}$$

with E_i being the amplitude incident on the resonator. The photocurrent and hence the electrical signal S_r is directly proportional to the measured power. In order to extract the final error signal the photodiode signal S_r is demodulated with the (phase shifted) frequency for the sideband modulation in a frequency mixer[5] and low pass filtered which results in the dc component of the signal. Mathematical these steps are described by:

$$\begin{aligned} S_r &\propto |E_o|^2 && (4.33)\\ S_r^{mix} &\propto S_r \sin(\Omega t + \varphi) && (4.34)\\ S_r^{dc} &\propto -2|E_{i,0}|^2 \beta Im[F(\omega)]\cos(\varphi) && (4.35) \end{aligned}$$

In an ideal case no phase shifter to adjust φ is required but in most realistic situations a phase difference between the signals used to generate the sideband and for demodulation is present (e.g. due to different signal path length) which needs to be compensated. Finally the error signal is fed back to either change the cavity length or the laser frequency keeping the cavity in resonance with the laser frequency. An overview of the whole scheme can be seen in figure 5.6.
Translating the error signal into a change in resonance frequency respectively laser wavelength can be achieved via different methods. For example a piezoelectric element translating one of the resonator mirrors can correct for relatively large frequency deviations,

[5]Frequency mixing is mathematical described by multiplication of both signals.

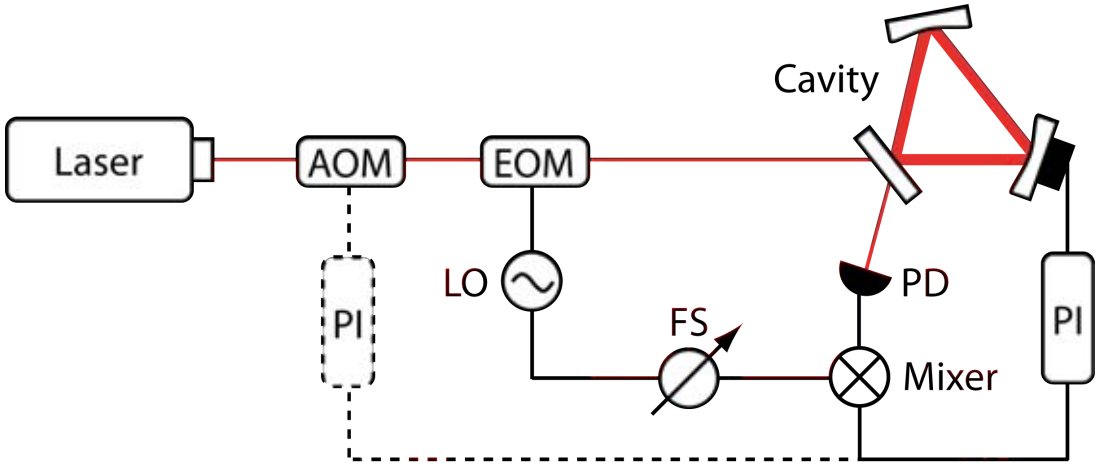

Figure 4.6 – Schematic overview of the Pound-Drever-Hall frequency stabilization. An electro-optical modullator (EOM) modulates sidebands on a laser beam incident on a cavity. The reflected light is collected by a fast photodiode (PD) and the signal is demodulated in the mixer with the EOM driving frequency from a local oscillator (LO). The error signal is fed into a PI controller which drives a correction element (a piezoelectric actuator at one of the cavity mirrors for instance).

i.e. changes comparable to the desired wavelength. Unfortunately the regulation bandwidth of piezoelectric actuators limits the correction speed to frequencies of some tenth of Kilohertz. By adding an acousto-optical modulator in the beam path and adjusting its driving frequency it is possible to tune the laser frequency by hundreds of Kilohertz with a bandwidth on the order of a Megahertz. Another option is to adjust the laser wavelength directly for example by means of changing pump diode current, the crystal temperature or the length of a laser cavity.

4.2 Design considerations

To enhance the efficiency of the evaporative cooling a novel scheme based on a dipole trap formed by a ring resonator will be implemented. The transfer of the atoms from the MOT into the dipole trap will be performed outside of the resonator focus at a rather large beam diameter whereas the evaporation is performed in the focal region which leads to enhanced thermalisation rates.
The two crucial points for an efficient loading are the trap depth and volume at the MOT position. For a given element and wavelength the first one only depends on the power inside the resonator which can be adjusted via the resonator finesse assuming a given available laser power and transfer volume. The transfer volume depends on the offset from the focus and the beam waist as can be seen from equation 2.12.
As mentioned in section 4.1.3 a small waist correspond to a configuration close to the instability region. For configurations close to the critical point, however, already small

changes in the resonator length may lead to an instable resonator. Therefore the minimal beam waist is determined by the ability to adjust and stabilise the resonator length[6]. For typical experimental situations a waist of approximately $20\,\mu$m is reasonable. For this minimal beam waist the loading volume only depends on the offset from the resonator focus. A small focus not only leads to a large loading volume but also yields high trap frequencies at the focus region which determine the thermalisation rate and thereby the efficiency of the evaporation.
The depth of the dipole trap is determined by the finesse of the resonator. The finesse also has an impact on the stability of the frequency lock as mentioned in section 4.1.4. To guarantee an efficient frequency stabilization and simultaneously a high enhancement a finesse of approximately 2000 was chosen for this resonator. A typical anti-reflection coating for vacuum viewports has a transmissivity of approximately 99 % which only allows for a finesse of maximal $F \approx 40$ when the resonator is placed outside the vacuum chamber (effectively eight viewports inside the resonator). The consequence of this is that the resonator has to be placed inside the vacuum which leads to strong restrictions for the mechanical design.
The controlled translation of the atoms in the interference pattern is induced by a frequency detuning $\delta\nu$ between the two counter propagating beams. The associated velocity is given by:

$$v = \delta\nu\lambda \tag{4.36}$$

This equation implies that during the transport at least one beam is not in perfect resonance with the cavity. However, in order to maintain a perfect interference pattern both beams inside the resonator have to be stabilized to the same intensity. As long as the detuning is not too large, i.e. comparable to the linewidth of the resonance, this can be easily achieved by monitoring both beams and correcting for differences in the circulating power by adjusting the power incident on the resonator.
Equation 4.36 also shows that the transport velocity is limited by the resonance linewidth of the resonator which is determined by the finesse. Another limitation for the velocity originates from the requirement that the transport should be adiabatic. An adiabatic transport is guaranteed when the corresponding time scales are much larger than the time scales associated with the oscillations of the atoms in the trap.

4.3 The design process

After the general considerations about the evaporation scheme in the last section a closer look on the specifications of the actual cavity will be given now. First the requirements on the resonator are summarized:

- A small focus is crucial since it not only leads to high trap frequencies for evaporation but also defines the divergence and thereby the volume at the MOT Position (for a given transport distance).

[6] The distance between the two curved mirrors is the sensitive length.

- A high finesse is required to achieve the desired trap depth. However, the finesse should not be so high as to make the frequency stabilization very challenging.
- A stable mounting of all parts is necessary to avoid instabilities through vibrations or misalignment over longer timescales.
- A piezoelectric actuator behind one mirror is required for frequency stabilization.
- The resonator must fit into the vacuum chamber.

In the following subsection it will be shown how the first statements influence the resonator geometry and mirror selection (4.3.1). This consequently leads to a specific design of the mirror holders which will be topic of subsection 4.3.2 where the stable mounting is discussed as well. Finally the problem of a suitable piezoelectric actuator is addressed (4.3.3). The vacuum chamber will be treated as a given restriction although the design was actually done in parallel.

4.3.1 Finding the optimal parameters

In this section it will be described in detail how the final resonator parameters were found. It starts with the choice of an overall geometry followed by a discussion of the specific lengths and angles. Finally the problem of finding appropriate mirrors is addressed.

Resonator type

A ring resonator with three or more mirrors is required to allow for the transport. Since the beam propagation in a ring resonator is not orthogonal to the curved mirrors the effective radius of curvature in sagittal and tangential directions are distinct (see section 4.1.2). The difference in the effective mirror curvature leads to an elliptical gaussian mode as can be seen from the propagation matrices (equation 4.23). The beam becomes more elliptical when the angles of incidence on the curved mirrors rises. Because of the ellipticity the beam waist differ in the both direction making it difficult or even impossible to create a very small focus in both directions. Therefore the angle of incidence on the two curved mirrors should be as small as possible.
The simplest ring resonator geometry providing a small angle of incidence on two curved mirrors is the bow-tie resonator already schematically depicted in figure 4.1. Nevertheless a non-negligible angle and corresponding ellipticity is inevitable due to the physical extent of the mirrors. For given mirrors this angle depends only on the distance between them. The minimal mirror diameter in turn depends on the beam divergence and the distance between the mirrors.

Resonator dimensions

A small focus implies that the resonator is very close to the instability region and the distance between the curved mirrors roughly equals the radius of curvature. Since high quality mirror substrates[7] are only available with certain radii of curvature this require-

[7] Here super polished substrates from *ATFilms* are chosen.

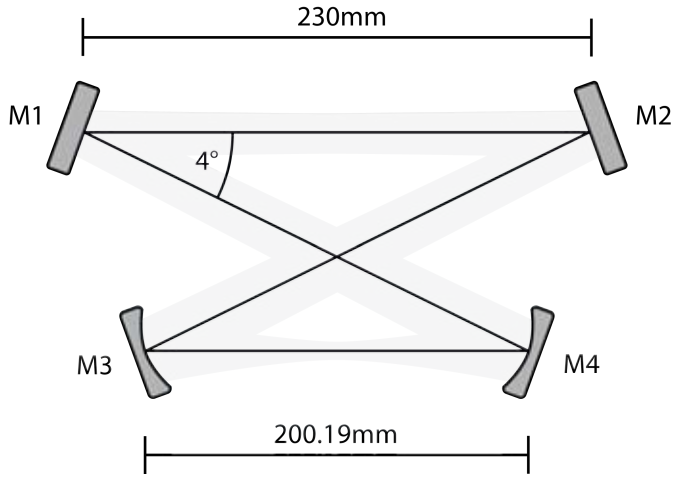

Figure 4.7 – Overview of the resonator specifications. The radius of curvature of mirrors M3 and M4 is 200 mm, M1 and M2 are plane parallel. The reflection coefficient for 1064 nm radiation are measured to be approximately $99,85\,\%$ for M1 and M2 and $99,998\,\%$ for M3 and M4 respectively.

ment restricts the size of the resonator to these particular values. Other limitations to the mirror distance arise from the fact that the whole resonator has to be placed inside the vacuum chamber.
After some iterations finally the values given in figure 4.7 turned out to give the best compromise satisfying the requirements. A calculation of the beam radii in both directions for this configuration can be seen in figure 4.8. The program used relies on equations 4.22 to 4.23 and was developed by Robert Jördens. It can be seen that the beam waist is $20 \times 30\,\mu$m whereas the radius at the MOT position is $230 \times 340\,\mu$m. The choice of the right MOT position relies on many parameters such as sufficient beam waist, optical access and so forth and was found to be optimally located 20 mm away from the resonator focus.

Mirror reflectivities

The resonator will be placed inside the vacuum chamber. Therefore losses inside the cavity can be neglected and the finesse only depends on the reflectivity of the resonator mirrors. Since the beam at the curved mirrors is strongly divergent the incoupling and power monitoring will be performed at the plane parallel mirrors[8]. For this reason the curved mirrors are chosen to be highly reflective and the finesse is determined by the plane parallel mirrors only. Taking the requirement for impedance matching ($r_1 = r_2 r_3 r_4$) into account the reflectivity of these mirrors should be approximately equal and given by $|r_i|^2 = 99,85\,\%$. The transmission curves as measured by the manufacturer are shown

[8] Only once the beam divergence is measured at one curved mirror in order to calculate the exact beam waist.

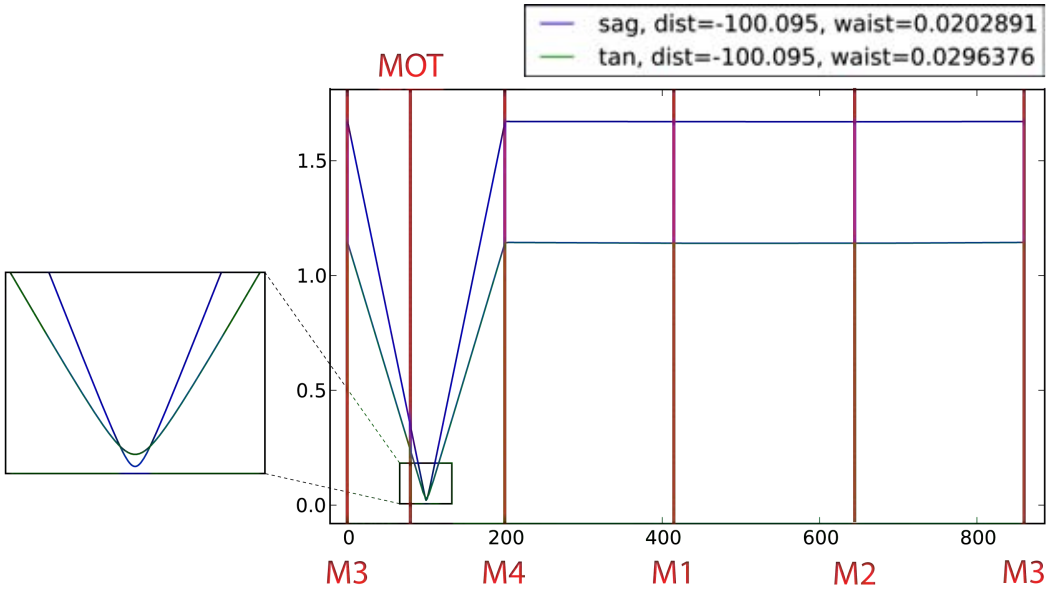

Figure 4.8 – The calculated beam radius (in mm) in sagittal (blue) and tangential (green) direction for the resonator geometry indicated in figure 4.7. The inlet shows that tight focussing is equivalent to strong divergence.

in figure 4.9. For the plane parallel mirrors a reflection coefficient of approximately $|r_i|^2 \approx 99.85\,\%$ and for the curved mirrors of approximately $|r_i|^2 \approx 99,992\,\%$ is specified for a laser wavelength of 1064 nm. With equation 4.10 this yield a finesse of approximately $F \approx 1987$. The free spectral range of the resonator can be calculated with the resonator length $L \approx 0.86\,\mathrm{m}$ to be $\Delta\nu_f \approx 349\,\mathrm{MHz}$. This free spectral range together with the finesse gives a resonance linewidth of $\Delta\nu_l \approx 176\,\mathrm{kHz}$. The transport of the atoms from the MOT position to the focus thus takes a minimal time of approximately 0.2 s for $\delta\nu = 0.5\Delta\nu_l$. With the mirror reflection coefficients given above an enhancement of roughly $\varepsilon \approx 633$ is calculated. For ^{6}Li, a laserwavelength of 1064 nm and a realisitc power per beam of 1 W this enhancement lead to a maximal trap depth at the MOT position in the two counter-propagating beams of approximately $T \approx 1.2\,\mathrm{mK}$ and trap frequencies of $\omega_x \approx 1.8\,\mathrm{kHz}$, $\omega_y \approx 1.2\,\mathrm{kHz}$ and $\omega_z \approx 1.7\,\mathrm{MHz}$ respectively. The same calculations for the focus position with only one beam yield a maximal trap depth of $T \approx 40\,\mathrm{mK}$ and trap frequencies of $\omega_x \approx 119\,\mathrm{kHz}$, $\omega_y \approx 79\,\mathrm{kHz}$ and $\omega_z \approx 1.1\,\mathrm{kHz}$ respectively.

4.3.2 Mechanical realization

For the mechanical mounting of the mirrors many constraints have to be fulfilled. The strongest restriction is that the resonator has to be placed inside the vacuum because this limits the available space to the inner dimensions of the chamber. The vacuum also influences the choice of material since outgassing has to be avoided. Even more restrictions follow from the fact that the optical access for all desired beams has to be

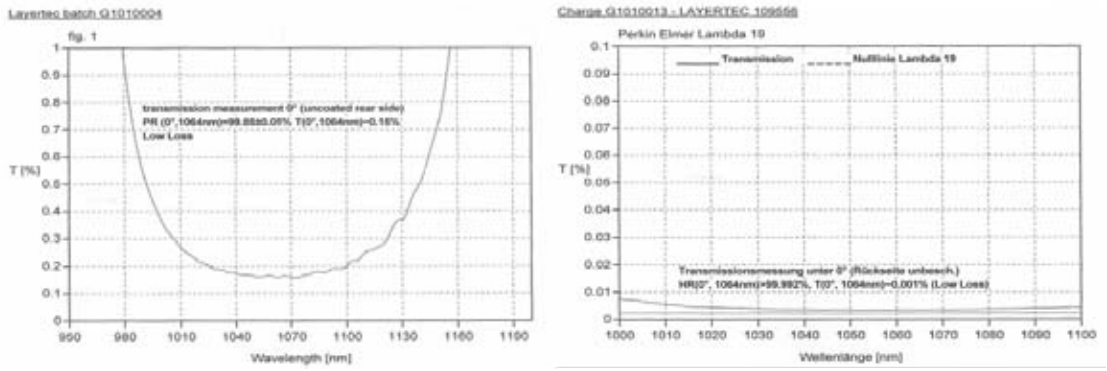

Figure 4.9 – The transmission coefficient for normal incidence for the plane parallel mirrors (left) and for the curved mirrors (right) as measured by *Layertec*. At a wavelength of 1064 nm the power reflection coefficients $|r|^2$ are specified to be $99.85 \pm 0.05\,\%$ and $> 99.992\,\%$ respectively.

kept free. Overviews of the whole resonator assembly as planned and manufactured can be seen in figure 4.10 and 4.12 respectively. In the following a detailed description of the design process is given. The mounting of the piezoelectric actuator is discussed separately in subsection 4.3.3.

Orientation

The direction of the focused resonator beam and thereby the position of the mirrors is defined by the axis of transport to the final experiment. The reason for this is that a good overlap between the elongated dipole traps of the resonator and for transport is crucial to assure an efficient loading of the transport trap from the resonator trap. Consequently a small angle between both beams is favorable. This angle was minimized to be approximately $25\,°$. Thus a perfect overlap is not given but this should not matter too much since the atoms should flow from the resonator trap into the focus of the transport beam when the resonator trap is ramped down and the transport dipole trap is simultaneously ramped up.
Another point to be kept in mind when positioning the individual mirrors is that the whole resonator roundtrip should lie within one plane. Otherwise the polarization will change in a way not well controllable which then also influences the resulting interference pattern. Taking the available space into account this plane was found to be optimally situated when tilted by $8\,°$ with respect to the vertical plane.

Mounting

For aligning and testing purposes the whole resonator will be assembled outside the vacuum chamber and afterwards inserted without realigning. This requires stable mounting of all mirrors on the same ground plate. The ground plate can be seen in figure 4.10.

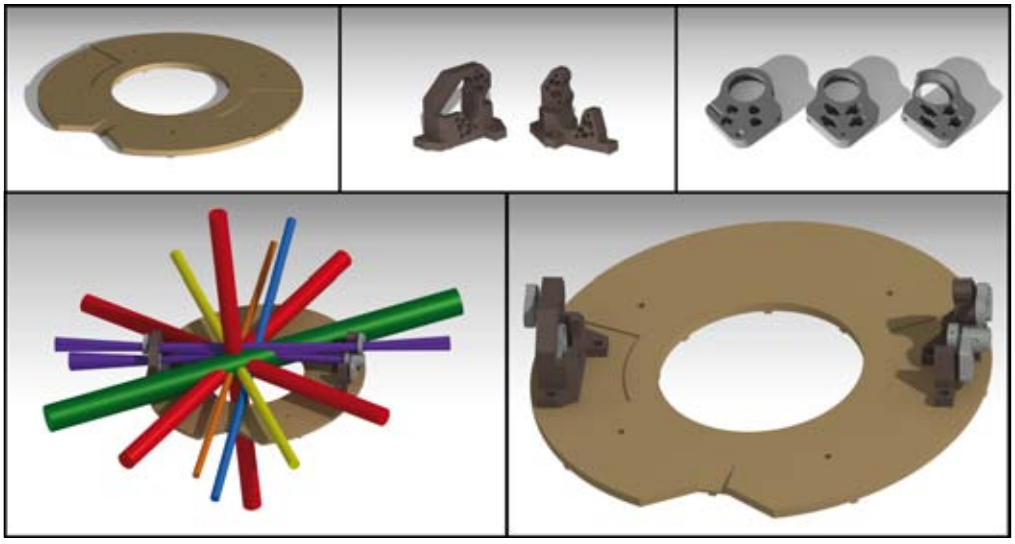

Figure 4.10 – CAD drawings of the resonator ground plate, the mirror hosts and the individual mirror holder (top, from left to right). In the lower panel the assembled resonator (right) with all rays crossing the main vacuum chamber (left) is shown.

The large hole in the middle and the groove in the front of the drawing are included to maintain all optical access, which also limits the overall height of the ground plate. To avoid virtual leaks the ground plate only stand on small bridges ($0,5\,\mathrm{mm}$ wide). It is fixed to the bottom chamber flange by the thread sticks welded on the bottom chamber flange.
It is convenient to fix the two mirrors of each resonator side to one common structure (host) which is mounted on the base plate. The mirror holders will be held by four strong springs where the adjustment is enabled by three fine threading screws. Although the resonator alignment will be performed outside the vacuum chamber the screws should be accessible after inserting the resonator into the chamber in order to enable readjustment. Therefore the mirrors are mounted behind the hosts (looking from the focus). Of course it is important that none of the beams inside the chamber is blocked by the hosts which is especially important for the incoupling and monitoring beams as well as the circulating beams itself. The hosts created for this purpose are shown in figure 4.10 and figure 4.12. It can be seen that the holes designed for the mounting on the base plate are elongated. The elongated holes makes it possible to adjust the length of the resonator and thereby the beam waist on a larger scale than it is possible with the adjustment screws.

Mirror holders

The mirror holders themselve have to satisfy constrains in addition to the spatial limitation. First of all the back sides of both plane parallel and one curved mirror have to be accessible to enable incoupling, power and mode monitoring respectively. The fourth

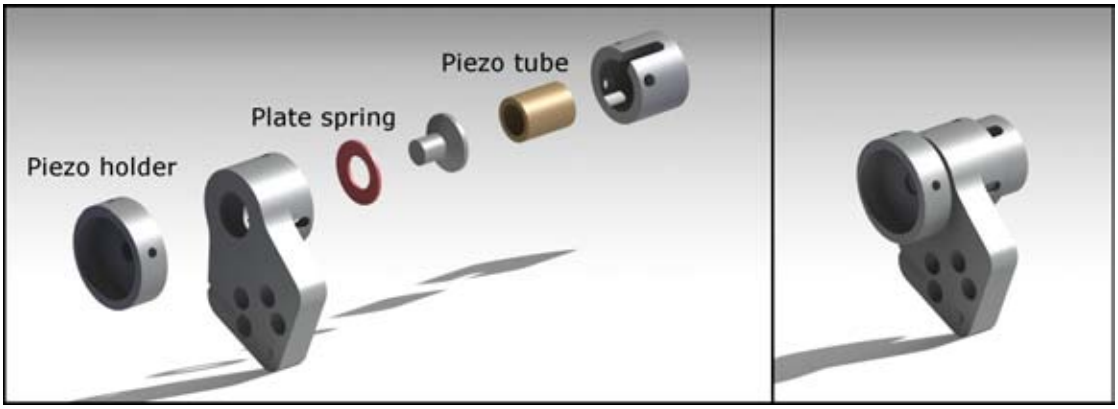

Figure 4.11 – CAD drawings of the holder designed to mount a mirror on the piezoelectric actuator without glue. The mirror holder is clamped to the piezoelectric tube with the help of a plate spring. To not damage the piezoelectric material during assembling it is important that no shear forces or radial load is applied to the piezoelectric tube.

mirror will be equipped with a piezoelectric actuator for frequency stabilization which will be the topic of subsection 4.3.3.
Optimal adjustability is achieved via three screws. It is important that the center of the spring forces fixing the holders to the hosts lies within (most likely centered) the triangle formed by the screws to ensure proper tilting in both directions as well as translation. For optimal position stability it is convenient to restrict the movement of the screw tips on the holder by providing a cone for one screw (fixed position) and a groove for one other (one-dimensional movement) as can be seen in figure 4.10. The mirrors are fixed to the holders by setscrews. At the side opposite to the set screw an off-center bore ensures that exactly two contact points exist which guarantee stable positioning.

Adjustment screws

The mirror adjustment screws provide a problem not yet mentioned. In the vacuum of course no grease can be applied but still an easy and precise adjustment has to be ensured. Precise adjustment without grease, however, is impossible when the threading hole and the screw are made from the same material. Since stainless steel is used for the base plate the mirror holders and the hosts some different, self lubricating material is required for the screws which shows only small outgassing. A bronze alloy (CuSN8P) was chosen for this purpose. The specially manufactured screws are depicted in 4.12: the tip consists of a stainless steel ball which is inserted in a cone at the front end of the screw.

4.3.3 The piezoelectric actuator

For the PDH lock the resonator length has to be adjustable in order to correct for fluctuations. A convenient way to do this is to mount one of the mirrors on a piezoelectric actuator. Since power monitoring and incoupling are performed with light transmitted through the flat mirrors a curved mirror is equipped with the piezoelectric tube. For the performance of the stabilization this is a good choice as well since the distance between the two curved mirrors is the sensitive length.

Piezo electric material

Since the piezoelectric effect depends on the electric field amplitude stack type actuators are typically used because they allow for large length variations with low voltages. Unfortunately such stacks need to be isolated for testing purpose under atmosphere, yet most isolation materials are not compatible with UHV conditions[9]. For one-crystalline piezoelectric tubes the expansion is given by:

$$\Delta L \approx d_{31} L \frac{U}{d} \tag{4.37}$$

where U is the applied voltage and d the wall thickness. The material NCE55 from *Noliac* offers a high piezoelectric coefficient of $d_{31} = -260 \times 10^{-12}\,\mathrm{CN}^{-1}$ and is available with custom specifications. A special size is required since the space behind the mirrors is strongly limited and standard tubes where not available with the given dimensions. A tube of 9 mm length with a wall thickness of 1 mm thus allows for a length variation of approximately 1000 nm when a voltage of ± 200 V is applied.

Piezo tube holder

Since glues have considerable outgassing rates and limited long time stabilities a purely mechanical mounting was designed. For the construction of a mount for a piezoelectric actuator attention has to be paid to the fact that piezoelectric materials are very sensitive to shear forces and radial pressure. Therefore the only possibility to properly mount the tube without glue is to strongly clamp it in longitudinal direction. Additionally this preload enhances the resonance frequency and thereby the speed of the piezoelectric actuator. Because of their small size and relatively strong forces plate springs are optimally suited to clamp the piezoelectric tube. The contact planes of the plate springs form a cone to ensure that the plate springs and thus the piezoelectric tube stay on the translation axis and no tilting is possible.
The mirror holder designed to hold the piezoelectric actuator can be seen in figure 4.11. During assembling it is crucial to ensure that the two parts clamping the piezoelectric tube are not rotated with respect to each other. Instead only the part to fix the holder at the hosts should be moved. Of course it is important that the wires delivering the voltage are isolated with kapton which is an UHV suitable plastic.

[9] *Physical Instruments* specifies their *Picmar ceramics* to be UHV suitable but to our knowledge this was never been tested under comparable experimental conditions.

Figure 4.12 – Pictures of the manufactured elements for the resonator. A Euro coin is shown for scale reference. The small *wall* on the right side of the lower hole in the left host prevents the titanium sublimation pump from deposing titanium on the mirror surface.

5 Testing the resonator

To reach the desired trap depth for evaporative cooling with moderate laser power the enhancement of a resonator placed inside the vacuum chamber is used. The utilized cooling scheme demands for precise control of the power and frequency in the two incoupled beams. The control of the frequency is necessary to enable the transport and the frequency stabilization whereas the power has to be adjustable in order to enable the evaporation and to hold the power in both beams constant during the transport. Therefore sophisticated control electronics (5.2) and an appropriate optical setup (5.1) are required.
A crucial point for every cavity is the frequency stabilization which is especially challenging for a large high finesse cavity like the cavity employed in this experiment. To guarantee the feasibility of the locking scheme as planned a setup including all desired elements was built. First measurements characterizing the resonator and the feedback loop are performed on this setup and presented in the final section (5.3). Although there are some theoretical details on a few elements the focus of this chapter lies on the work in the lab. It should be pointed out that all the work was performed on a test setup and some details may still be changed.

5.1 Optical setup

The optical setup for the operation of the cooling resonator includes the EOM which generates the sidebands for the Pound-Drever-Hall frequency stabilisation and two AOMs which are employed to prepare the two beams for the resonator as well as beam shaping optics and mirrors to guarantee an efficient incoupling. Before setting up the test system an overview of the optical table including all elements potentially affecting the plans for the cooling resonator optics was drawn. In particular this was necessary since the same high power laser source will be utilized for the cooling, transport and manipulation of atoms. Several main components are described at the end of this section (5.1.2 to 5.1.5) in detail but first the whole optical system is summarized (5.1.1).

5.1.1 Layout of the optical setup

The optics for the preparation of the two beams which are coupled into the resonator are placed on the same optical table as the vacuum system and the cavity. The laser radiation is provided by a high power solid state laser with a very good beam profile. Nevertheless beam shaping optics are planned to guarantee an efficient incoupling. The optical setup also include two acousto-optical modulators (AOM) which will be utilized for the power control of both beams and together with an electro-optical modulator (EOM) form the

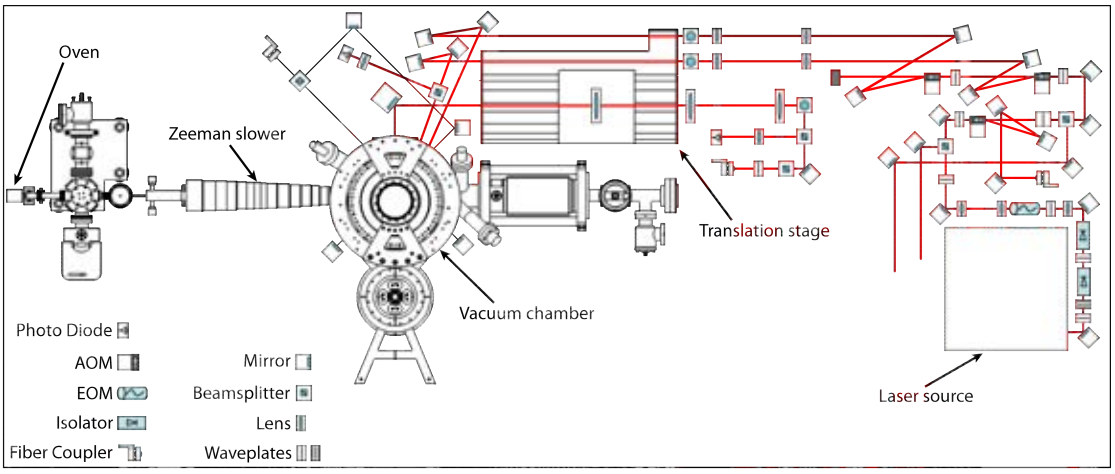

Figure 5.1 – A scaled view of the experimental table as planned so far. The dimensions of the table are: $3.5 \times 1.5\,\mathrm{m}$. The vacuum system and the optical setup are shown. For a detailed discussion see text.

fast part of the feedback loop. Additionally the beam preparation for the dipole trap employed to transport the atoms into the glass cell is considered since it strongly affects the space available for the other elements. In the following a detailed overview of every element in the beam path is given.

A sketch of the experimental table as planned so far can be seen in figure 5.1. A Nd:YAG solid state laser generates approximately 25 W of laser light at a wavelength of 1064 nm (for details see 5.1.2). An optical isolator is placed right behind it to prevent back reflections into the laser. Since optical isolators are polarization dependent, wave plates are used to adjust for best transmission. In fact, every polarization dependent element like EOM, AOM and polarizing beam splitter has a wave plate in front of it to set the right polarization. Additionally, space is kept free for a second, optional optical isolator in case the present 35 dB attenuation is insufficient.

The next main element is an electro-optical modulator which generates the phase modulation for the Pound-Drever-Hall (PDH) signal. The first acousto-optical modulator splits off the laser beam for the transport dipole trap. This is then coupled into an optical fiber to maintain a perfect TEM_{00} mode. At the outcoupling port of the fiber a polarizing beam splitter for polarization filtering and power monitoring via a photodiode follow before the beam is expanded and focused into the chamber by a lens mounted on the translation stage.

At the main beam path the AOM is followed by a wave plate, which can be rotated by a small motor, and a beam splitter. One of these beams is then guided away for further use. The beam splitter is followed by two AOMs providing the two beams for the cooling resonator. Both beams are then guided through a telescope for better mode matching and a periscope which shifts the beam path to the height of the resonator in the vacuum chamber (28 cm).

The final incoupling is achieved via two independent mirrors for each beam to ensure full

control over direction and position of the beam at the incoupling mirror (beam walk). Two wave plates with polarizing beam splitters are used to ensure the right polarization and thereby a clean interference pattern inside the resonator (not shown). The beam splitter and the photodiode provides the signal for the PDH lock explained in 4.1.4.
Some mirrors for the incoupling of the MOT beams were also considered. Two photodiodes for monitoring the intensity of each beam independently (required for the power control) are placed behind the outcoupling port of the resonator (not shown).

5.1.2 The laser source

The laser source utilized for the evaporation dipole trap has to fulfill some requirements. For example a narrow linewidth is desirable in order to enable an efficient incoupling into the high finesse cavity and good frequency stability is favorable to relive the Pound-Drever-Hall feedback loop. Additionally high power is necessary to generate a deep trap for evaporation. Even more power is necessary since the same laser source will also be used to form the dipole trap for the transport of the atoms into the glass cell and to generate optical lattices in the glass cell. In the final setup a 25 W *Mephisto* [36] laser system from *Innolight* will be used for this purpose but in the test setup a much smaller version with only 200 mW output power is employed. However, most other specifications are comparable and it will be referred to the 25 W version in the following.
The high power *Mephisto* systems consists of a Nd:YAG (neodymium-doped yttrium aluminum garnet) solid-state laser [34] followed by additional optical amplifiers. This so-called master oscillator power amplifier (MOPA) approach preserves the advantages from a single weak laser source while quite high powers can be reached[1]. For example a very good single mode (TEM_{00}) operation and beam profile is specified. The laser emits at a wavelength of 1064 nm with a narrow linewidth of only 1 kHz. Two options for frequency tuning are included: The effective cavity length can be changed by a piezoelectric actuator leading to a frequency tuning range of ± 100 MHz and a response bandwidth of 100 kHz. A change of the laser crystal temperature leads to a tuning range of 30 GHz where the response bandwidth is limited to approximately 1 Hz. In the test setup the lock was performed only with the piezoelectric actuator and the temperature control was utilized for manual adjustment. Other important characteristic of this laser source are the frequency stability (specified to approximately $17\,\mathrm{kHzs}^{-1}$) and the very low intensity noise ($< 0.2\,\%$rms from 10 Hz to 2 MHz).

5.1.3 Electro-optical modulators

For the Pound-Drever-Hall frequency stabilization scheme a modulation of the phase of the laser light is necessary. This phase modulation is generated by an electro-optical modulator. In general every device which modulates the properties (phase, frequency, amplitude, polarization) of a beam of light by use of an applied electric field is called an electro-optical modulator (EOM). Here, however, EOM refers to what more precisely is

[1] Diode stacks and fiber lasers with comparable powers for instance typically show much worse beam profiles.

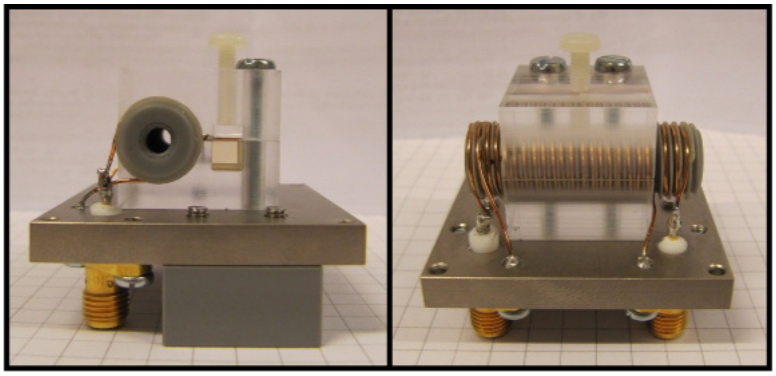

Figure 5.2 – Pictures of the EOM employed in this setup. In the front view (left) the crystal can be seen. The three coils for incoupling and monitoring are wrapped on a common structure (right). Everything is fixed with an isolating structure.

an electro-optical phase shifter.
An electro-optical phase shifter consists of a crystal whose refractive index and the related speed of light depend on the local electric field (Pockels effect, Kerr effect). The phase of a laser beam behind a crystal in turn depends on the optical path length. Therefore an EOM can modulate the phase of the outgoing laser beam by modulating an external electrical field [13].
Pictures of the EOM employed in this experiment during assembly can be seen in figure 5.2. The electrical field is generated by a parallel plate capacitor placed across the crystal. Together with a coil it forms a resonant circuit enhancing radio frequencies which are coupled in through a second coil from an external source. A third coil can be used for monitoring. The measured resonance frequency of this EOM is 68 MHz with a linewidth of 1 MHz.

5.1.4 Acousto-optical modulators

An acousto-optical modulator (AOM) can be used to tune the frequency and amplitude of a laser beam. In the frame of this work AOMs are utilized for the fast part of the Pound-Drever-Hall frequency stabilization and the frequency control enabling the transport as well as for the power control. Figure 5.3 schematically shows the working principle of a typical acousto-optical modulator. A piezoelectric actuator is mounted on a transparent material such as glass. When an oscillating voltage is applied to this actuator it starts vibrating and thus generates a sound wave inside the glass. Back reflections are suppressed by an acoustic absorber on the opposite side. The acoustic (density) wave inside the material causes a periodic change in the refractive index. This acts as a grating to an electro-magnetic wave traveling perpendicular to the acoustic wave leading to typical diffraction phenomena.
The power in the diffracted beams can be adjusted by the amplitude of the acoustic wave. With a thin piece of material, pure sinusoidal modulation and careful adjustment

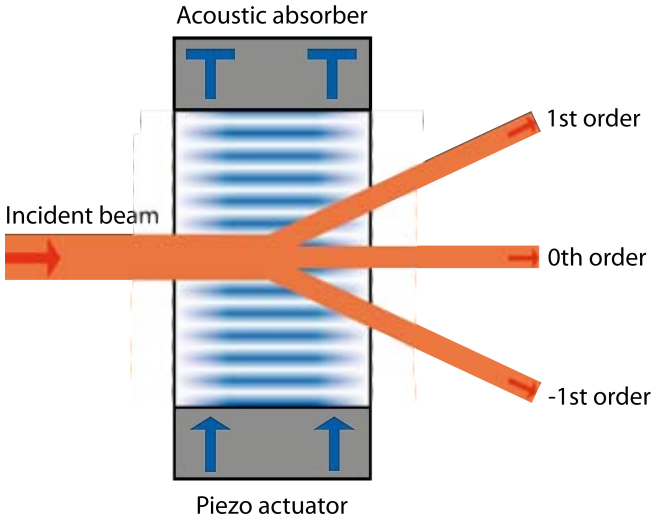

Figure 5.3 – Working principle of an acousto-optical modulator. The vibrations of a piezoelectric actuator lead to a travelling density wave inside a piece of glass. A beam of light will diffract at the grating formed by the density wave and the resulting modulation of the refractive index respectively. In contrast to Bragg diffraction at conventional gratings the frequencies of the diffracted beams in an AOM are shifted due to the conservation of momentum in the photon-phonon interaction which causes the diffraction in a quantum-mechanical picture.

up to 90 % can be diffracted into the first order depending on the specific AOM.
An important difference to conventional Bragg diffraction is the traveling wave nature of the grating which leads to a Doppler shift in the diffracted beams. In other words, momentum and energy are conserved in the photon-phonon interaction. The frequency shift is given by the modulation frequency and can vary between approximately ten and a few hundred Megahertz for different types of AOMs. This effect also makes it possible to tune the laser frequency by changing the AOM driving frequency. Please notice that in a given optical setup the frequency can only be tuned by up to a few MHz since the angle of diffraction is also dependent on the frequency so that a large shift would result in misalignment.
In many applications the speed of an optical device is a crucial point. For AOMs this only depends on the beam radius and the speed of sound inside the material and can be rather fast. For the AOM used in this setup a reaction time of approximately 0.37 μs is expected. For this test setup a AOM with a driving frequency of 80 MHz was used[2]. The maximal observed diffraction efficiency was near 85 % where it was obvious that further improvement is possible.

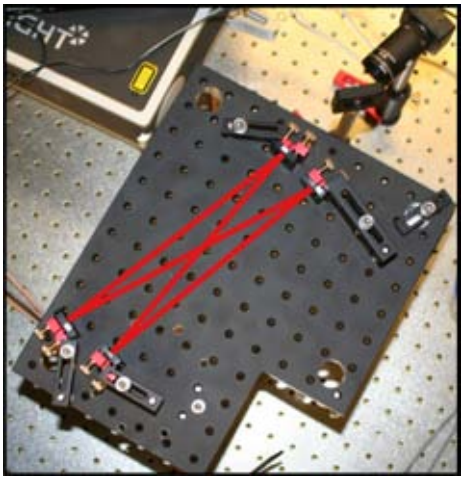

Figure 5.4 – The resonator test setup with the drawn beam path. The CCD camera is visible in the upper right corner.

5.1.5 The test resonator

A sophisticated cavity was designed to ensure good mechanical stability and a suitable resonator geometry. Unfortunately the production of the mirror holders was not finished when the work in the lab started so that a test resonator was built. It consists of the final mirrors but conventional mirror holders. It was tried to make this test resonator geometrically as similar to the final resonator as possible but some differences where inevitable. For example, the angles between the different beams where larger due to the larger mirror holders. Also the distance between the two curved mirrors was larger resulting in an optically more stable configuration but also in a larger beam waist. A more serious difference between the final resonator and this setup was the obviously much greater mechanical instability of the latter one. Additional no piezoelectric actuator was mounted at the resonator mirrors such that the locking was implemented by changing the laser wavelength directly. In the final setup the frequency stabilization will not be performed by tuning the laser frequency since the laser has to be locked simultaneous to different cavities.
For the alignment of an infrared resonator team work is recommended since observation of the beam and adjusting the elements needs more than two hands. The alignment was performed in the following way: First of all, the two flat mirrors were lined up with the last mirror before the resonator such that all of them were centrally hit by the beam. For the observation of the beam behind the incoupling mirror the room has to be darkened and the utilized infrared viewer card needs regular recharging. As a second step also the curved mirrors were placed and an approximate roundtrip is achieved by moving the mirror holders.
Once this is done, the holders are fixed tightly onto a ground plate and further adjustment is performed with the appropriate screws at the resonator. By guiding the main

[2]Gooch & Housego: I-FS080-2S2G-3-LV1, Inventory: QM-00079

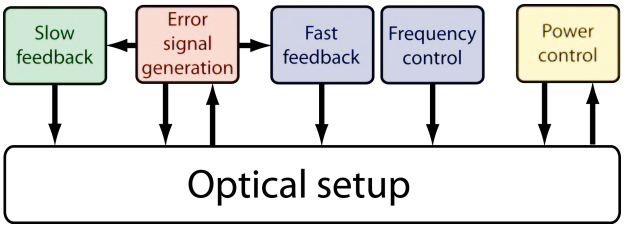

Figure 5.5 – Schematic overview of the electronic scheme employed for the operation of the cooling resonator. The error signal generation is discussed in detail in section 4.1.4. The slow part of the feedback loop will be implemented through a piezoelectric actuator translating one of the resonator mirrors whereas the fast part will be implemented with two AOMs placed in the beam path. The frequency control to make the controlled transport of the atoms inside the resonator possible and the power control to enable the evaporative cooling will be implemented through the same AOMs as the frequency stabilisation.

beam inside the resonator through a small hole in the viewer card the light of higher order roundtrips can be observed. This is brought to overlap with the main beam by successively adjusting each mirror. When no further improvement was possible in this way a CCD camera was placed behind the second flat mirror. After some adjustment of the incoupling (remember the original mirror positions!) the TEM_{00} mode could be observed and optimized to a certain extend.
Since observation of the light transmitted by the resonator with a viewer card is impossible in the unlocked mode, then the monitoring of the reflected light was set up. Once the resonator is locked a photodiode can be added behind the outcoupling mirror giving precise information on the power circulating inside the resonator. Now the incoupling can be improved again by carefully adjusting each mirror. Finally the monitoring of the reflected light has to be readjusted.
The incoupling of the second beam was not performed but it should be easier since the resonator stays unchanged and the requested overlap with the reflected part of the first beam should help.

5.2 Electronic setup

For every resonator electronics are necessary to realize the frequency stabilization. For the resonator discussed in this thesis even more electronics are needed to realize the transport and evaporation for the novel cooling scheme (figure 5.5). The frequency stabilization scheme implemented for this resonator can be divided into three parts. First a Pound-Drever-Hall error signal is generated by demodulating the light reflected on the incoupling mirror of the cavity with the local oscillator which drives an EOM modulating sidebands on the incident laser beam. Second a slow feedback is realized with a piezoelectric tube translating one of the cavity mirrors such that rather large disturbances can be corrected by changing the resonator length. Finally a fast feedback

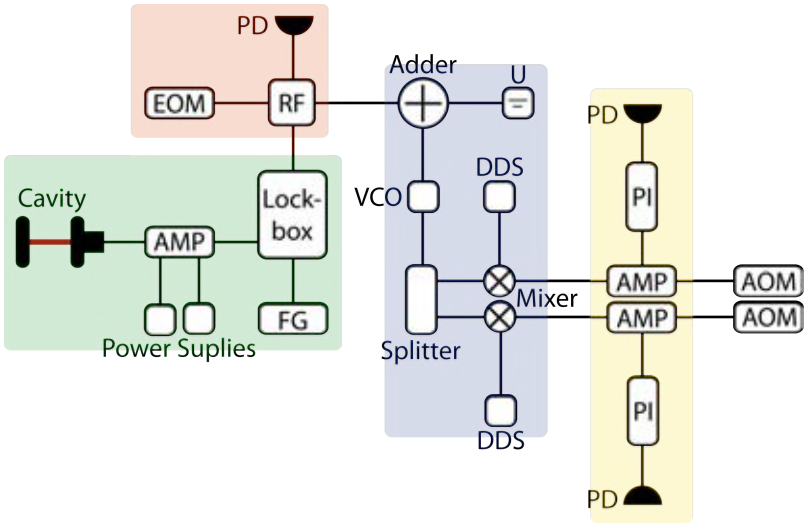

Figure 5.6 – Detailed overview of the electronic scheme employed for the operation of the cooling resonator. One sees the elements for the error signal generation (red) and the slow part of the feedback loop (green) as well as the frequency (blue) and power (yellow) control for the AOM driving frequency. The given abbreviations stand for: PD = photodiode; RF = RF-lock; AMP = amplifier; FG = frequency generator; PI = PI-controller; U = DC voltage source. For further explanations see text.

is implemented with an AOM placed in the beam path which shifts the laser frequency when the AOM driving frequency is changed. The AOM can only correct deviations from resonance with a relative small amplitude but it perfectly complete with the slow feedback by the piezoelectric element. For the evaporative cooling it is necessary to lower the power circulating in the cavity. The power control for this purpose is realized by adjusting the amplitude of the driving frequency for the two AOMs which splits up the power for the two resonator beams from the primary laser beam. The same AOMs are used to realize the fast part of the frequency stabilization and additionally to introduce the frequency difference between both beams which is necessary for the transport. In the following subsections a detailed overview of this electronic scheme is given (5.2.1) before some comments on PI controllers (5.2.2), the lock-box (5.2.3) and photodiode front ends (5.2.4) are made.

5.2.1 Overview of the electronic setup

Figure 5.6 schematically shows the single elements of the electronic setup. It can be distinguished between error signal generation, elements for the slow part of the frequency stabilization with the piezoelctric actuator of the cavity and the AOM control. The two AOMs are employed to simultaneous realize the fast part of the frequency stabilization scheme and the frequency control for the transport as well as for the power control for evaporation.

The error signal generation was already discussed in section 4.1.4. We find an EOM modulating the sidebands, a fast photodiode for signal collection and the RF-lock containing the local oscillator and the mixer as well as a low-pass filter. The radio frequency at the local oscillator can be adjusted in order to match the EOM resonance.
The control of the piezoelectric actuator mainly consists of the lock-box (with an external frequency source) which will be discussed in 5.2.3. Since the piezoelectric element needs high voltage (±110V for the full range) the signal coming from the lock-box needs further amplification. A high voltage operational amplifier[3] together with two 110V low noise power supplies[4] is used for this purpose.
The most complicated part of the electronics is the AOM control for the two beams. The AOMs are used to realize the fast part of the PDH feedback loop. The signal for the frequency stabilization is directly taken from the RF-lock and only high-pass filtered in order to avoid any slow element. It is added to a constant voltage. To ensure that the error signal has the right sign and amplitude adjustment of both is enabled. This signal is used to drive a voltage controlled oscillator (VCO). For the frequency stabilization it is convenient to use the frequency generated by the VCO to drive the AOMs which will then adjust the frequency of the light incident on the cavity for optimal resonance. However, for the moving interference pattern a well controllable offset between the two AOM driving frequencies is required. For this reason the VCO signal is divided and mixed with two other distinct, adjustable frequencies. These frequencies will be generated by two direct digital synthesizers (DDS) combined on a single chip which allows very precise phase and frequency adjustment via a computer. After appropriate filtering and amplifying the resulting sum respectively difference frequencies can be used to drive the AOMs in the desired way. In addition to this frequency control the AOMs are also used to adjust the power circulating in the resonator. For this purpose two photodiodes monitor the power in the individual modes. A simple PI controller (see section 5.2.2) compares the signal to some set value given by a computer and generates an error signal. This tunes the gain (amplification factor) of two final amplifiers giving the desired amplitude at the AOMs.

5.2.2 Controller

The task of a controller within a feedback loop is to process the error signal into an appropriate correction signal.
The simplest possibility doing this is to output a signal proportional to the error. Two drawbacks are connected to this: firstly a residual deviation from the set point is inevitable and secondly, caused by the limited speed of electronics the feedback loop will perform a damped oscillation. This is even worse when the error signal is modulated with the oscillation frequency since then the error will be enhanced. Therefore a low gain at this frequency is preferable whereas the gain at low frequencies should be as high as possible for fast damping of the oscillations.
An integrator provides a gain decreasing with frequency since it accumulates the error signal over time which only for low frequencies gives a noteworthy contribution.

[3] Cirrus Logic: PA 85-IC OP-AMP.
[4] Kniehl: CAHV 110.0,55, Inventory: QM-00078.

When combining this with a proportional part (PI-controller) the desired behavior can be achieved.
The frequency where noise will be perfectly enhanced is characterized by a phase delay of 180 ° and is determined by the speed of the used electronics and the controlling element. The circuit of such a PI-controller consisting of appropriate wired operational amplifiers. Formulas for the right dimensioning of the electronics and a detailed discussion of everything outlined above can be found in every good electronic book such as [15] and [35].

5.2.3 The lock-box

The controlling unit of the feedback loop in this experiment is called lock-box. In principle it is a PI-controller supplemented by an alternative *dither mode* and some elements for comfortable operation. In the dither mode an alternating voltage is generated at the output where the frequency and form is given by an external source. This voltage forces the control element (the piezoelectric actuator for instance) to periodically scan a certain range making the observation of a cavity-resonance spectrum possible. The amplitude and offset is adjustable so that a certain resonator mode can be chosen and locked. The gain and offset at the PI controller can be adjusted as well so that the error signal can be optimized for stable operation. Another very helpful feature is the relock. Whenever an variation in the cavity length or the laser wavelength exceed the locking capability such that the locked resonator mode is lost, the relock feature forces the piezoelectric actuator to scan a full range trying to lock the mode again.
In order to make sure that the performance of the feedback loop is not limited by the lock-box electronics it is desirable to measure the speed of the lock-box. This can be approximated by disabling the integral part of the PI-controller and finding the frequency corresponding to a phase delay of 180 °. By applying a sinusoidal voltage to the input (error signal) and comparing it to the output this is easily done. After some modifications the speed of the lock-box in this setup was measured to be approximately 113 kHz.

5.2.4 Photodiodes

Two important points concerning photodiodes are the signal-to-noise ratio (SNR) and the maximal frequency detectable. The speed of a conventional photodiode alone is determined by the size of the active area where a smaller diode is faster. The photocurrent typically delivered by such a diode is very small which requires amplification before signal processing. Because of the noise inevitable introduced from the environment the first amplification stage should be as close to the diode as possible. A detailed analysis of how to generally build an appropriate front end is given in [12]. Here only two special points should be mentioned.
A problem concerning most amplifier electronics is that they are typically either fast but insensitive to dc signals or sensitive to dc signals but slow. For this reason two photodiodes are required for observation of the reflected light. A fast photodiode for the error signal generation and another for monitoring the incoupling efficiency. This can

Figure 5.7 – On the left the TEM_{00} mode is shown in the unlocked (top) and locked (bottom) case, the contribution from higher order modes are clearly visible in the upper picture. Beside the shown higher order modes (TEM_{10}, TEM_{12} and TEM_{40}) many strange transversal modes were lockable where two examples are shown on the right.

also be implemented with one diode but two different amplifier stages on the same chip giving two distinct outputs (broadband photodiode). In the test setup, however, two separate, self built photodiodes are employed.
The performance of the PDH lock strongly depends on the amplitude of the error signal. For evaporative cooling the power in the resonator has to be lowered by several orders of magnitude and the error signal will change accordingly. To avoid unlocking the resonator a second amplifier stage can be used whose gain is automatically adjusted with respect to the incoming signal keeping the error signal constant for a wide range of resonator power. A detailed description of this automatic gain control in the context of evaporative cooling can be found in [37].

5.3 Characterization of the resonator and the feedback loop

In order to validate the performance of the cooling resonator characterizing measurements on the cavity itself and on the electronics are necessary. For the test resonator not all of the discussed elements were finally set up. For example only one beam was coupled into the cavity and the power control was not implemented at all. But measurements on this setup can give some feeling for the performance of the final setup.
Before measurements of the speed of the feedback loop are shown (5.3.2) some general points characterizing the test setup should be mentioned (5.3.1). In the final subsection a measurement of the resonator finesse, which is the key characteristic of every cavity, is presented (5.3.3).

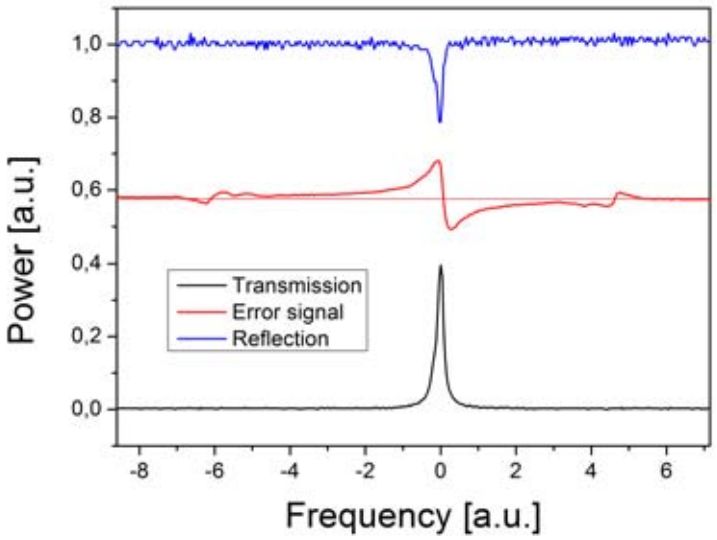

Figure 5.8 – The three quantities monitored by the oscilloscope around the TEM_{00} cavity resonance. One sees the reflection the transmission and the error signal where the reflection and the error signal are scaled by a factor of 15 and the zero line for the error signal is indicated seperately. The two extra features in the error signal probably originates from the sidebands and the asymmetry on the frequency axis from the non-linearity of the piezoelectric actuator.

5.3.1 Characteristics of the test resonator

Precise knowledge about the experimental setup is necessary for every experiment. During the measurements for the characterization of the test setup four quantities were constantly monitored showing the current status of the setup. Namely these quantities are the mode circulating in the cavity on a CCD camera and the error signal, the transmission as well as the reflection on an oscilloscope. As can be seen from figure 5.7 many different modes were accessible within one resonator adjustment. This shows that the overlap between the incoupling beam and the TEM_{00} mode has to be optimized (mode matching) in order to optimize the incoupling efficiency. The incoupling efficiency observed for this test setup was typically 25 % for the TEM_{00} where only a rough optimization was performed. The error signal suffers under the multi-mode operation and should become better when the incoupling is optimized.
During all the time a permanent slow drift between the laser wavelength and cavity resonance is observed. Although this could be caused either by a drift of the laser wavelength or the effective resonator length the latter is more probable since the laser head is specified to be very stable [36]. The test resonator in contrast suffers from a rather bad mechanical mounting compared to the final setup and changes in temperature which will be strongly suppressed once the resonator is placed inside the vacuum. When the

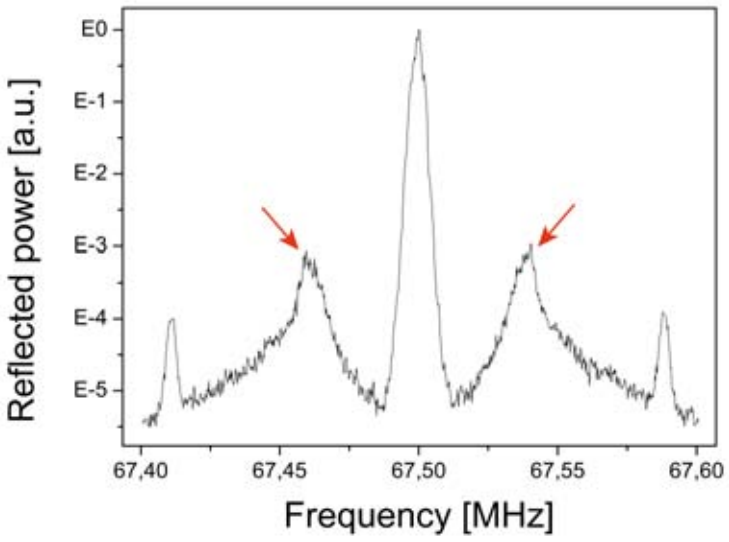

Figure 5.9 – Semi logarithmic plot of the power reflected from the cavity versus frequency measured with a spectrum analyzer. The center peak equals the EOM modulation frequency of 67,5 MHz. A measurement of the servo-bump position (indicated with arrows) yield a speed of the feedback loop of approximately 42kHz. The two extra features are not identified.

drift should be a problem in the final setup nevertheless a temperature lock of the laser head on the cavity is possible. For now the large deviations from resonance are corrected manually by changing the temperature of the laser crystal.

5.3.2 Speed of the feedback loop

To achieve an efficient incoupling the laser wavelength has to match the cavity length for all times. Therefore the cavity length and the laser wavelength are locked to each other by an active feedback loop. The performance of the cooling resonator depends critically on the performance of the frequency stabilization hence knowledge about the performance of the feedback loop is desirable. A possibility to measure the speed of a feedback loop for frequency stabilization is outlined in the following and a measurement in the test setup is presented.
In an optimal case neither the laser wavelength nor the cavity length changes over time. In this case the light reflected from the cavity at the incoupling mirror has a constant amplitude. When monitoring this light with a photodiode and a spectrum analyzer in principle a delta peak at zero should be visible. However, because of the limited bandwidth of every spectrum analyzer the peak will be broadened. Furthermore in reality a change in the resonator length is inevitable due to vibrations for instance. When the change of the resonator length is periodical modulated it will lead to a periodic variation

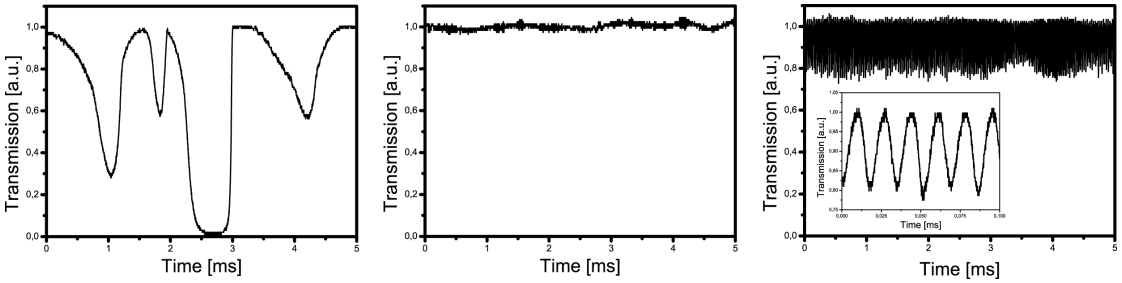

Figure 5.10 – Representative cavity transmission signals collected for three different gain settings at the lock-box. For low gain the errors often exceed the correction capability and the circulating power drops drastically (left). For optimal gain settings the feedback loop efficiently damps the deviations from resonance between laser frequency and resonator length and the variations in the circulating power are minimized (middle). When the gain is set to high the feedback loop start oscillating (with approximately 58 kHz) which again decreases the stability (right).

of the incoupling efficiency and consequently to a periodic variation of the amplitude of the reflected light. At the spectrum analyzer this modulation will show up as a distinct peak where the position is determined by the periodicity of the length variation. In realistic situations deviations between the laser wavelength and the cavity length occur with every modulation period leading to a noise spectrum at the spectrum analyzer. For a typical cavity the amplitude of this noise is a decreasing function of frequency. An active feedback loop can be employed to damp the noise which leads again to a single peak at zero in the optimal case. Unfortunately the speed of a realistic feedback loop is limited so that the feedback loop becomes inefficient for high frequencies. Furthermore, for noise where the phase between the oscillating deviation and the correction signal approaches 180 ° the noise at the corresponding frequency is enhanced instead of damped. This enhancement can be seen at the spectrum analyzer as the so called servo-bump. Therefore the frequency where the servo-bump is located is a measure for the speed of the feedback loop.

As discussed above the speed of the entire feedback loop can be estimated from the reflected light on the entrance of the resonator whilst it is locked. Using a fast photodiode and a spectrum analyzer the frequency noise spectrum looks like depicted in figure 5.9. The shown maximum is due to the strong *noise* introduced by the beat between the sidebands and the laser wavelength which has the frequency of the EOM modulation. The other noise is centered around this maximum since both signals are mixed when detecting the light with a photodiode[5]. This way a speed of 42 kHz was measured for the feedback loop in the test setup. Taking into account that only the slow feedback with the piezoelecric actuator of the laser was implemented so far this is well appropriate. Further

[5]For a single noise frequencies Ω_n and the modulation frequency Ω_m this phenomenon is obvious: $E = E_m cos(\Omega_m t)e^{i\omega t} + E_n cos(\Omega_n t)e^{i\omega t} \rightarrow$
$|E|^2 = E_m^2 cos^2(\Omega_m t) + E_n^2 cos^2(\Omega_n t) + E_m E_n cos((\Omega_m - \Omega_n)t) + E_m E_n cos((\Omega_m + \Omega_n)t)$ for real modulation E_m and noise E_n amplitudes. The shifted noise is expressed in the last two terms.

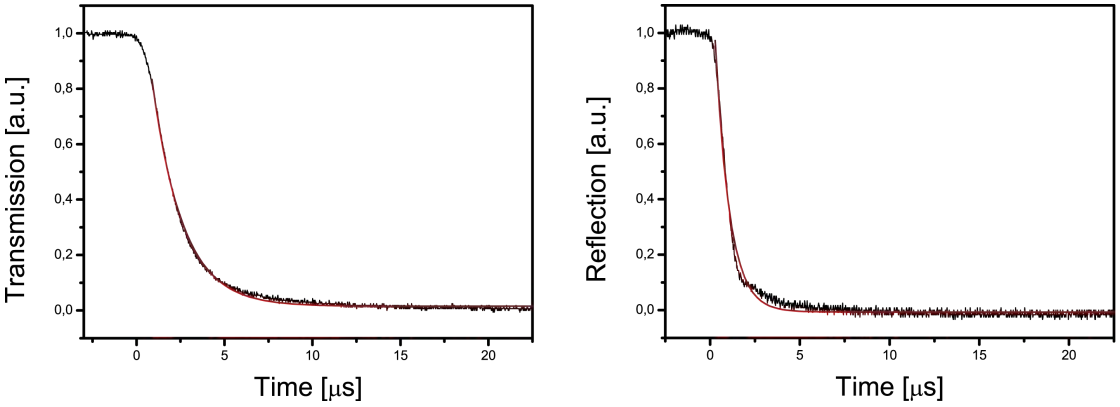

Figure 5.11 – Left: the transmission monitored by a photodiode when the beam incident on the cavity is shut off at $t = 0$. The ring-down time extracted from this measurement is $\tau = 1.79 \pm 0.02\,\mu$s. Right: the reflection at the incoupling mirror of the cavity monitored by a photodiode when at $t = 0$ an AOM placed in the beam path is shut off. A time constant of $0.77 \pm 0.03\,mu$s was obtained from this measurement. The deviation from exponential decay is probably due to the slow reaction time of the photodiode.

improvement through implementation of the fast part through an AOM is expected to be possible and required for stable operation under experimental conditions.
For this measurement the error signal gain at the lock-box was adjusted to optimal locking which is characterized by two distinct phenomena. When the error signal is too small vibrations easily exceeds the locking range and only the relock feature keeps the cavity in resonance. If in contrast the gain is too high the feedback loop starts oscillating. Both phenomena can be identified by their characteristic signatures in the transmitted intensities, shown in 5.10.

5.3.3 Finesse of the resonator

As a first step to characterize the resonator itself its finesse was measured. There are two distinct methods to measure the finesse of a cavity relying on the measurement of the ring-down time (equation 4.14) and the fraction of the full spectral range to the linewidth (equation 4.10), respectively. In many cases the measurement of the ring-down time is the more accurate method since nonlinearities in the expansion of the piezoelectric actuator might influence the measurement of the free spectral range. Furthermore, in this setup it was not possible to observe the whole free spectral range at once since the scanning range is limited to approximately 80 MHz.
For the measurement of the ring-down time the resonator is locked and the transmission behind the resonator is monitored. When the beam incident on the cavity is suddenly switched off, an exponential decay of the transmitted light is observed (figure 5.11). By extracting the time constant of this decay and measuring the resonator length the finesse can be determined. This measurements result in a time constant of $\tau = 1.79 \pm 0.02\,\mu$s and a resonator length of $L = 0.87$ m yielding $F = 3878 \pm 43$. The indicated error results

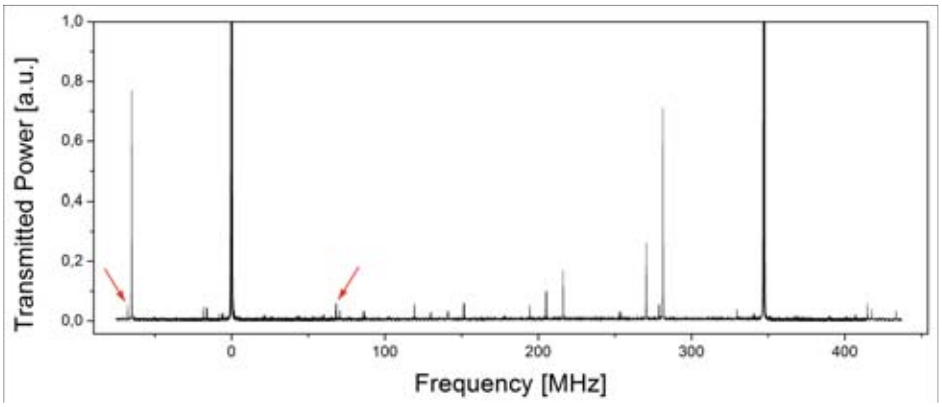

Figure 5.12 – A typical cavity resonance spectrum combined from multiple measurements. The strongest signal originates from the TEM_{00} mode and is much higher than the measuring range. The arrows indicate the sidebands from the EOM modulation.

from multiple measurements of the ring-down time. The systematic error for the measurement of the resoantor length is expected to be below 0.01 m it originates from the fact, that the exact position of the beam on the mirrors was not observed. A possible systematic error for the measurement of the ring-down time is discussed in the following. The finesse obtained from the measurements of the ring-down time of $F = 3878 \pm 43$ strongly deviates from the design value of roughly 2000. The ring-down time calculated with the measured mirror reflectivities of 99.85% and 99.992% and the resonator length of 0.86 m is approximately $\tau = 0.84\,\mu$s. One possible explanation for the discrepancy is that the AOM turn-off time is expected to be on the same order of magnitude ($\approx 0.37\,\mu$s). Then, however, the ring-down time is not longer much larger than the turn-off-time which leads to a complicated superposition of the corresponding decays in the transmission of the resonator and a strict quantitative analysis of the measured signal becomes much more difficult. To confirm that this is the error source the turn-off time in the reflected signal was measured (figure 5.11). By fitting an exponential decay a time constant of $0.77 \pm 0.03\,\mu$s was obtained. The obvious deviation from exponential decay and calculated turn-off time is probably caused by the slowly decaying photocurrent in the rather large photodiode which was used[6]. In principle it is possible to get a faster decay of the photocurrent and therefore a better result for the ringdown-time by inserting a smaller[7], faster diode. Unfortunately inserting a smaller photodiode in the electronics employed results in oscillations in the electronics of the photodiode front end. The fact that these oscillations can only be observed in the reflected power shows that the ring-down contributes with the same order of magnitude to the total signal. Effectively the decay of the power seen in the transmission of the resonator is some mixture of the effects of the AOM turn-off, the photocurrent in the photodiode and the real ring-down of the

[6] Hamamatsu: $G8370 - 01$.
[7] Hamamatsu: $G8376 - 03$.

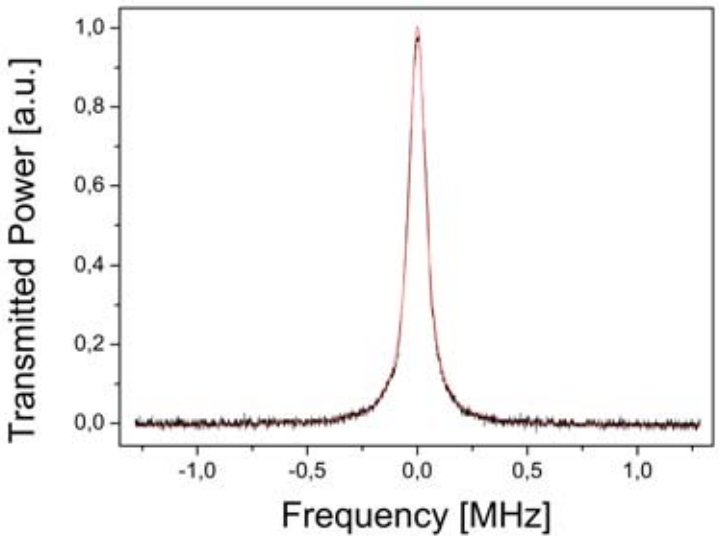

Figure 5.13 – Typical resonance peak of the TEM_{00} mode measured with a oscilloscope (black). From the fitted Lorentzian curve (red) a line width of $\Delta\nu_l = 83 \pm 9\,\mathrm{kHz}$ was obtained, where the frequency scale was taken from figure 5.12 (the experimental settings were not changed between both measurements).

resonator. Since they all are on the same order of magnitude a strong error in the finesse measured this way is expected.
To obtain a better result the free spectral range and the line width were measured directly. For determining the finesse one actually only needs to measure the ratio between these quantities so a frequency reference is not necessary. However, the EOM sidebands offer such a reference allowing for simple measuring of absolute values. In principle these measurements can easily be done by monitoring the transmission behind the resonator while scanning the laser frequency. Unfortunately the piezoelectric tube of the laser head in combination with the given voltage is not able to scan over a full free spectral range. Therefore multiple pictures were taken. The center frequency of the laser is changed between those pictures by changing the temperature of the laser crystal manually. Combining the single datasets leads to figure 5.12. Here the nonlinearity of the expansion of the piezoelectric crystal became obvious. To minimize the effect of this nonlinearity only a quarter of the possible voltage was applied to the piezoelectric crystal. The remaining error of this effect was estimated to be approximately $\pm 7\,\%$ for the free spectral range. The sidebands can easily be identified by switching on and off the EOM and are marked in figure 5.12. The EOM frequency for these measurements was 68 MHz. Figure 5.13 shows the transmission peak of the TEM_{00} mode. This peak is fitted with a Lorentzian function to obtain the linewidth. It is essential to keep the settings of the lock-box unchanged between both measurements in order to keep the frequency axis comparable. By this

method a free spectral range of $\Delta\nu_f = 347 \pm 56\,\mathrm{MHz}$ and a linewidth of $\Delta\nu_l = 83 \pm 9\,\mathrm{kHz}$ was obtained which results in a finesse of $F = 4190 \pm 737$. Surprisingly this coincides with the result obtained from the ring-down measurement (within the error-range) implying that the measured mirror reflectivities contains large errors. Therefore the finesse obtained from the ring-down measurements ($F = 3878 \pm 43$) is expected to be quite accurate. However, the indicated error range originates from multiple measurements of the linewidth and does not account for systematic errors in the measurement of the resonator length or the ring-down time due to the superposition of the three decays.
A more realistic value and error range can be derived when the measured linewidth is combined with the free spectral range calculated from the measured resonator length. It is expected that the systematic errors due to the nonlinearity of the piezoelectric actuator are neglectable for the measurement of the linewidth since here only a very small scanning range is used. Therefore the error for the linewidth is governed by statistical errors and the linewidth is given by: $\Delta\nu_l = 83 \pm 9\,\mathrm{kHz}$. The error for the measurement of the resonator length is estimated to be less than one centimetre and the length is measured to be $L = 0.87 \pm 0.01\,\mathrm{m}$. With these values the finesse of the resonator can be calculated to be $F = 4155 \pm 453$. The free spectral range and the enhancement can be derived as well they are $\Delta\nu_f = 345 \pm 4\,\mathrm{MHz}$ and $\varepsilon = 1323 \pm 144$ respectively. The design value for the enhancement is $\varepsilon = 633$ which implies that the measured enhancement is approximately twice the design value but since locking was possible and the time for transport is approximately 0.5 s which is still reasonable no complications are expected.

6 Conclusion & outlook

In this diploma thesis a ring resonator for a novel all-optical cooling scheme was designed and tested. Since this resonator will be placed inside the vacuum in order to reduce the losses and make a high power enhancement possible, the main vacuum chamber was designed as well.
All quantum gas experiments rely on evaporative cooling to reach temperatures at the Nanokelvin scale. The choice of the trapping potential is crucial to realize an efficient evaporation scheme since the trapping potential determines the initial atom number and the thermalisation rate. The new evaporation scheme employed in this experiment is designed to overcome the drawbacks of the dependency on the spin state for magnetic traps and the small capturing volume for typical deep dipole traps. Two counter-propagating laser beams are coupled into a ring resonator and the atoms will be loaded from the MOT into the interference pattern at a large beam diameter outside of the focus of the resonator mode. The atoms will subsequently be transported to the resonator focus and evaporation will be performed in a traveling wave configuration. The transport leads to an enhanced atom density in the focus which consequently results in an enhanced thermalisation rate. Since no magnetic fields are used for trapping a Feshbach resonance can be used to further enhance the evaporation efficiency.
Apart from a small focus which determines the divergence and therefore the beam diameter at the MOT position, a high enhancement was the most important goal for the resonator design. In order to reach an enhancement of roughly 600 the resonator will be placed inside the vacuum which minimizes the losses. The design of the resonator and the vacuum chamber thus have strong impact on each other. Therefore special attention was paid to construct mirror holders for the cooling resonator which are very compact and enable the possibility to test the whole resonator setup outside of the vacuum chamber. Nevertheless a stable resonator setup was realized. In addition to the cooling resonator the chamber geometry is determined by the optical access required and the magnetic coil arrangement for the MOT field and the Feshbach field. Optical access is necessary for the MOT beams, the atomic beam which is either created by a Zeeman slower or by an optional 2D-MOT, the resonator beams and for imaging as well as for a second dipole trap which realizes a transport of the atoms from the position where the evaporation is performed into a glass cell. The option for the 2D-MOT is included to maintain maximal flexibility. For the same reason a broadband coating was chosen for the viewports at the main vacuum chamber. The magnetic fields are generated by a single pair of coils which is situated very close to the position of the atoms in the dipole trap. Since the MOT lies off-center with respect to these coils additional pushing coils are used to shift the MOT field.
The vacuum chamber and the resonator were designed as 3D-models and manufactured

in professional workshops. All desired elements have arrived in the lab by now and the vacuum chamber as well as the final resonator are being assembled. However, when the work in the lab started not all parts of the resonator were produced so that first measurements to characterize the resonator were performed with a test resonator. Moreover, the electronics and optics necessary to stabilise the resonator were also implemented and tested. With this setup the finesse of the resonator was determined to be $F = 4155 \pm 453$, a value that is approximately a factor of two higher than the design value. This discrepancy may be explainable with large spatial inhomogenities in the mirror coating process. The design value was chosen relatively low to make the frequency stabilization less challanging. However, already in the test setup only a slow frequency stabilization with a measured bandwidth of 42 kHz was sufficient to lock the resonator. Hence we are in the fortuitous position to have a larger power enhancement without significant drawbacks.
As the next step it is planned to test the final cooling resonator where special attention will be paid to the performance of the piezoelectric actuator. Once this slow part of the feedback loop is shown to perform well the fast part of the feedback loop realized with an AOM will be implemented and tested as well. To complete the setup for the cooling resonator the second beam will be coupled into the resonator and the power control will be implemented and tested as well. The last task performed in the test setup will be the optimal adjustment of the resonator mode to TEM_{00} with a small focus. Afterwards the optical and electronic setup will be moved to the main experimental table and the resonator will be inserted into the vacuum chamber. Finally the transfer from the MOT, the transport and the evaporative cooling will be tested and optimized.
Parallel to the work at the resonator the other parts of the experimental setup are planned and assembled. For example the design of the magnetic coils and appropriate holders was carried out by K. Morgener and the manufacturing is in progress. The oven and the glass cell design are finished as well (by W. Weimer) and the oven is already assembled. At the moment the work in the lab concentrates on the chamber bake-out and resonator testing as well as on setting up the laser system and optics for the MOT beam preparation. When all this is accomplished and the new experiment is finally set up it will offer a high degree of flexibility as well as excellent imaging resolution. Therefore it is expected that exciting results will be produced and the experiment will contribute to the field of ultra-cold atoms in the next years.

7 Appendix

7.1 Feshbach resonances

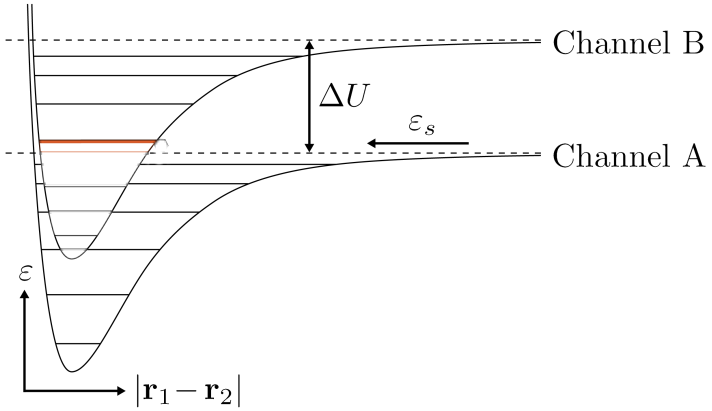

Figure 7.1 – The s-wave scattering potential for two neutral atoms. The open (bottom) and closed (top) channel are characterized by distinct internal states. Indicated are some vibrational dimer states, the scattering energy ε_s and the (tunable) channel spacing ΔU. The background scattering length a_0 is determined by the energy of the highest bound state in channel A.

The term Feshbach resonance originates from nuclear physics where resonance phenomena in nuclear reactions can be described by a generalized theory of Herman Feshbach. The most basic expression of Feshbach like phenomena is the Levison theorem which claims that a resonant enhancement of the scattering length can be observed whenever a new bound state appears at the dissociation energy of a potential.
Nowadays magnetically induced Feshbach resonances are a widely used tool in the field of quantum gases. They allow for arbitrary manipulation of the interaction strength when changing the magnetic field hence they enable the investigation of such exiting phenomena as fermionic superfluidity and quantum magnetism. In the frame of this work Feshbach resonances are important to enhance the efficiency of the evaporative cooling. A detailed discussion of Feshbach resonances is out of the scope of this thesis such that only a very short qualitative overview will be given. Very comprehensible summaries can be found in [6] and [21] where this section is based on the latter.

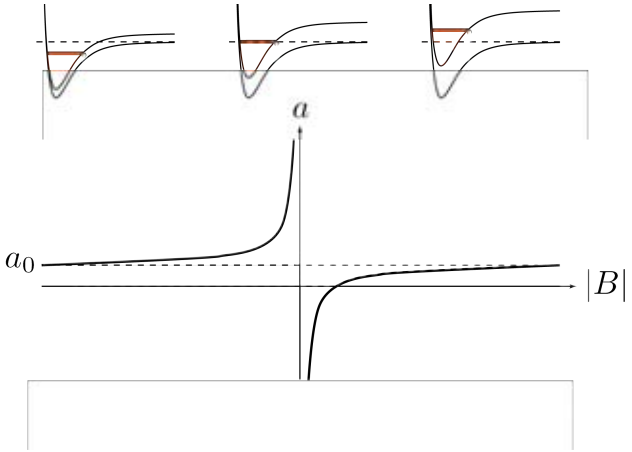

Figure 7.2 – The qualitative behavior of the scattering length a around a Feshbach resonance (bottom) and the corresponding position of a bound state in the closed channel with respect to the dissociation energy of the open channel (top) are shown. Please note that for positive scattering lengths an accessible (when ramping over the resonance) molecular state evolves.

Figure 7.1 schematically shows the s-wave scattering potential[1] of two neutral atoms for two different internal state configurations (scattering-channels). Those channels may be defined by different spin configurations which allow for tuning the energy difference (ΔU) due to the Zeeman effect with a magnetic field. This of course also changes the position of the bound states[2] in the B channel relative to the dissociation energy of channel A. If a bound state of channel B has an energy similar to the scattering energy ε_s and a coupling between both channels is present this state will modify the scattering wavefunction and hence the scattering length. The influence of the bound state in B on the scattering length depends on its position relative to the dissociation energy of channel A and thus on an externally applied magnetic field. This offers the possibility to tune the interaction of an atomic gas by adjusting the current in a magnetic coil.
The qualitative behavior of the scattering length around a Feshbach resonance (for low energies) is shown in figure 7.2. The corresponding formula reads:

$$a = a_0 \left(1 - \frac{\Delta B}{B - B_{res}}\right) \tag{7.1}$$

where ΔB is the region where a has the opposite sign to the background scattering length a_0. It is determined by the coupling strength between the two channels and $\frac{\partial}{\partial B}\Delta U$ on resonance.
To address the Feshbach resonance in a whole atomic ensemble a homogeneous magnetic field is necessary which can be generated by a Helmholtz coil configuration.

[1] For higher angular momentum the centrifugal barrier has to be taken into account.
[2] They are not really bound since they can spontaneously decay in the continuum of channel A.

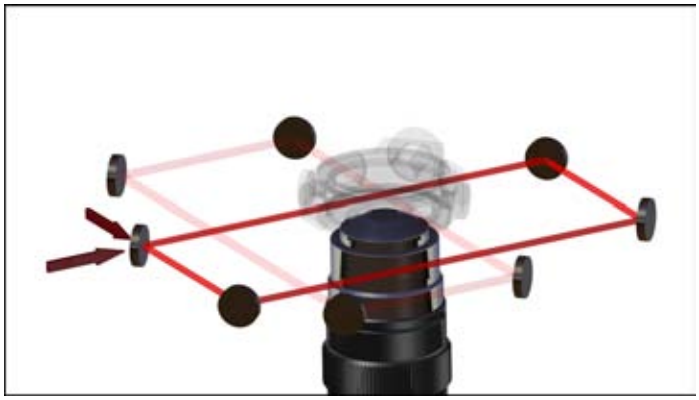

Figure 7.3 – Artistic impression of the glass cell surrounded by two ring cavities and a microscope. A second, identical microscope will be placed above the glass cell so that imaging and manipulation of the atoms on the Nanometre scale is simultaneous possible. The resonators will be used to realize different dipole potentials where confinement in the vertical direction can be added by separate laser beams.

7.2 The glass cell

The glass cell within the experimental setup can be seen right in front of figure 3.1. The glass cell is surrounded by a stable structure for attachment of magnetic coils which allows for precise control of the interaction strength in the atomic ensemble. Two microscopes ($NA = 0.62$) below and above the glass cell allow for both, observation and manipulation with nearly single site resolution. This high resolution is possible since the glass cell is only 16 mm high. The geometry of the glass cell is determined by the beams planned to use. As depicted in figure 7.3 two four mirror ring resonators are employed to generate a crossed dipole trap. The advantage of this resonator design is that very deep traps can be generated with moderate laser power and additional the beam will have a very stable, clear profile. Another point is that two beams coupled into one resonator will always perfectly overlap. This can for example be used to generate nearly homogeneous potentials by coupling in one red and one blue detuned laser. To benefit from the high enhancement of the resonators it is important that the glass cell is anti reflection coated. For conventional glass cells coating from inside is not possible. However, with a special bonding technique it is possible to manufacture a glass cell where for the optical access a coating is applied[3]. The resonators provide a very elliptical mode and by shining in two blue detuned beams from the vertical direction under an angle of only 12° we are able to bring a large fraction of the atoms in a two-dimensional system. Of course it is also possible to generate optical latices by coupling counter propagating beams into the resonators. In addition optical access for three beams at an angle of 120° is foreseen which allows for the generation of triangle latices.

[3]The glass cell is manufactured by the technical glass devision of *Precision Glassblowing of Colerado*.

8 Bibliography

[1] M. Albiez, R. Gati, J. Fölling, S. Hunsmann, M. Cristiani, and M. K. Oberthaler, *Direct observation of tunneling and nonlinear self-trapping in a single bosonic josephson junction*, Physical Review Letters, 95 (2005), p. 010402.

[2] M. Anderson, J. Ensher, M. Matthews, C. Wieman, and E. Cornell, *Observation of Bose-Einstein Condensation in a Dilute Atomic Vapor*, Science, 269 (1995), pp. 198–201.

[3] M. Bartenstein, A. Altmeyer, S. Riedl, R. Geursen, S. Jochim, C. Chin, J. Hecker Denschlag, and R. Grimm, *Precise determination of 6li cold collision parameters by radio-frequency spectroscopy on weakly bound molecules*, Physical Review Letters, 94 (2005), p. 103201.

[4] E. D. Black, *An introduction to Pound-Drever-Hall laser frequency stabilization*, American Journal of Physics, 69 (2001), pp. 79–87.

[5] S. Chiesa, C. N. Varney, M. Rigol, and R. T. Scalettar, *Magnetism and Pairing of Two-Dimensional Trapped Fermions*, Physical Review Letters, 106 (2011), p. 035301.

[6] C. Chin, R. Grimm, P. Julienne, and E. Tiesinga, *Feshbach resonances in ultracold gases*, Reviews of Modern Physics, 82 (2010), p. 1225Ű1286.

[7] B. DeMarco and D. S. Jin, *Onset of Fermi Degeneracy in a Trapped Atomic Gas*, Science, 285 (1999), pp. 1703–1706.

[8] M. Eckstein, M. Kollar, and P. Werner, *Thermalization after an Interaction Quench in the Hubbard Model*, Physical Review Letters, 103 (2009), p. 056403.

[9] S. Giorgini, L. P. Pitaevskii, and S. Stringari, *Theory of ultracold atomic Fermi gases*, Reviews of Modern Physics, 80 (2008), p. 1215Ű1274.

[10] R. Grimm, M. Weidemüller, and Y. B. Ovchinnikov, *Optical Dipole Traps for Neutral Atoms*, Advances In Atomic, Molecular, and Optical Physics, 42 (2000), pp. 95–170.

[11] K. Günter, T. Stöferle, H. Moritz, M. Köhl, and T. Esslinger, *Bose-fermi mixtures in a three-dimensional optical lattice*, Physical Review Letters, 96 (2006), p. 180402.

[12] P. C. Hobbs, *Photodiode Front Ends: The Real Story*, Optics and Photonics News, 12 (2001), pp. 44–47.

[13] P. C. D. Hobbs, *Building electro-optical systems*, John Wiley & Sons, 2008.

[14] S. Hong, S. Y.H., and K. J.T., *Residual gas survey of stainless steel 304 extreme high vacuum chamber with hot cathode ionization gauge*, Measurement, 41 (2008), pp. 1026–1031.

[15] P. Horowitz and W. Hill, *The art of electronics*, Cambridge University Press, 2 ed., 1989.

[16] J. Hubbard, *Electron Correlations in Narrow Energy Bands*, Proceedings of the Royal Society of London. Series A, Mathematical and Physical Sciences, 276, No. 1365 (1963), pp. 238–257.

[17] M. Inguscio, W. Ketterle, and C. Salomon, *Ultra-cold Fermi Gases*, in Proceedings of the International School of Physics "Enrico Fermi", 2008.

[18] D. Jaksch, C. Bruder, J. I. Cirac, C. W. Gardiner, and P. Zoller, *Cold bosonic atoms in optical lattices*, Physical Review Letters, 81 (1998), pp. 3108–3111.

[19] W. Ketterle and M. W. Zwierlein, *Making, probing and understanding ultracold fermi gases*, arXiv:0801.2500, (2008).

[20] P. A. Lee, N. Nagaosa, and X.-G. Wen, *Doping a Mott insulator: physics of hightemperature superconductivity*, Reviews of Modern Physics, 78 (2006), pp. 17–85.

[21] A. Marte, *Feshbach-Resonanzen bei StöSSen ultrakalter Rubidiumatome*, PhD thesis, Technische Universität München, 2003.

[22] H. J. Metcalf and P. van der Straten, *Laser Cooling and Trapping*, Springer, 1999.

[23] A. Mosk, S. Jochim, H. Moritz, T. Elsässer, M. Weidemüller, and R. Grimm, *Resonator-enhanced optical dipole trap for fermionic lithium atoms*, Optics Letters, 26 (2001), pp. 1837–1839.

[24] R. Mottl, *A bowtie resonator trap to load, transport and cool fermionic atoms*, master's thesis, ETH Zürich, 2009.

[25] J. F. O'Hanlon, *A User's Guide to Vacuum Technology*, John Wiley & Sons, 2003.

[26] C. Ospelkaus, S. Ospelkaus, L. Humbert, P. Ernst, K. Sengstock, and K. Bongs, *Ultracold heteronuclear molecules in a 3d optical lattice*, Physical Review Letters, 97 (2006), p. 120402.

[27] C. Pethick and H. Smith, *Bose-Einstein Condensation in Dilute Gases*, Cambridge University Press, 2 ed., 2008.

[28] A. Polkovnikov, K. Sengupta, A. Silva, and M. Vengalattore, *Nonequilibrium dynamics of closed interacting quantum systems*, arXiv:1007.5331v1, (2010).

[29] A. Prodromides, *Non-Evaporable Getter Thin Film Coatings for Vacuum Applications*, PhD thesis, Ecole Polytechnique Federale de Lausanne, 2002.

[30] Product catalogue, *The Vacuum Technology Book*, Pfeiffer Vacuum GmbH, 2008.

[31] J. Sakurai, *Modern Quantum Mechanics*, Addison-Wesley Publishing Company, 1994.

[32] T. Schnider, *Design of a Second Generation Optical Lattice Experiment for an Ultra-Cold ^{40}K Quantum Gas*, master's thesis, ETH Zürich, 2009.

[33] A. E. Siegman, *Lasers*, University Science Books, 1986.

[34] O. Svelto, *Principles of Lasers*, Springer, 2010.

[35] U. Tietze, C. Schenk, and E. Gamm, *Halbleiter-Schaltungstechnik*, Springer, 13 ed., 2010.

[36] User's Manual, *Mephisto MOPA Product Line*, Innolight, Version 2.1.

[37] W. Weimer, *Stabilizing a Diode Laser on a Narrow Linewidth Ring Cavity*, master's thesis, ETH Zürich, 2010.

[38] Wikipedia, *Pressure measurement — Wikipedia, The Free Encyclopedia*, 2011. [Online; accessed 18-April-2011].

[39] Wikipedia, *Sagittalebene (Optik) — Wikipedia, The Free Encyclopedia*, 2011. [Online; accessed 21-April-2011].

[40] B. Zimmermann, T. Müller, J. Meineke, T. Esslinger, and H. Moritz, *High-resolution imaging of ultracold fermions in microscopically tailored optical potentials*, New Journal of Physics, 13 (2011), p. 043007.

9 Acknowledgement

First of all I would like to thank Prof. Dr. H. Moritz for giving me the opportunity to contribute to the new experiment with this diploma thesis and for his support whenever a problem arose. It was a very exiting and instructive experience to see the new group and the experiment growing.
Special thanks are due also to Prof. Dr. K. Sengstock who is the second advisor for this thesis. He was the one to get me enthusiastic about the research field of quantum gases due to his motivating lectures and his talent to transfer his own fascination to others.
I would like to thank each member of the research group for his support and the enjoyable atmosphere in the office and the lab, apart from the bobbery produced by W.W. of course. I had a great time working with you.
Without the help of the administrative and technical staff at the institute and in the physics workshop this diploma thesis would not be possible. Therefore I would like to thank Ellen Gloy, Reinhard Mielck and Ralf Lühr as well as Stephan Fleig and Thomas Marckmann for the invaluable support they gave me.
Very special thanks to my teachers W. Falkenberg and G. Mücke who engaged my interest for sciences in school and believed in me when others already gave up. I know that you are a main reason why it was possible that I could follow my interests and study physics.
I would like to thank my fellow students as well since they constantly encourage me to learn and learn and learn... Apart from the time at the university I will always remember the countless nights in the student dorms, at the Reeperbahn or just at home with one to twelve bottles of beer. Here Damian Böcker is to mention by name who, I think I can say that, is my best fellow student and a really good friend.
Of course I do not forget about my friends from da big city who helped me very actively when it came to drinking and barbecue. Especially Joschka Böddeling is to mention since he tried to improve my englisch in this diploma thesis unsuccessfully.
For my loved girlfriend I have a thousand kisses instead of a single *thank you*. She made the past years the most happiest of my life and dragged me to the *real life* whenever I despaired on physical problems. Kocham cię mój chomiczku!
Last but not least I would like to express my deep gratefulness to my parents. They supported me throughout my whole education and finally learned to exercise patience when my learning process took a little longer.